Adsorption and Oxidation of Formate at Au Electrodes

by

Jonathan Richard Strobl
B.Sc., University of Saskatchewan, 2011

A Thesis Submitted in Partial Fulfillment of the
Requirements for the Degree of

Master of Science

in the Department of Chemistry

Adsorption and Oxidation of Formate at Au Electrodes

by

Jonathan Richard Strobl

B.Sc., University of Saskatchewan, 2011

Supervisory Committee

Dr. D. A. Harrington, Supervisor (Department of Chemistry)

Dr. A. G. Brolo, Departmental Member (Department of Chemistry)

Dr. M. G. Moffitt, Departmental Member (Department of Chemistry)

Supervisory Committee

Dr. D. A. Harrington, Supervisor (Department of Chemistry)

Dr. A. G. Brolo, Departmental Member (Department of Chemistry)

Dr. M. G. Moffitt, Departmental Member (Department of Chemistry)

Abstract

This work focuses on tracking formic acid adsorption as formate onto polycrystalline gold and its subsequent catalyzed oxidation to CO_2. Formic acid oxidation is notoriously dependent on supporting electrolyte composition, a dependency that is little characterized. Additionally, the mechanism of oxidation is in disagreement in the literature. As such, the two preceding topics are the primary focus of this work, and are studied in $HClO_4$ and H_2SO_4 solutions. Cyclic voltammetry experiments supplemented by mathematical modelling and fitting of data were used. Solution pH and adsorption of supporting electrolyte anions onto Au(poly) were very influential factors in determining formate coverages on Au(poly). This alone explains the effect of supporting electrolyte on this reaction. The coverage of adsorbed formate was found to be singularly responsible for determining the rate of formic acid oxidation. This implies a chemical rate limiting step for oxidation, leaving the oxidation rate constant independent of potential.

Another segment of this work focuses on the statistical mechanics of lattice gases, namely the role of sites available for adsorption on the activity. This topic is central to the modelling of multiple adsorbing species in competition for the same adsorption sites. Activity for interaction-free lattice gases in the thermodynamic limit was found to be $\theta_i/\theta_{\mathrm{av},i}$, where θ_i is coverage of sites occupied by species i and $\theta_{\mathrm{av},i}$ is coverage

of sites available for adsorption of i. This relationship was exploited to simulate coadsorption of two species, the first obeying the Langmuir isotherm and the second following the hard hexagon isotherm. This system was originally considered as a possible model for coadsorption of formate and sulfate in H_2SO_4 solutions, but did not match with data.

Table of Contents

List of Tables

List of Figures

Acknowledgements

I thank Dr. Robert W. J. Scott and Dr. Priyabrat Dash for introducing me to academic research, and Dr. Ian J. Burgess for introducing me to electrochemistry. The help, guidance and patience of Dr. David A. Harrington during my time at UVic is greatly appreciated. NSERC is thanked for funding, as well as the award of an Alexander Graham Bell Canada Graduate Scholarship. The University of Victoria is thanked for supplying a UVic Fellowship, H. E. Petch and President's Research Scholarship.

To Mom and Dad.

Chapter 1

Introduction

The overreaching topic of this thesis is thermodynamically reversible adsorption of multiple species onto common sites. This is also referred to as "competitive" adsorption, or "coadsorption". This topic is central to understanding adsorption of reaction intermediates onto catalytic electrodes in electrochemical settings. In such settings, the substrate is usually in solution with a supporting electrolyte, which lowers electrical resistance of the solution. A common side effect is the adsorption of supporting electrolyte anions onto the catalyst surface. This lowers available space on the electrode surface, meaning adsorption of the substrate or reaction intermediates is suppressed and catalyst efficiency is decreased. In spite of the major influence this has on many reactions, these effects are often ignored in the literature. Elaboration on both the theory and real world importance of this topic is warranted. This thesis focuses mainly on thermodynamically reversible coadsorption, where these adsorption steps are much faster than other steps in the reaction mechanism. Vastly different time scales for reaction steps can allow independent observation of these steps, making adsorption easier to observe.

Thermodynamically reversible coadsorption is a broad topic, and so this work focuses on several specific experimental systems and aspects of the theory. The electro-

catalytic oxidation of formic acid on Au(poly) was selected as the central experimental system. Chapters 2 and 3 encompass this topic. Each individual chapter is intended for publication in a peer reviewed journal. Au catalyzed formic acid oxidation is explored for fundamental purposes, specifically to highlight the effects of supporting electrolyte on catalyst reactivity. High catalytic acitvities were not observed or expected**.** Formic acid adsorbs reversibly on Au as formate, and then undergoes rate limiting oxidation. The relative speed of adsorption to oxidation makes this reaction ideal for study. Also, supporting electrolyte effects have been observed for this reaction, but have not been investigated thoroughly. This reaction was studied in both perchloric and sulfuric acid electrolyte solutions, classic examples of solutions containing "weakly" and "strongly" adsorbing anions, respectively. A basic electrochemical technique, cyclic voltammetry, was used almost exclusively to study adsorption and oxidation of formate separately. Separate observation was accomplished by changing the voltage sweep rate, which determines the time scale of the measurement. Fitting of observed formate and supporting anion adsorption to the Sips isotherm was done succesfully. This isotherm is capable of accounting for electrode heterogeneity, but it is rare to see it used for multi-adsorbate systems. Adaptation of the isotherm to such systems was straightforwardly and succesfully achieved. Characterization of coadsorption allowed qualitative and quantitative understanding of the catalytic mechanism, since oxidation rates were well correlated to formate coverages.

Some theoretical treatments of coadsorption are carried out in Chapter 4. The content of this chapter was published in The Journal of Chemical Physics [1]. Using a statistical mechanics approach, the role of sites available for adsorption in determining the activity of an adsorbed species was investigated. The investigation was restricted to systems with purely geometric constraints on adsorption, with no long range or nearest-neighbor interactions. Activity for interaction-free lattice gases in the thermodynamic limit was found to be $\theta_i/\theta_{\mathrm{av},i}$, where θ_i is the coverage of sites occupied by species i and $\theta_{\mathrm{av,i}}$ is the coverage of sites available for adsorption of i.

This relationship has major implications in modelling of coadsorption, as the presence of adsorbates on a surface can lower the amount of available sites for an adsorbing species. A non-trivial case for coadsorption was modelled, wherein one species obeys the Langmuir isotherm and the other obeys the hard hexagon isotherm. This system is expected to model formate and sulfate coadsorption on Au(111).

Chapter 2

Formic Acid Oxidation on Au in $HClO_4$ Solutions

2.1 Introduction

The oxidation of formic acid on metal catalysts has been studied for decades, but the mechanism of this reaction on Au electrodes is often in disagreement between different authors. Also, few studies have focused on rationalizing the effects of electrolyte composition on this reaction, in spite of its enormous influence. These are two topics that will be explored in this work.

Although Au often supplies poor catalytic acitivity in the oxidation of $C_1H_xO_y$ species it is modestly active in the case of formic acid. This activity has been studied in UHV conditions [2, 3], as well as in sulfuric [4–11] and perchloric acid [11–15] solutions. In both solutions, the selectivity of Au for oxidizing formic acid in the double layer region (as opposed to other $C_1H_xO_y$ molecules) could be advantageous if one desires exclusive detection of formic acid. Such a selective detector as Au might be used to complement studies on more active fuel cell catalysts, perhaps as the ring in a rotating ring-disk electrode configuration. This would be useful in assessing

the oxidation yields of the more electron rich formaldehyde and methanol, wherein oxidation to CO_2 is desired but partial oxidation yields formic acid.

Furthermore, this reaction has many interesting features, and may lend insight into the mechanism of formic acid oxidation on other metals. A recently proposed mechanism on Au has been sucessfully extrapolated to Pt [15], one of the most active pure metal catalyst for this reaction. It is established that the reaction on Au progresses purely via the so called "direct pathway", whereas oxidation on Pt goes through the direct pathway and an "indirect" pathway. Au serves as a convenient proxy for Pt, as the presence of the "indirect pathway" leads to CO poisoning and complicates mechanistic studies. The universal picture for the "direct pathway" is that formic acid adsorbs as some intermediate onto Au or Pt surfaces, undergoing an oxidation step afterwords. This has been followed with EQCM work [8]. Also, several studies employing SEIRAS [11,15] or SERS [13,14] have correlated adsorbate vibrational intensities to oxidation current as a function of potential. There is also sufficient evidence to identify this intermediate as adsorbed formate [13, 14]. The adsorption (Eq. (2.1)) is usually treated as being essentially reversible, establishing a rapid pre-equilibrium step before formate oxidation. Since the pH of studied solutions is such that no appreciable amount of solution phase formate exists (max pH = 2, $pK_a(HCOOH) = 3.75$), this adsorbate will be referred to simply as "formate" (regardless of charge). The reaction's second step (oxidation) can be generalized according to Eq. (2.2).

$$HCOOH \rightleftharpoons HCOO(ads) + H^+ + e^- \tag{2.1}$$

$$n HCOO(ads) \longrightarrow n(CO_2 + H^+ + e^-) \tag{2.2}$$

Separate studies propose different kinetics for Eq. (2.1), and different stoichiometry. Crepy et al. proposed Eq. (2.1) as written, but this has recently been reimagined

as kinetically hindered formate adsorption from a formic acid dimer by Cuesta and coworkers [11, 15]. These authors have also disagreed upon the reaction order (n) of formate and the potential dependence of the rate constant in Eq. (2.2). Crepy et al. set $n = 1$ with rate limiting electron transfer (potential dependent rate constant) [5,8,10]. Cuesta et al. asserted that $n = 2$ and that a chemical reaction step is rate limiting (potential independent rate constant) [11,15]. This work aims to clarify these details by studying the individual reaction steps as separately as possible. This is achieved by drastically varying voltage sweep rates in cyclic voltammetry (CV) experiments.

This work also studies formate adsorption versus solution composition (in $HClO_4$ solutions) and the resulting oxidation current. The roles of pH, [ClO_4^-], and [HCOOH] are investigated, as these constitute major factors in determining formate coverages. In SO_4^{2-} solutions, Crepy et al. [5] observed pH dependance of reaction rates in the range 0.2-8.0, but did not modify [SO_4^{2-}]. No other studies have varied supporting electrolyte concentrations to the best of our knowledge. This is a worthwhile experiment, as SO_4^{2-} (and ClO_4^-) can compete with formate for sites on Au. EQCM studies [8] showed that mass of adsorbates on the electrode surface decreased from H_2SO_4 to H_2SO_4 + HCOOH solutions. Given the lighter mass of formate, displacement of SO_4^{2-} from Au is implied. Additionally, Cuesta et al. [11] found that formate vibrational intensities were weaker in SO_4^{2-} (strong adsorption) solutions than for comparable concentrations of ClO_4^- (weak adsorption). In the literature, it is often assumed that ClO_4^- does not compete with formate for surface sites. This claim is based on some evidence that ClO_4^- does not adsorb onto Au [16], although many publications say that it does. For example, perchlorate adsorption on Au(111) [17–22], Au(110) [17,21], Au(100) [17,18,21], Au(210) [18] and Au(poly) [17,20] has been observed. Conway et al. proposed stoichiometries for the adsorption of perchlorate on Au(111) or (110) (Eq. (2.3)) and Au(100) (Eq. (2.4)). Our discussion of perchlorate adsorption will follow this same convention.

$$\mathrm{ClO_4^-} \rightleftharpoons \mathrm{ClO_4(ads)} + \mathrm{e^-} \tag{2.3}$$

$$\mathrm{ClO_4^-} \rightleftharpoons \mathrm{ClO_4^-(ads)} \tag{2.4}$$

Formate coverage grows over wider potential / concentration regimes than predicted by the Langmuir isotherm (true in all previous studies). In one interpretation, quantitative description of formate adsorption onto Au(poly) requires accounting for electrode heterogeneity. A popular adsorption isotherm achieving this is the Sips isotherm [23], an adaptation of the older Freundlich isotherm. Eq. (2.5) is a Sips isotherm written for Eq. (2.1).

$$\theta = \frac{[\mathrm{HCOOH}]\exp(\frac{CF(E-\overline{E^0})}{RT})}{[\mathrm{H^+}]\left(1+\frac{[\mathrm{HCOOH}]}{[\mathrm{H^+}]}\exp(\frac{CF(E-\overline{E^0})}{RT})\right)} \tag{2.5}$$

The form of the Sips isotherm (Eq. (2.5)) is very simple, requiring only two parameters C and $\overline{E^0}$. This isotherm has been applied in many cases, including molecular adsorption into molecularly imprinted polymers [24], H_2 on activated C [25], Cr(III) and Pb(II) on Takovite-Aluminosilicate nanocomposites [26], NO on titanium-silicate supported Cu [27] / Pt black [28], and H_2 and methanol on Rh and Ir electrodes [29]. This isotherm was fitted with great success to the formate adsorption data collected in this study, and the extracted parameters are reported.

2.2 Experimental

All solutions used Milli-Q water with a resistivity of >18 MΩ cm. The Au(poly) working electrode was made from Au wire (Alfa Aesar, Premion, 99.999%) sealed to a third of its length in teflon tape. This was immersed in fresh, hot piranha solution overnight and was then rinsed and soaked thoroughly in Milli-Q water before use. All

experiments made use of a reversible hydrogen reference electrode (RHE) separated from the working compartment by a Luer cap wetted with electrolyte. The Pt reference electrode was cleaned in fresh piranha solution overnight and rinsed thoroughly before use. A Pt wire counter electrode (Alfa Aesar, Premion, 99.997%) was used, and was flame annealed before experiments. Ultra-pure $HClO_4$ (Anachemia Science, Environmental Grade, 70%) was used in the preparation of supporting electrolyte solutions. Solutions were purged using 99.999% Ar (Praxair), and purging of the reference electrode compartment was done with 99.995% H_2 (Praxair). HCOOH was supplied by Fluka Analytical (puriss for HPLC, 50% HCOOH). The electrochemical cell used was glass, and all components in contact with the experimental solutions were glass or teflon. Cell components were heated in concentrated H_2SO_4 overnight and then rinsed thoroughly with Milli-Q water before experiments. This was also done for volumetric glassware used in preparing solutions. The RHE and working electrode compartment were filled with identical solutions (common $[HClO_4]$) at the beginning of experiments. Constant ionic strength was not maintained accross all experiments, due to the lack of suitable, non-adsorbing anion candidates. Candidates such as PF_6^- and BF_4^- were considered, but available purities were too low. Experiments at different [HCOOH]'s at a common $[HClO_4]$ were undertaken by sucessive spiking of HCOOH aliquots. Aliquots were added into an electrolyte of known % mass H_2O, HCOOH, and supporting electrolyte between experiments (into working electrode compartment only). Electrolytes were mixed by vigorous Ar bubbling for 3 min following additions. Electrochemical annealing was applied to the working electrode before and between all separate experiments, formic acid additions, etc. This entailed running 25-100 CVs from 0.2 to 1.85 V RHE at 200 mV/s. This was found to stabilize currents reliably. The surface area of the Au working electrode was determined using the Burshtein method [30] in 0.5 M H_2SO_4. The electrochemically active area was 0.45 cm^2, with a roughness factor of 2.3. Potential control and current measurement was handled by Gamry Reference 600 potentiostat/galvanostat. Only

data from the anodic sweeps of CVs was analyzed in detail.

Trends vs pH were assessed at variable $HClO_4$ vs RHE, meaning features that do not shift in potential have identical pH dependence as the reference electrode. All reported concentrations are in molal, abreviated "m" (or millimolal as "mm").

Fast sweep CVs ($\geq$15 V/s) were collected to emphasize capacitance and adsorption pseudocapacitance currents. This allows easier observation of formate adsorption peaks. Potential excursions were restricted from 0/0.2 to 1.3 V RHE. This excludes zones where appreciable hydrogen evolution or reconstruction due to Au oxidation takes place. Fast sweep CVs were corrected for IR drop post-collection, with the cell set up to minimize resistance. Resistances fell in the range of 0.5-14 Ω for supporting electrolyte $\geq$0.05 m, with the lowest supporting electrolyte concentration (0.01 m) giving a resistance of 70 Ω. For currents measured at 15 V/s, IR corrections typically fell in the range of 0 - 7 mV (maximum was 40 mV). Formate and perchlorate adsorption pseudocapacitances were separated from the double layer capacitance baseline by the following procedure: 1) HCOOH-free capacitance current densities above and below the perchlorate adsorption peak were used as a baseline without modification. 2) For potential regions where perchlorate adsorbs, the capacitance was approximated by a straight line. A linear function was fitted to 20 mV of current density-potential points directly before and after the perchlorate peak (giving a straight current density-potential line under the perchlorate peak). 3) Capacitance current density from steps 1-2 was subtracted from the raw current density potential data, leaving current density associated with perchlorate and formate adsorption. 4) Data above the potential threshhold where Au-oxide begins to form was rejected. All aforementionned current densities were measured at 15 V/s.

To characterize the adsorption of formate onto Au, fitting of formate adsorption peaks to the potential derivative of the Sips isotherm (Eq. (2.6)) was done in Maple 14 using the Statistics[Fit] command, a non-linear least-squares fitting routine. The formate adsorption peaks fitted were generated by the approach described in the

previous paragraph.

$$j = \sum_i \left(\frac{\nu F}{RT}\right) \sigma_{i,\max} C_i \left(\frac{\exp(\frac{C_i F(E-\overline{E_i})}{RT})}{1+\exp(\frac{C_i F(E-\overline{E_i})}{RT})} - \left(\frac{\exp(\frac{C_i F(E-\overline{E_i})}{RT})}{1+\exp(\frac{C_i F(E-\overline{E_i})}{RT})} \right)^2 \right) \quad (2.6)$$

The summation over i (different adsorbates) allows for multiple peaks to be fitted by Eq. (2.6). Three parameters are alloted per peak: i) $\sigma_{i,\max}$, in units of μC/cm^2. This parameter is the charge under the peak for adsorbing species "i". ii) C_i, dimensionless. $0 < C_i \leq 1$, with peak width increasing with lowered C_i (Langmuir isotherm at limit of $C_i = 1$). iii) $\overline{E_i}$, units of V. $\overline{E_i}$ is the peak potential for the adsorption of species "i", given by $\overline{E_i^0} - \ln(a_{\mathrm{HCOOH}}) + \ln(a_{\mathrm{H^+}})$, a function of the mean adsorption energy and activities of species involved in the adsorption equilibrium.

For $[HClO_4] : [HCOOH]$ less than $20 : 1$, two formate peaks are visible, and fitting is done in a two peak format. At or above this ratio, a single peak fitting function is sufficient. A special fitting procedure was used for the lowest $HClO_4$ concentration (0.01 m), where fits were found to perform poorly. The potential limit for this data set was lower than usual because of an lower potential adsorption onset. This led to most of the fitted data being far from the center of the formate peaks. Therefore, the current regime for fitting was restricted to 3/4 of the formate peak current or higher, allowing the fitting to focus on the peak region more exclusively. χ^2 values for single peak fits fell in the range from 1.8-5.3$\cdot 10^{-3}$. Dual peak fit χ^2 values fell between 4.35$\cdot 10^{-5}$ and 4.34$\cdot 10^{-3}$.

Coverage versus potential information extracted from Sips isotherm fits was used further to determine the rate law for formate oxidation. Four rate laws were devised from propositions in the literature. The first three models have potential independent rate constants. Eq. (2.7) is first order decomposition of formate, as observed on Pt by Feliu et al. [31]. Eq. (2.8) and Eq. (2.9) are the second order counterparts of Eq.

(2.7), inspired by Cuesta et al. [11, 15]. Eq. (2.8) allows reaction between common-type formates, while Eq. (2.9) adds in reaction between different formate types. Eq. (2.10) is first order decomposition of formate with rate limiting electron transfer (put forward by Crepy et al. [5]). These rate equations were then fitted to experimental oxidation current vs potential curves (using rate constants as fitting parameters). The four equations are given below.

$$j = \sum_i k_i \cdot \sigma_i(E) \tag{2.7}$$

$$j = \sum_i k_{ii} \cdot \sigma_{i,\max}^2 \cdot P_{ii}(E) \tag{2.8}$$

$$j = \sum_i k_{ii} \cdot \sigma_{i,\max}^2 \cdot P_{ii}(E) + \sum_i \sum_j \frac{1}{2} k_{ij} \cdot \sigma_{i,\max} \cdot \sigma_{j,\max} \cdot P_{ij}(E) \tag{2.9}$$

$$j = \sum_i k_i \cdot \sigma_i(E) \cdot \exp\left(\frac{\beta_i F \cdot E}{RT}\right) \tag{2.10}$$

Here, $\sigma_i(E)$ is the charge of type i formate versus potential (Eq. (2.6) integrated with respect to potential). $P_{ij}(E)$ is the probability of formate type i and type j occupying adjacent sites as a function of potential, and is related to $\sigma_i(E)(P_{ij}(E) \neq \theta_i(E) \cdot \theta_j(E)$ as in Langmuir case, see Theory: Sips Isotherm in Supporting Information for details).

2.3 Results

For an electrochemically reversible adsorption reaction, currents associated with adsorption are expected to be linear with sweep rate (ν), and appear as a peak. Capacitance currents scale identically with sweep rate, and are experimentally inseparable from adsorption currents. In this case, the sum of capacitance and adsorption currents should become much greater than the sweep rate independant oxidation currents (see 2.3.3) at large ν. Formate adsorption onto Au in $HClO_4$ solution was observed by

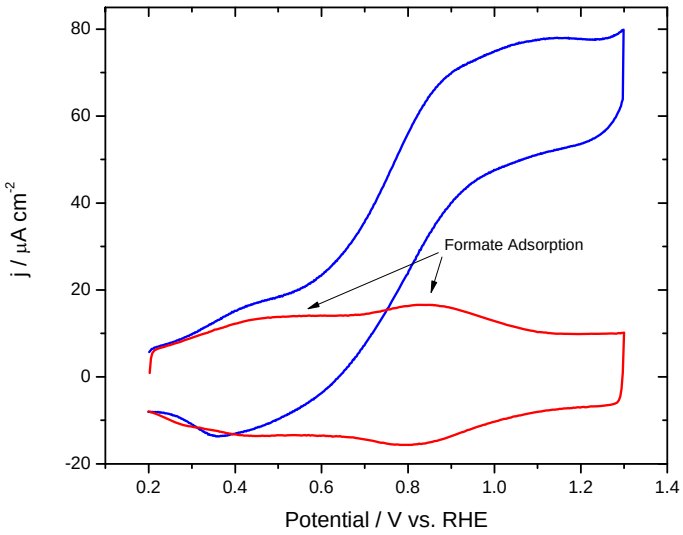

Figure 2.1: Current densities measured in 0.1 m $HClO_4$ / 0.1 m HCOOH. j_{tot} (blue) $j_{\text{Cap.+Pseudocap.}}$ (red) apply at 0.2 V/s. $j_{\text{Cap.+Pseudocap.}}$ measured at 15 V/s, divided by 75.

setting ν for CVs to 15 V/s or greater (often referred to as "fast sweep" CVs). The measured capacitance / adsorption current can be scaled down to its value at a lower ν to show oxidation current and adsorption / capacitance current separately (Fig. 2.1).

Fig. 2.1 reveals the coincidence of formate adsorption and oxidation current onsets. Observation of adsorbed intermediates via fast-sweep voltammetry has also been reported for formate adsorption onto Pt [31], and methanol adsorption onto Rh and Ir [29].

2.3.1 Perchlorate Adsorption in $HClO_4$ Solution

Current peaks associated with perchlorate adsorption were observed in HCOOH-free CVs collected over a wide ν range (0.2 - 100 V/s) and perchloric acid concentrations

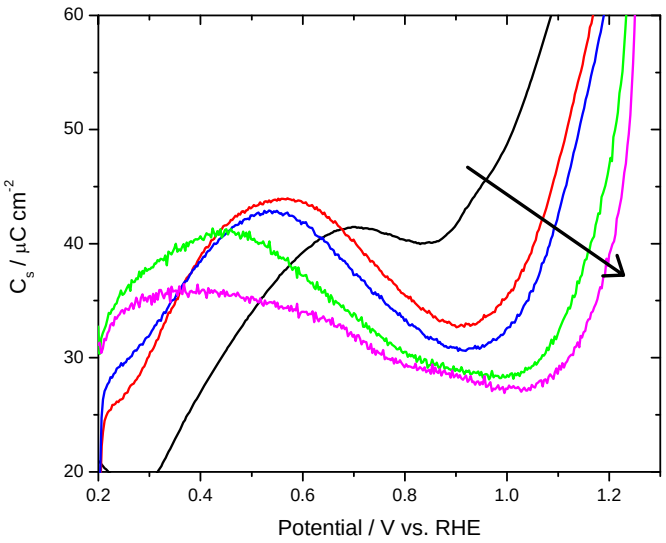

Figure 2.2: Perchlorate adsorption peaks in anodic 15 V/s potential sweeps. $[HClO_4]$ = 0.01, 0.05, 0.1, 0.5 and 1 m. Arrow indicates increasing concentration. Rising current at > 1 V RHE is due to onset of Au oxide formation.

(0.01 - 1 m). Potentials of these peaks are in close agreement with features similarly assigned in a study by Conway et. al. [17] on Au(111), Au(110), and Au(100). The potential of this peak decreased at -133 mV/ log$[HClO_4]$ against RHE at 15 V/s (seen in Fig. 2.2). For a reaction following the stoichiometry outlined in Eq. (2.3), a slope of -120 mV/ log$[HClO_4]$ is expected if adsorption is reversible (observed by Conway et. al.). The lack of dependence of this peak's potential on sweep rate does suggest near reversibility. The slope below -120 mV/ log$[HClO_4]$ has been attributed to changes in the activity coefficient of perchlorate with supporting electrolyte concentration. Adsorbed perchlorate charge densities observed during experiments are very low (average = 5.63 $\mu C/cm^2$, see Sec. 2.2 for details). Full width at half maximum (FWHM) of perchlorate peaks are estimated at 350 mV.

2.3.2 Formate Adsorption in $HClO_4$ Solution

Current peaks for formate adsorption are visible in fast sweep CVs, as shown in Fig. 2.3**.** Sweeps of 15-100 V/s CVs are superimposable upon being subjected to post-run IR drop correction and normalization by sweep rate. This is true in the full formic acid concentration range investigated (0.005 - 1 m). The superposition of the fast sweep rates is indicative of formate adsorbing very quickly on Au (charge versus potential is not a function of time allowed for adsorption). In short, no mass transport or kinetic limitations on adsorption rate are observed. This strongly suggests effectively reversible adsorption. The important conclusion drawn is that formate adsorption could never be rate limiting during formic acid oxidation, given the comparatively low maximum current densities associated with the oxidation step of this reaction (Fig. 2.8 (A)). The only behaviour that disagrees with effectively reversible adsorption is the slight hysteresis of adsorption/desorption peaks (desorption peak pot. $<$ adsorption peak pot.). This difference in peak potentials is unaffected by sweep rate. This hysteresis is perhaps due to slight reconstruction of the Au substrate during sweeps.

The adsorption peaks are very broad at 350-400 mV FWHM, in spite of the speed of the associated reaction. A Langmuir adsorption isotherm predicts a half height width of 91 mV at 298 K. This extra width could be due to repulsive adsorbate-adsorbate interactions or the heterogeinity of the Au (non-degenerate adsorption sites). If lateral interactions were the sole cause, peak symmetry would be expected to break down before the observed widths were reached. Since these peaks are symmetrical, we assume the larger width is due to electrode heterogeneity.

More information can be gleaned from fast sweep results by altering solution composition. Adsorption peaks shift to lower potentials with increased [HCOOH] and decreased [$HClO_4$]. Single species adsorption peaks should shift to lower potentials with increased concentration of the adsorbing species, but without change in size or shape. A reproducible observation is a low potential shoulder on formate adsorption

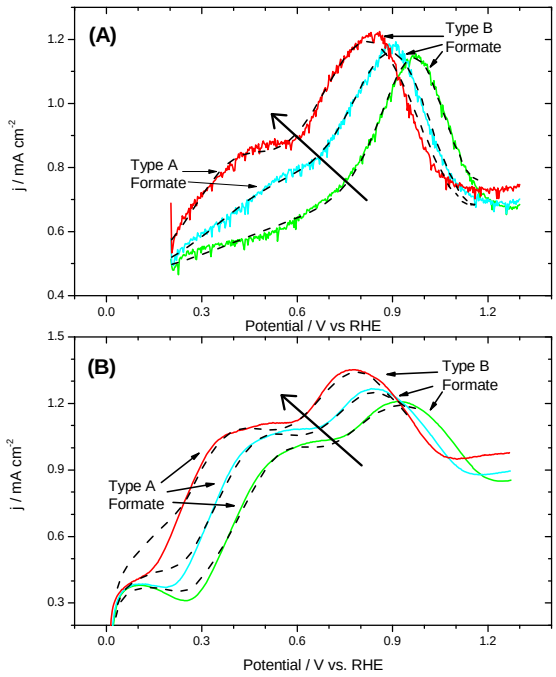

Figure 2.3: 15 V/s anodic sweeps at (A) 1 m $HClO_4$ or (B) 0.01 m $HClO_4$ with 10 mm, 0.1 m or 1 m [HCOOH].Arrow indicates increasing concentration. Dashed black lines represent Sips isotherm fits of formate adsorption current density + capacitance current density.

currents at [HCOOH]:[$HClO_4$] > 0.05. This shoulder grows into a full second peak as this ratio rises. For clarity, the low potential peak will be referred to as type A formate. The high potential peak (observed for all [HCOOH]:[$HClO_4$]) will be referred to as type B formate. The type A formate peak has been assigned to adsorption on a different variety of site than type B formate. Overall these results show a rise in maximum formate coverage with [HCOOH]:[ClO_4^-], and are supported by the increase in maximum faradaic current as a function of [HCOOH]:[$HClO_4$] (Fig. 2.8). This supports the theory that adsorbed ClO_4^- competes with formate for sites on the surface.

The presence of two overlapping formate peaks made it difficult to accurately judge the peak potentials, deposited charge, and widths of individual peaks. In order to accomplish this, fast sweep CVs were corrected for capacitance current and fitted to the Sips isotherm (see Sec. 2.2 for details). This served to deconvolute the peaks and yielded three parameter values per peak: $\sigma_{i,\max}$, C_i and $\overline{E_i}$ (related to peak charge, width and peak potential, respectively). $\sigma_{i,\max}$ represents the charge under formate peak i. $\sigma_{A,\max}$ values extracted are summarized in Fig. 2.4.

A noteworthy observation is the linearity of $\sigma_{A,\max}$ vs log[HCOOH], and the offset of the line to lower charges with increasing [$HClO_4$] for 0.01 m $\leq$ [$HClO_4$] $\leq$ 0.1 m. The slope of these lines is similar across the three lowest supporting electrolyte concentrations. The deviation from this behaviour for 0.5 and 1 m [$HClO_4$] is attributed to the flexibility of the peak fits. In these data sets, type A formate peaks are very small and heavily overlapped by the type B peak. The fitted values for $\sigma_{A,\max}$ rise at the expense of $\sigma_{B,\max}$ (a much larger value) in these cases (the growth of the type A peak is obvious to the eye, but not captured by the fit, see Fig. 2.3 (A)). $\sigma_{B,\max}$ typically takes on a constant value and does not show a universal trend with [$HClO_4$] or [HCOOH]. The average value of $\sigma_{B,\max}$ extracted was 21.8 $\pm$ 2.2 $\mu C/cm^2$.

C_A and C_B remain mostly fixed across all solution compositions investigated, without any universal trends in their values. This supports the theory that electrode

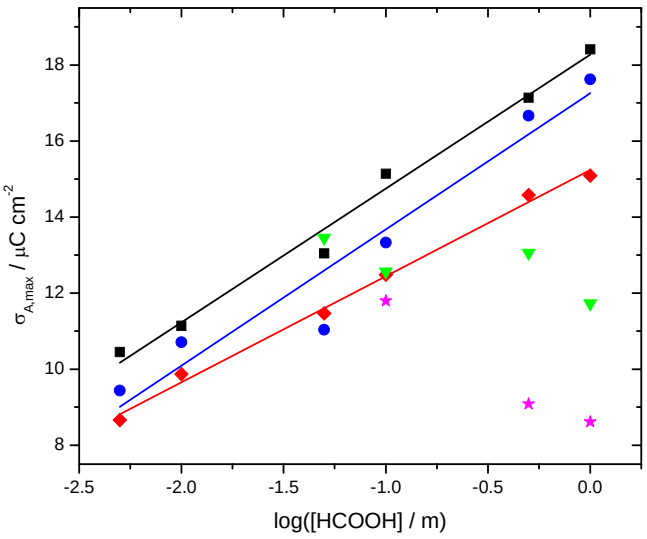

Figure 2.4: $\sigma_{A,\max}$ from sips isotherm fits of type A formate peaks. $[HClO_4] = 0.01$ (■, black), 0.05 (●, blue), 0.1 (♦, red), 0.5 (▼, green), and 1 m (★, pink). Information on linear trends included in Supporting Information under Additional Information.

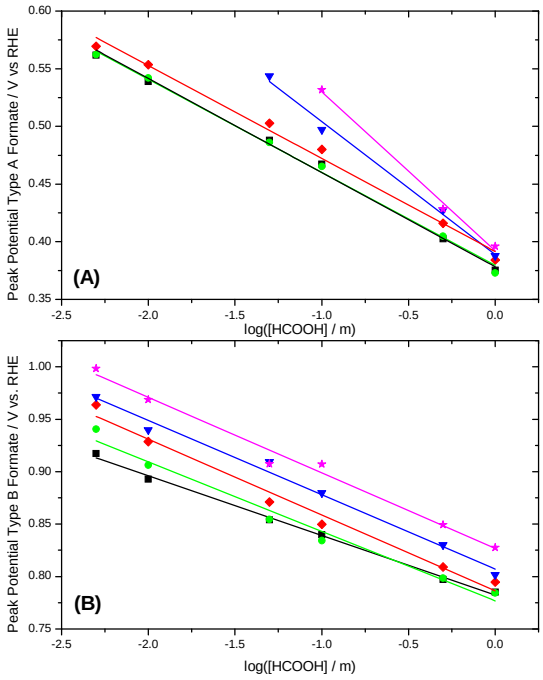

Figure 2.5: Fitted peak potentials for (A) type A and (B) type B formate from Sips isotherm fits. $[HClO_4] = 0.01$ (■, black), 0.05 (●, green), 0.1 (♦, red), 0.5 (▼, blue), 1 m (★, pink). Linear trends summarized in Supporting Information.

heterogeneity is responsible for the large peak widths (changing total coverage of formate would alter peak widths if strong lateral repulsions were in effect). C_A averaged 0.259 ± 0.030, corresponding to a FWHM of 354 mV. C_B averaged 0.226 ± 0.017, corresponding to a FWHM of 398 mV. More detailed information on $\sigma_{B,\max}$, C_A, and C_B has been included in the Supporting Information, under Additional Information, Formate Sips Isotherm Parameters.

Fitted peak potentials for formate adsorption are summarized for both type A and type B formate in Fig. 2.5.

Peak potentials (vs RHE) are linear vs log[HCOOH], as might be predicted for

a reversible adsorption reaction. For both peaks, peak potential is independent of $[HClO_4]$ at high [HCOOH]:$[HClO_4]$. This is an indication that competition for sites with perchlorate no longer affects peak potential (formate adsorption dominates). Further, since these measurements were conducted against RHE, the coincidence of peak potentials at different $[HClO_4]$ and fixed [HCOOH] indicates a -59.2 mV/pH trend in the peak potential (peaks shift with same sensitivity vs pH as reference electrode). Type A formate peak potential vs log[HCOOH] slopes changed from -80 to -137 mV as $[HClO_4]$ decreased. Type B formate peak potential vs log[HCOOH] slopes changed from -57 to -72 mV as $[HClO_4]$ decreased.

2.3.3 Formate Oxidation in $HClO_4$ Solution

Oxidation Current Densities versus Potential

Slower sweep CVs at 200 mV/s provide a measurement of oxidation current (j_{ox}, from reaction (2.2)) vs potential, when corrected for capacitance and adsorption currents. Values of j_{ox}'s were comparable with those measured by Koper et al [14], and some examples are displayed in Fig. 2.6. j_{ox} was measured at 5 - 1000 mm HCOOH in 10 - 1000 mm $HClO_4$. j_{ox} vs potential curves rise from 0 (0 - 0.3 V RHE) to a constant value (ca. 1.1 - 1.2 V RHE), with current onsets and maxima improving with increased [HCOOH] or decreased $[HClO_4]$. This is easily rationalized, as j_{ox} onsets coincide well with the onset of formate adsorption in the faster sweep CVs. j_{ox} rises with formate coverage, and reaches a plateau once maximum coverage is achieved. Cuesta et al. [11,15] also observed that j_{ox} depends only on formate coverage, implying a chemical rate limiting step (potential independent rate constant).

Electrolyte stirring does not affect j_{ox}, indicating a lack of mass transport effects. Alteration of sweep rate also does not change j_{ox}, as previously reported [12, 14]. Some typical j_{ox} vs potential curves are included (Fig. 2.6), at different [HCOOH] and $[HClO_4]$. Note that the slight anomalies in current above 1.2 V are thought to

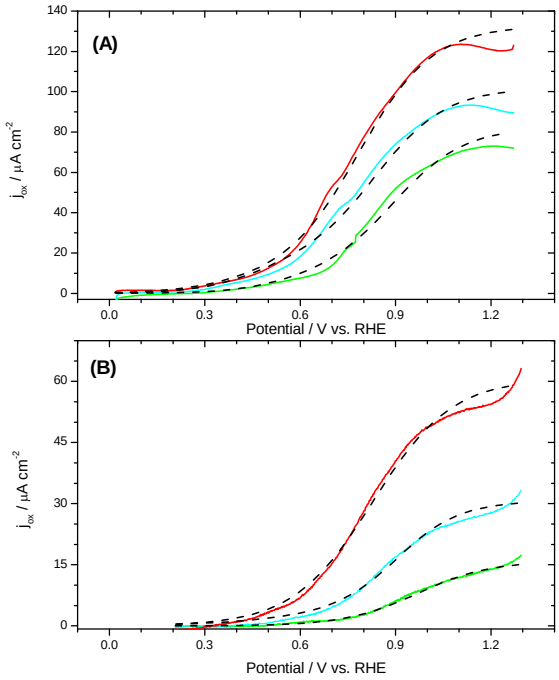

Figure 2.6: Potential dependence of j_{ox} in (A) 0.01 m $HClO_4$ and (B) 1 m $HClO_4$ at [HCOOH] = 0.01 (green), 0.1 (cyan), and 1 m (red). Dashed black lines correspond to fits of $j_{ox} = kA \cdot \theta_A + kB \cdot \theta_B$ with the coverages found by fitting Sips Isotherms.

be due to the onset of Au oxide adsorption, which reacts with formate [6] and may perturb formate coverage.

2.3.4 Fitted Models of Oxidation Current Density

Included in Fig. 2.6 are results fitted to a model using the coverage-potential information from the fitted Sips isotherms. For details on how fitting was done see Sec. 2.2. Fitting of the models was undertaken to discern the reaction order of formate and find the rate constant(s). Of the four models fitted, only the most well behaved model (Eq. (2.7)) is plotted. Fitting Eq. (2.7) yielded χ^2 values of $8.3{\cdot}10^{-5}$ to $1.5{\cdot}10^{-3}$ (av-

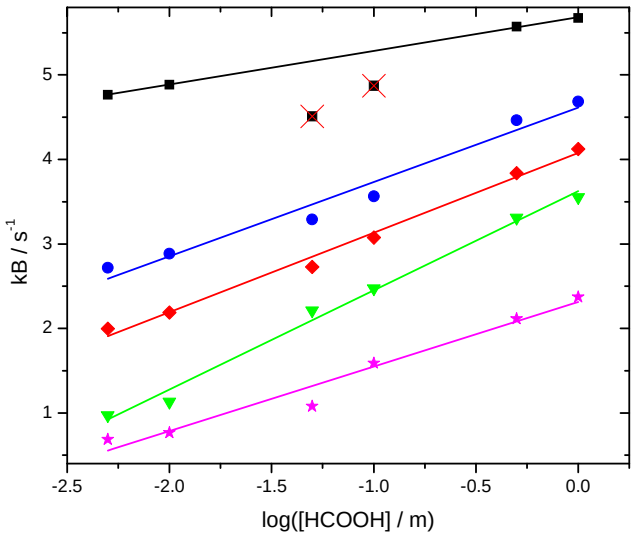

Figure 2.7: Value of kB (effective rate constant for oxidation of type B formate) against log[HCOOH] for $[HClO_4]$ = 0.01 (■, black), 0.05 (●, blue), 0.1 (♦, red), 0.5 (▼, green), 1 m (★, pink).

erage = $2.6{\cdot}10^{-4}$), and qualitative agreement with experimental results. The only consistent deviation is the overestimation of current densities near the plateau. This is likely due to Au oxide formation decreasing formate coverage in the experimental system. These fits show type A formate as being far less active than type B, with a rate constant of $kA = (5 \pm 3){\cdot}10^{-1}$ s^{-1}. The large standard deviation in this number is probably due to the small influence type A formate oxidation has on the overall fit. The rate constant for type B formate (kB) is larger, but systematically changes with solution composition (Fig. 2.7), implying it is in fact an effective rate constant. The linearity of kB with log[HCOOH] is an obvious indication of a higher order dependence on formic acid (or derivative). For a more thorough interpretation, refer to Sec. 2.4.3.

Eq. (2.8) and Eq. (2.10) provide the worst fit to the data both qualitatively and quantitatively. Values of χ^2 range from $1.8{\cdot}10^{-2}$ to $3.5{\cdot}10^{-4}$ (average = $6.6{\cdot}10^{-4}$)

for Eq. (2.8) and $1.4{\cdot}10^{-2}$ to $7.2{\cdot}10^{-5}$ (average = $1.7{\cdot}10^{-3}$). Fitted curves for these models tend to cross the experimental curve at several points only, rarely showing close agreement over an extended potential range. Eq. (2.10) fails to show a current plateau.

Fitting experimental data to Eq. (2.9) produces mediocre results. This fit performs either slightly better or much worse than Eq. (2.7), with χ^2 ranging from $3.8{\cdot}10^{-3}$ to $7.2{\cdot}10^{-5}$ (average = $5.1{\cdot}10^{-4}$). This model predicts that $> 99\%$ of all current flows due to reaction of type A and type B formate, and not second order reaction of common type formate. Rate constants show some scatter.

Current Densities vs [HCOOH] and [$HClO_4$]

Plateau current densities (and in fact j_{ox}'s at all potentials) increase with [HCOOH] and decrease with [$HClO_4$]. Maximum j_{ox}'s have been summarized in Fig. 2.8 **(A)**, and are linear with log[HCOOH] above 20 μA/cm^2. Lines for j_{ox} vs log[HCOOH] at different [$HClO_4$] are offset in j_{ox}, but parallel (j_{ox} vs log[$HClO_4$] also linear). This type of behaviour is seen irrespective of the selected potential, so long as current density remains > 20 μA/cm^2. Also, Fig. 2.8 (B) contains a summary of $j_{ox} \leq 3$ μC/cm^2 at 0.4 V (limit of low current density), where oxidation of type A formate is expected to be dominant. Data from Fig. 2.8 will prove critical in discerning the reaction order of the adsorbed formate species.

2.4 Discussion

A scheme fully justifying the adsorption and oxidation mechanism findings in this work has been provided (Fig. (**??**)), and will be explained in the following discussions.

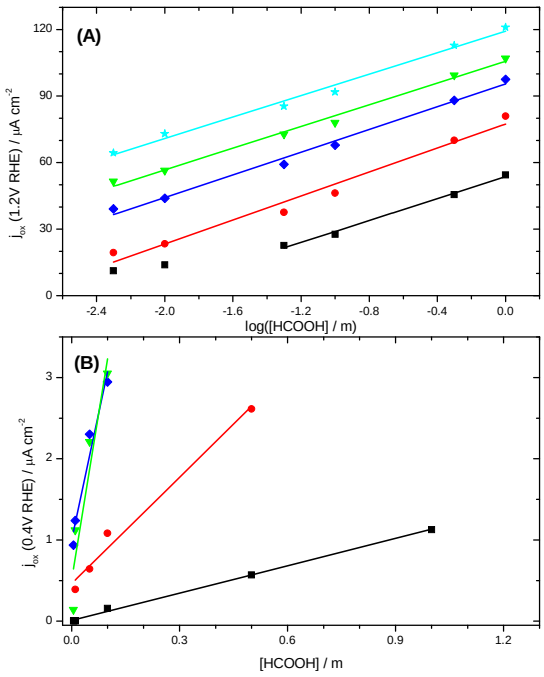

Figure 2.8: (A) j_{ox} at 1.2 V RHE as a function of log[HCOOH]. (B) All $j_{\text{ox}} \leq 3$ μA/cm^2 at 0.4 V RHE. [$HClO_4$] = 0.01 (★, cyan), 0.05 (▼, green), 0.1 (♦, blue), 0.5 (●, red), 1 m (■, black). Parameters for linear trends are included in Supporting Information, under Additional Information.

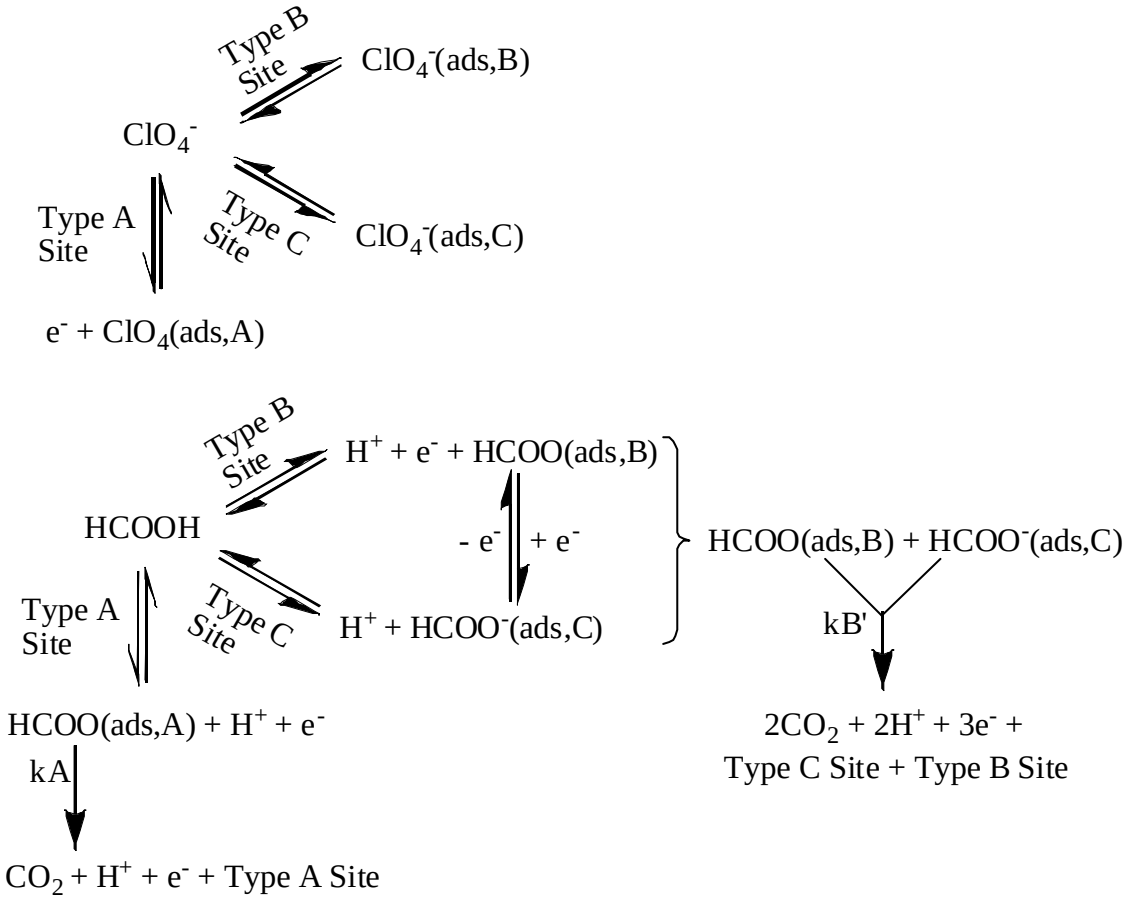

Figure 2.9: Overall reaction scheme deduced in this work. Three distinct perchlorate and formate adsorption equilibria are proposed, with each type of formate undergoing subsequent oxidation to CO_2.

2.4.1 Perchlorate Adsorption in $HClO_4$ Solution

Some workers have refuted the idea of specific adsorption of perchlorate, as done by Stimming et al [16] for Au(poly). A lack of shift of the PZC on very smooth Au(poly) electrodes with [$HClO_4$] was cited as evidence. This was assessed in the presence of a junction potential which was approximately corrected for. Some other studies contradict these results, and draw evidence from a wide variety of techniques. EQCM mass:charge ratios on Au(poly) and Au(111) were cited by Wantanbe et al. [20] as evidence for perchlorate adsorption. SNIFTIRS was used on Au(poly) electrodes to show that surface excesses of perchlorate are higher than expected based on the Gouy-Chapman model [21], increasingly so with rising potential. Kolb [19] and Santos [18] showed shifts in the PZC with [$HClO_4$] on several single crystal faces, although junction potentials were not corrected for. Further, peak potential for reconstruction of Au was found to shift with $HClO_4$ [18]. Conway et al. studied several single crystal Au faces, and in each instance rationalized onset potentials for Au oxidation according to strength of perchlorate adsorption. Distinct adsorption current peaks were also seen in the double layer for Au(111) and (110), and peak shifts with [$HClO_4$] could be predicted by the stoichiometry outlined in Eq. (2.3). Work published by Smalley using the indirect laser induced temperature-jump (ILIT) method contained data consistent with the specific adsorption of perchlorate onto Au(111) [22].

As mentioned, Stimming et al reported no specific adsorption of perchlorate on Au(poly), at a reported roughness factor of no greater than 1.1 [16]. The roughness factor in this work is much higher at 2.3, and it is suggested that the roughness of the Au surface is partially responsible for perchlorate adsorption. Atomic level roughness introduced by our electrode cleaning procedure may expose "high energy" sites susceptable to strong perchlorate adsorption. It is thought to be unlikely that the adsorption peaks seen are due to adsorption of trace level impurities in the supporting electrolyte. Based on the amount of charge deposited and the maximum time interval

over which the deposition takes place (at 15 V/s), a minimum concentration of ca. 70 μm would be required for a reversibly adsorbing species to give the observed adsorption peak (under diffusion conditions). Adsorbing impurities in the perchloric acid (sulfate, chloride, etc.) are present at levels much lower than what is required to give the observed peaks, on the order of ppm in the concentrated $HClO_4$.

Another possible phenomenom that might cause an adsorption peak is the low potential adsorption of OH on the surface of Au. This has been seen on Au(100) by Conway et al [17], who report that this adsorption is reversible and accompanied by the transfer of 1/2 e^-. The peak potentials observed in this study have a dependence of 133 mV RHE/log[$HClO_4$]. This is more than twice what would be expected for OH adsorption with transfer of 1/2 e^- (ca. 60 mV RHE/log[$HClO_4$]), but only 10% higher than the ca. 120 mV RHE/log[$HClO_4$] expected for perchlorate adsorption according to Eq (2.3). Based on this comparison it seems safe to reject low potential adsorption of OH.

Given the size of a perchlorate anion, a max coverage of 20-25% of a monolayer might be considered reasonable. This has been supported by EQCM studies in $HClO_4$ solutions, on Au(111) and Au(poly) [20], where double layer charging was assumed to contribute 20 $\mu F/cm^2$ across the double layer region. Charges observed in the present study are much lower than estimates suggest (average = 5.63 $\mu C/cm^2$, see Sec. 2.2 for details). This charge might not be unreasonable, since not all crystal faces of a Au(poly) surfaces oxidatively adsorb perchlorate. Conway et al. [17] have shown that perchlorate adsorption onto Au(100) does not incur charge transfer, while adsorption on Au(111) and Au(110) displays charge transfer. If the polycrystalline electrodes used in this study have an appreciable fraction of Au(100) or related surfaces, this might explain the low overall charge density. Furthermore, the perchlorate charges reported by Conway et. al. on Au(111) and Au(110) fell in the range of 5-10 $\mu C/cm^2$. A possible source of error in measuring adsorbate charge (especially for small total charge) is the choice of a capacitance baseline. This has been done inconsistently in

the literature.

2.4.2 Formate Adsorption in $HClO_4$ Solution

Fast voltammetry experiments show formate adsorption onto Au(poly), with effectively reversible adsorption onto at least two classes of sites (type A and type B sites). The adsorption peaks are very wide (354 or 398 mV FWHM), collectively covering most of the double layer region. Adsorption and desorption are both observed (in anodic and cathodic sweeps respectively). The $\overline{E^0}$ values for each adsorption equilibrium are 0.374 V (type A formate) and 0.785 V SHE (type B formate). Peak potentials of type B formate shift with pH (-59.2 mV/pH) and [HCOOH] (-57 to 72 mV/decade). The stoichiometry of Eq. (2.1) predicts slopes of -59.2 mV, confirming that it is indeed formate being observed ($1e^-$:$1H^+$:1HCOOH confirmed). Type A formate behaves similarly, exhibiting a -59.2 mV/pH and -80 to -137 mV/log[HCOOH] shift. While the pH dependence is easily justified, the formic acid dependence implies more complicated behaviour. Deviation of slopes $<$ -59.2 mV/log[HCOOH] has been attributed to competition with perchlorate for surface sites, although the reason for this is not clear.

Lower HCOOH to $HClO_4$ ratios have been shown to decrease the coverage of type A formate, which further supports competition of perchlorate and formate for Au sites. Peak potentials (vs RHE) of type A and type B formate are affected by [$HClO_4$] at lower [HCOOH]:[$HClO_4$]. Growth of the type A formate peak with [HCOOH]:[$HClO_4$] can be predicted in a model where perchlorate and formate adsorb on the same sites according to the stoichiometry of Eq. (2.1) and Eq. (2.3) (and maximum coverage of formate is greater than maximum coverage perchlorate). Note that this sort of model predicts the linear increase in peak charge with log[HCOOH] extracted from peak fitting (Fig. 2.4). An example simulation is provided in Fig. 2.10. Details on the execution of this simulation are included in the Theory: Sips

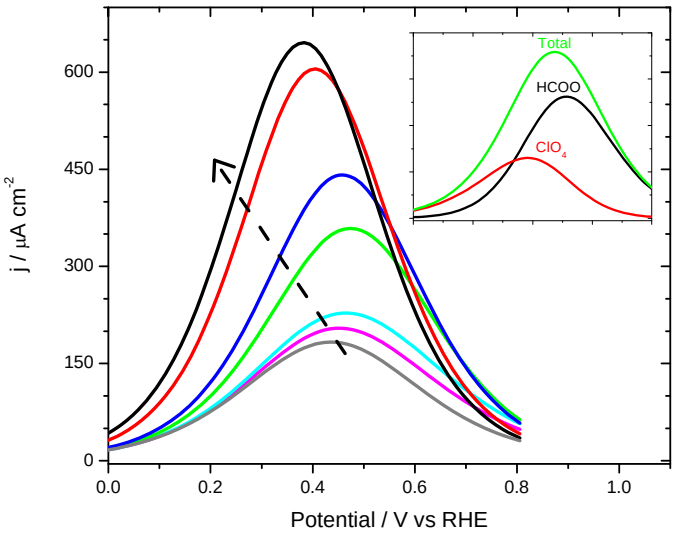

Figure 2.10: Simulated total current density for potential-dependent perchlorate and formate adsorption onto the same sites. Simulations run at 0.5 m $HClO_4$ + 1, 0.5, 0.1, 0.05, 0.01, 0.005, or 0 m HCOOH. Arrow indicates increasing concentration. Inset: Deconvolution of peak (0.05 m HCOOH) into perchlorate and formate contributions.

Isotherm section in Supporting Information. This implies that at least some of the observed perchlorate adsorption (Fig. 2.2) is taking place on the same sites as type A formate.

In contrast type B formate peak size is fixed across all data sets. This peak still moves to higher potential with [$HClO_4$] at low [HCOOH]:[$HClO_4$], indicating a different sort of competition for surface sites. The simplest model to match this behaviour is potential *independent* perchlorate adsorption on the same sites as potential *dependent* formate adsorption (details in Theory: Sips Isotherm section in Supporting Information), and is illustrated in Fig. 2.11. In such cases, peak shape and size for formate are not expected to change, but movement to higher potentials with rising [$HClO_4$] (when the ratio [HCOOH]:[$HClO_4$] is sufficiently low) is expected. Conway et al. showed that perchlorate adsorption onto Au(100) gave no e^- transfer. It would

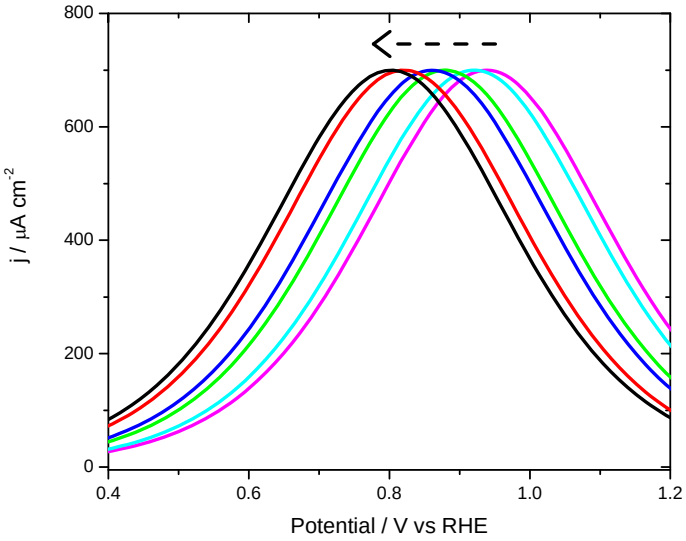

Figure 2.11: Simulated current density for potential-dependent formate adsorption onto same sites as potential-independent perchlorate adsorption (Case ii)). Simulations run at 0.5 m $HClO_4$ + 1, 0.5, 0.1, 0.05, 0.01 or 0.005 m HCOOH. Arrow indicates increasing concentration.

be expected that adsorption onto Au(100) or similar surfaces would display far lesser potential dependence than on Au(111) and Au(110). It is tentatively proposed that type A formate adsorbs onto Au(111)- or Au(110)-like facets, with type B formate adsorbing onto Au(100)-like facets.

No previous studies have directly measured maximum formate coverage on Au. Some estimates can be provided from studies done on other metals. A fast sweep voltammetry study by Feliu et al. [31] in HCOOH / $HClO_4$ medium provided an estimated formate charge of ca. 90 $\mu C/cm^2$ (ca. 87 $\mu C/cm^2$ on Au), near half a monolayer. This result applies to Pt(111) and Pt(554) surfaces. Formate adsorbs at much lower potentials than perchlorate on these surfaces. This implies that the coverages measured are the true saturation values, undiminished by coadsorbed perchlorate. Another estimate can be provided from Ni(110) UHV studies, where reports

by Jones and coworkers [32,33] turned up similar results. Formate was found to bond in a bridged fashion, filling out a c(2×2) overlayer on the surface. On an equivalent Au surface, this would imply 68 $\mu C/cm^2$ at saturation. In general, saturation coverages of 0.42-0.5 ML seem to be common. In this study, high potential formate charge fell in the range of 21.8-40.3 $\mu C/cm^2$ (0.108-0.199 ML). The saturation value for type B formate can be confidently assigned at 21.8 $\mu C/cm^2$, but the saturation value for type A cannot be so easily determined. Type A formate coverage did not reach a maximum value in the parameter space investigated, indicating perchlorate still occupied some type A sites. See also Sec. 2.4.3, where evidence for a third, fully charged version of formate is found.

The oldest theories in the literature on formate adsorption onto Au come from Crepy et al. [5], and are accepted by several other authors [8,14]. Formate adsorption was taken as being electrochemically reversible, with formic acid acting as the adsorbing species. Another model arose from work by Cuesta et. al. [11,15], who proposed irreversible adsorption from dimeric HCOOH. "Irreversible" applies in two senses here. The first is that desorption of formate was assumed impossible (only removed via oxidation). The second is that adsorption was thought to be slow (electrochemically irreversible). Another study that agrees with an electrochemically irreversible adsorption step was carried out by Wu et al. [10], using a potential step method. This method is questionable because of reliance on Au oxide reduction proceeding in the same way with or without HCOOH, in spite of its proven reactivity with Au oxides [6]. Experimental evidence here agrees with the propositions by Crepy et al. [5]. Where conclusions deviate from older studies, these outstanding issues will be discussed.

All past studies show j_{ox} and formate coverage rising over most of the double layer region [5,8,11,14,15]. While broadening of an adsorption peak (>91 mV FWHM for Langmuir model) can take place due to slow adsorption, this is only one possible explanation. It can also have a thermodynamic origin, if a reversible adsorption reaction takes place over a very wide potential range. The Langmuir isotherm and

most common isotherms inherently assume that all sites on the surface bind formate with equal energy, and often do not consider repulsive or attractive interactions. The reality is that the many types of inequivalent sites on a polycrystalline surface will have a statistical distribution of binding energies for formate, thereby broadening the adsorption peak. Furthermore, it is common even for uncharged adsorbates to experience lateral repulsions at close proximities, widening the potential or concentration regime over which adsorption occurs. As was remarked upon earlier, peak widths are not a function of maximum coverage and peaks are symmetrical. This supports the hypothesis that electrode heterogeneity is responsible for peak width. This width was seen and remarked upon by Cuesta et al. as being unexpected in the absence of slow adsorption [11, 15].

Another point raised that is not strongly supported by this work is the idea of formate adsorbing exclusively from the dimeric form of formic acid [11, 15]. This hypothesis was adopted to explain an observed second-order dependence of rate on formate in the presence of slow adsorption. It was proposed that two formates would be produced on adjacent Au sites from a single adsorbing dimer. These would then react (due to their proximity) to give two units of CO_2. All that is required for second order oxidation is for two formates to be present on adjacent catalytic sites. One could imagine that two formates could adsorb from two monomeric HCOOH's on adjacent sites, or adsorb on non-adjacent sites then undergo surface diffusion to become adjacent. While adsorption from the dimer is possible, it is not required to explain experimental observations.

2.4.3 Oxidation Currents in $HClO_4$ Solution

The ultimate goal of this section is to discern the reaction order and rate constant in Eq. 2.2. Assessment of the models fitted to j_{ox} vs potential traces will allow this. Firstly, Crepy et. al.'s proposed mechanism (represented by Eq. 2.10) does not fit

adequately to the data, as it does not allow for j_{ox} to plateau at high potentials. A plateau is only possible if the rate determining step is purely chemical (no electron transfer), as put forward by Cuesta et al. [11, 15].

Equations (2.7)-(2.9) are variations on this theme, differing only in the reaction orders used. Although Cuesta and coworkers suggested a second order dependence on adsorbed formate, Eq. (2.8) and (2.9) (both second order mechanisms) do not perform well. Qualitative disagreement with the data and inconsistent rate constants arise for Eq. (2.8). Better agreement between Eq. (2.9) and the data was achieved, but rate constants were very inconsistent and followed unpredictable trends versus solution composition. It must be admitted that assessment of reaction rates for reaction orders >1 are laden with many assumptions. These assumptions include: assuming that the Sips isotherm truly describes formate adsorption on a microscopic scale (not just the surface as a whole), no significant lateral interactions exist, fixed ratio of type A and type B sites exists on all patches of sites (see Theory: Sips Isotherm in Supporting Information for details) and that there is a random arrangement of these two site types on the surface. Therefore, it is difficult to categorically rule out second order mechanisms.

Eq. (2.7) (first order formate dependence) fitted adequately, showing typical first order behaviour for type A formate and more exotic behaviour for type B (rate constant shifts with log[HCOOH]). Note that first order behaviour has also been used to explain the activity of Pt(111) and Pt(554) catalysts [31].

The simple first order behaviour of type A formate is evident in the data under certain conditions (Fig. 2.8 (B)). At 0.4 V, 92 - 97 % of formate will be type A (j_{ox} predominantly first order). Eq. (2.5) shows that linearity of coverage with [HCOOH] is expected at fixed potential for low coverages, with the slope increasing at raised pH. For first order oxidation of formate, j_{ox} should behave identically (seen in Fig. 2.8 (B)).

At higher potentials, j_{ox} is dominated by oxidizing type B formate, e.g., 94 - 100% of j_{ox} at 1.2 V. Note the qualitative similarity of fitted rate constant (Fig. 2.7) and j_{ox} (Fig. 2.8 (A)) at 1.2 V vs solution composition. Since the high-potential coverage of type B formate is fixed accross all data sets, this is to be expected. It is worth considering why the fitted rate constant for type B formate changes as it does with solution composition. Firstly, kB values extracted from fitting are not fixed, implying an effective rate constant (actual rate constant times activity of some other species, a_x, see Eq. (2.11)).

$$kB = kB' \cdot a_x \tag{2.11}$$

From Fig. 2.7 and Fig. 2.8 (A) it is clear that a_x increases linearly with log[HCOOH] and drops with log[$HClO_4$]. This is characteristic of coverage for potential independent adsorption of formic acid or formate (near the middle of the coverage range). For the sake of simplicity, it will be assumed this new species is a third variety of formate (type C). For this proposal to work, any perchlorate competing with type C formate for sites would also need a potential independent equilibrium constant (Eq. (2.4), as for type B sites). An example of the proposed coverage vs concentration behaviour is shown in Fig. 2.12. Refer to the Theory: Sips Isotherm section in the Supporting Information for details on the execution of this simulation. A further restriction is that surface sites for type C formate must be distinct from those occupied by type B and type A. It is logical to assert that these sites are on the same facets of Au(poly) as type B, as these two formate species react together and compete for sites with fully charged perchlorate. The proposed equilibrium for type C formate is given in Eq. (2.12).

$$HCOOH \rightleftharpoons HCOO^-(ads, C) + H^+ \tag{2.12}$$

If a_x is the coverage of a third type of formate, then the oxidation of type B

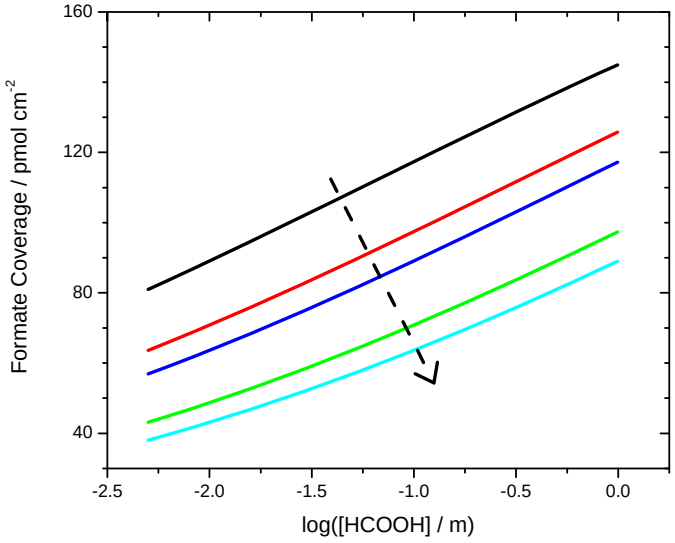

Figure 2.12: Simulated formate coverage when formate and perchlorate adsorb onto the same sites without charge transfer (Case iii)). $[HClO_4] = 0.01$, 0.05, 0.1, 0.5 and 1 m. Arrow indicates increasing concentration.

formate would be similar to the second order reaction proposed by Cuesta et. al. (oxidation of two formates via reaction with each other, rate limiting chemical step, Eq. (2.13)).

$$HCOO^-(ads, C) + HCOO(ads, B) \rightarrow 2CO_2 + 3e^- + 2H^+ \tag{2.13}$$

However, Cuesta et al. observed the square root of current scaling linearly with the intensity of a single vibrational band [11, 15]. From this, they asserted that it was a single variety of formate reacting with itself. It is only evident that two different types of formate are reacting if [HCOOH] and [$HClO_4$] are varied (never before reported in $HClO_4$ solution). The results in this study are compatible with Cuesta et al.'s observations if fast interconversion of type B and type C formate is allowed (Eq. (2.14)). Rapid interconversion of two spectroscopically active species can give one vibrational band representing both species. Since this two formate oxidation process seems to be dominant, it is unsurprising that Cuesta and coworkers were able to ignore the type A formate pathway in their analysis.

$$HCOO^-(ads, C) \rightleftharpoons HCOO(ads, B) + e^- \tag{2.14}$$

For a summary of the multiple parrallel reaction pathways, see (Fig. **??**). This scheme incorporates all the equilibria and steps needed to describe the reactivity of HCOOH on Au seen in this work.

2.5 Conclusion

Formate adsorption was observed in three separate forms on Au(poly), showing reversible adsorption first suggested by Crepy et al. [5]. Adsorption was successfully fitted with the Sips isotherm. Formate oxidation kinetics proceed through two path-

ways, a simple first order oxidation of type A formate, and a more dominant second order pathway between type B and type C formate. This second order pathway is thought to be equivalent to the mechanism proposed by Cuesta and coworkers [11,15]. Perchlorate concentrations and pH influence the formate coverages under most investigated conditions. Type A formate competes with discharged perchlorate for surface sites, while type B and type C compete with fully charged perchlorate. Based on the charge state of the perchlorate and results reported by Conway et al. [17], it is suggested that type A formate adsorbs on faces with mostly Au(111) and Au(110) character, while type B and type C adsorb on facets with Au(100) character.

2.6 Supporting Information

2.6.1 Theory: Sips Isotherm

Like many similar isotherms, the Sips isotherm envisions a heterogeneous catalyst surface as being composed of many patches of sites. A "patch" of sites is separate from all other patches, and only adsorbates on the same patch can interact with one another. Sites on the same patch are considered identical, but most importantly share E^0_{ads} (adsorption energy) for a given substrate. Different patches will have different E^0_{ads} for the same substrate. Patches with E^0_{ads} all the way from $-\infty$ to ∞ are considered possible, but are all weighted according to a probability distribution in E^0_{ads}. What varies from one heterogeneous adsorption isotherm to another is the local adsorption isotherm (describing adsorption onto a single patch) and the form of the probability distribution for E^0_{ads} (see Eq. (2.15)). The Sips isotherm can be interpreted as treating local adsorption according to the Langmuir isotherm and using a nearly Gaussian probability distribution for E^0_{ads}. This is shown in Eq. (2.16). Note that the subscript "x" in (2.15) and (2.16) refers to a particular patch of sites. Unsubscripted θ refers to the global coverage.

$$\theta = \int \theta_x(E_x^0) \cdot P(E_x^0) dE_x^0 \tag{2.15}$$

$$\theta = \int \frac{\exp(\frac{F(E-E_x^0)}{RT})}{1+\exp(\frac{F(E-E_x^0)}{RT})} \tag{2.16}$$

$$\cdot \frac{\left(\frac{\sin(\pi C)}{\pi RT}\right)\exp\left(-\frac{CF(E_x^0-\overline{E^0})}{RT}\right)}{1+2\cos(\pi C)\exp\left(-\frac{CF(E_x^0-\overline{E_x^0})}{RT}\right)+\exp\left(-\frac{2CF(E_x^0-\overline{E^0})}{RT}\right)} dE_x^0 \tag{2.17}$$

$$= \frac{\exp(\frac{CF(E-\overline{E^0})}{RT})}{\left(1+\exp(\frac{CF(E-\overline{E^0})}{RT})\right)} \tag{2.18}$$

In order to model systems with two adsorbate species competing for the same sites, we must solve a system of two equations. Each of the two equations comes from replacing the single species form for $\theta_x(E_x^0)$ with a new one allowing for two adsorbates. An example of a pair of $\theta_x(E_x^0)$'s for a two adsorbate system are provided in Eq. (2.19) and Eq. (2.20). A third equation, Eq. (2.21), is needed to establish the relationship between the E_x^0's of the two adsorbates. Only molecules adsorbing on the same patches of sites may compete for said sites, implying that $P(E_x^0)$ (proportion of sites on the surface belonging to the patch of interest) must be the same for both adsorbates. Subscript "i" refers to the first species, and subscript "j" refers to the second.

$$\theta_{i,x}(E_{i,x}^0) = \frac{(1-\frac{\sigma_{i,x}}{\sigma_{j,x}}\theta_{j,x}(E_{j,x}^0))\cdot\exp(\frac{F(E-E_{i,x}^0)}{RT})}{1+\exp(\frac{F(E-E_{i,x}^0)}{RT})} \tag{2.19}$$

$$\theta_{j,x}(E_{j,x}^0) = \frac{(1-\theta_{i,x}(E_{i,x}^0))\cdot\exp(\frac{F(E-E_{j,x}^0)}{RT})}{1+\frac{\sigma_{i,x}}{\sigma_{j,x}}\exp(\frac{F(E-E_{j,x}^0)}{RT})} \tag{2.20}$$

$$P(E_{i,x}^0) = P(E_{j,x}^0) \tag{2.21}$$

Eqs. (2.19) - (2.21) apply when $\sigma_{i,x} \geq \sigma_{j,x}$. Note that $\frac{\sigma_{i,x}}{\sigma_{j,x}}$ is the ratio of saturation charges of the two adsorbates, equal to the ratio of number of sites blocked out by

Adsorbate	σ_i / μC cm^{-2}	$\overline{E_i^0}$ vs SHE / V	C_i
ClO_4	5.63	0.429	0.22
HCOO	18.5	0.374	0.259

Table 2.1: Parameters for Case i) Formate and Perchlorate Coadsorption Simulation

adsorption of i vs j.

Modelled Behaviour of Type A, B and C Formate

For all of the observed types of adsorbed formate, competition for adsorption sites with adsorbing perchlorate is evident. The adsorption characteristics of the formate and perchlorate in question, in particular the potential dependence of the adsorption equilibrium constant (charge transfer on adsorption or not) are very important in determining the coverage versus potential and concentration. Three cases will be considered: i) Potential dependent adsorption of perchlorate and formate onto the same sites. ii) Potential dependent formate adsorption and potential independent formate adsorption onto the same sites. iii) Potential independent formate and perchlorate adsorption onto the same sites. Using a dual adsorbate Sips isotherm (approximating the integral using the rectangle rule for $E^0_{F,x} = \overline{E^0_F} \pm$ 0.205 V, 100 rectangles), some current vs potential simulations were done with parameters from Table 2.1. As exact parameter values are often unavailable, these simulations only qualitatively resemble the data. Parameters for Case i) (Fig. 2.10) are taken from Sips fits of experimental peaks (formate parameters estimated from type A peak at highest [HCOOH]:[$HClO_4$]).

Case i), shows very distinctive behaviour in Fig. 2.10, and is similar to that for type A formate. At [HCOOH] = 0, a small peak from perchlorate adsorption is present. As [HCOOH] is increased, this small peak grows larger (charge linear with log[HCOOH]) and shifts to lower potential. When formate adsorption is dominant

Adsorbate	σ_i / μC cm^{-2}	$\overline{\Delta G}_{ads,i}$ / kJ mol^{-1}	C_i
ClO_4^-	5.63	41.4	0.22
HCOO	21.8	75.7	0.22

Table 2.2: Parameters for Case ii) Formate and Perchlorate Coadsorption Simulation

($\geq$ 0.05 m [HCOOH], for Fig. 2.10), peak potentials are also linear vs log[HCOOH] with slopes < -59.2 mV/decade (-75, in this case). This is the fingerprint of formate (possessing a higher saturation coverage) displacing perchlorate from surface sites. Note how only one peak is observed, but it is composed of both perchlorate and formate charge (Fig. 2.10, inset). Until the size of the peak reaches a maximum at high [HCOOH], some of the peak's charge will be from perchlorate. However this can be neglected for many solution compositions. For [HCOOH]:[$HClO_4$] $\geq$ 0.1 (condition for type A formate peak to be large enough for Sips isotherm fitting), the fraction of charge as perchlorate is estimated from modelling as being $\leq$ 35%.

Case ii) was simulated (Fig. 2.11) using the parameters contained in Table 2.2. Parameters for formate were taken from Sips isotherm fits of type B peaks. Parameters for perchlorate could not be measured, as no charge transfer occurs for perchlorate adsorption onto type B sites (not detected in voltammetry). Instead, parameters from perchlorate adsorption onto type A sites were used ($\overline{E^0_{ClO_4}} \cdot F$ used for $\overline{\Delta G}_{ads,ClO_4}$).

Case ii) is very distinct from Case i), and mirrors behaviour for type B formate. In this scenario, the observed current peak is purely derived from formate adsorption. It does not change in size vs [HCOOH] (or [$HClO_4$]). It merely shifts in potential in response to changes in [$HClO_4$] or [HCOOH] (-59.2 mV/log[HCOOH]). Peak shifts vs [$HClO_4$] cease once the [HCOOH]:[$HClO_4$] ratio is high enough.

Case iii) (Fig. 2.12) again is very distinct from the former two cases considered, and is a model for type C formate. Type C formate was hypothesized to adsorb on the same surfaces (but different sites) as type B formate, and react with it in a second-order fashion. This hypothesis was based on the behaviour of the rate constant for type B formate adsorption. The model for Case iii) disallows charge transfer on

Adsorbate	$\Gamma_{i,\max}$ / pmol cm^{-2}	$\overline{\Delta G}_{\mathrm{ads},i}$ / kJ mol^{-1}	C_i
ClO_4^-	58.4	41.4	0.22
$HCOO^-$	226	4.82	0.22

Table 2.3: Parameters for Case iii) Formate and Perchlorate Coadsorption Simulation

formate or ClO_4^- adsorption, so coverage will only change as a function of $[HClO_4]$ and [HCOOH]. Formate coverage vs log[HCOOH] is notably linear when far from zero or full coverage, with higher $[HClO_4]$ simply causing the line to shift to lower coverages. Note the similarity in behaviour for kB and j_{ox} vs log[HCOOH] at 1.2 V (see main paper). Parameters for this model were mostly taken from experimental data: perchlorate parameters the same as for Case ii), formate parameters same as Case ii), but $\overline{\Delta G}_{\mathrm{ads,HCOO^-}}$ was lowered to get the desired behaviour. See Table 2.3.

Second Order Reactions in the Sips Isotherm

Using coverage-potential information from fitted fast sweep CVs, fitting of several rate laws to j_{ox} data was attempted. The patch-based nature of the Sips isotherm complicates higher order surface reactions, e.g., second order reaction between two adsorbates, as only adsorbates on the same patch can come into contact and react with each other. In order to assess the probability of two adjacent adsorbates (of type x and y) over all patches, an integral similar to Eq. (2.15) must be solved (Eq. (2.23)). Note that the form of the integral applies for either two of the same species of adsorbate (x=y) or two different types of adsorbate on different types of sites that are randomly arranged on the surface (not two distinct species in competition for the

same sites).

$$P_{ij}(E) = \int P_i \cdot \theta_{i,x}(E^0_{i,x}) \cdot P_j \cdot \theta_{j,x}(E^0_{j,x}) \cdot P(E^0_{i,x}) dE^0_{i,x} \tag{2.22}$$

$$P_{ij}(E) = P_i \cdot P_j \cdot \int \frac{\exp(\frac{F(E-E^0_{i,x})}{RT})}{1+\exp(\frac{F(E-E^0_{i,x})}{RT})} \cdot \frac{\exp(\frac{F(E-E^0_{j,x})}{RT})}{1+\exp(\frac{F(E-E^0_{j,x})}{RT})} \tag{2.23}$$

$$\cdot \frac{\left(\frac{\sin(\pi C_i)}{\pi RT}\right) \exp\left(-\frac{C_i F(E^0_{i,x}-\overline{E^0_i})}{RT}\right)}{1+2\cos(\pi C_i)\exp\left(-\frac{C_i F(E^0_{i,x}-\overline{E^0_x})}{RT}\right)+\exp\left(-\frac{2C_i F(E^0_{i,x}-\overline{E^0_i})}{RT}\right)} dE^0_{i,x} \tag{2.24}$$

P_i and P_j are the probability of a randomly selected site on a patch being a possible site for adsorbate type i and type j, respectively. These are assumed as being constant across all patches, and left out of the integrals (incorporated into rate constant k_{ij} while fitting $P_{ij}(E)$ to j_{ox} data). Species "i" assigned so that $C_i \leq C_j$ (i has wider probability distribution for $E^0_{i,x}$). Note that $P(E^0_{i,x}) = P(E^0_{j,x})$, as both weightings apply to the same patch of sites. In fact, it is this relationship that allows determination of $E^0_{j,x}$ from $E^0_{i,x}$.

Unfortunately, Eq. (2.23) cannot be evaluated analytically. Instead, integrals of this sort were approximated using the rectangle rule, dividing the function between ± 0.5 V of $E^0_{i,x}$ into 125 segments (or ± 1 V of $E^0_{i,x}$ into 200 segments). Note that many assumptions must be made in order to assess reactivity of adsorbates for a reaction order of two, which may render this analysis invalid. Also worth noting is that simply multiplying the overall coverages (taking $P_{ij}(E) = \theta_i \cdot \theta_j$ as one would do in the Langmuir case) gives very similar (but not identical) results to approximating the integral from Eq. (2.23). Fitting j_{ox} vs potential to $\theta_i \cdot \theta_j$ yields similar results as fitting it to an approximate form of the integral from Eq. (2.23).

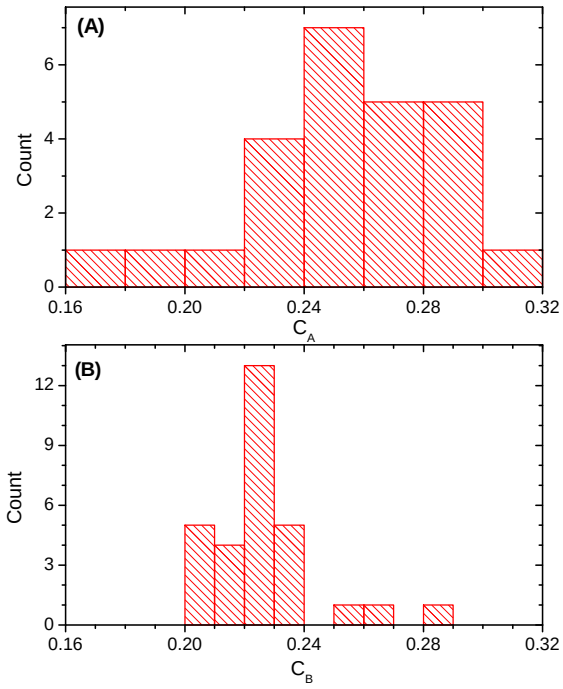

Figure 2.13: Histograms of C_x values for (A) x = type A formate and (B) x = type B formate.

2.6.2 Additional Information

Formate Sips Isotherm Parameters

Fitting of formate current peaks from fast sweep voltammograms yielded three parameters that were scattered about a central value as opposed to changing systematically with solution composition. These included the width parameters C_A and C_B, as well as the peak charge for type B formate ($\sigma_{B,\max}$). Histograms or graphs of these values are included in Fig. 2.13 and Fig. 2.14.

Similar to the width factors, the value of $\sigma_{\mathrm{B,max}}$ seems independent of the solution composition for all but one data set (0.01 m $HClO_4$). The change of $\sigma_{B,\max}$ versus

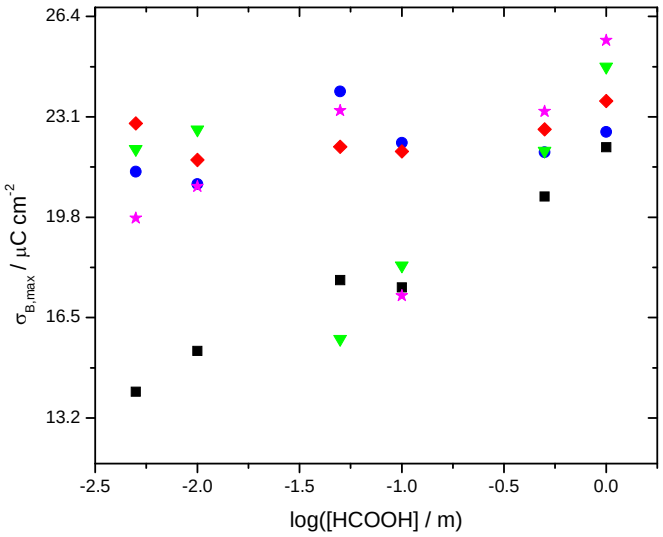

Figure 2.14: All values of $\sigma_{\mathrm{B,max}}$ extracted from Sips isotherm fits. [$HClO_4$] = 0.01 (■, black), 0.05 (●, blue), 0.1 (♦, red), 0.5 (▼, green), or 1 m (★, magenta).

[HCOOH] for 0.01 m $HClO_4$ is likely a fitting artefact. Early onset of Au oxide prevents capacitance baseline subtraction of formate peaks above ca. 950 mV RHE in this data set, cutting off the majority of the type B peak. This means fitted curves had poor sampling of the type B peak at low concentrations. With higher [HCOOH], the peak moves over into the fitting window and the peak charge approaches to the usual value. With this in mind, the average value of $\sigma_{B,\mathrm{max}}$ was calculated without its four lowest values for 0.01 m $HClO_4$. The average $\sigma_{B,\mathrm{max}}$ is 21.8 ± 2.2 μC/cm^2.

The remaining three parameters from the Sips isotherm fits were found to shift linearly against log[HCOOH]. The parameters for these linear fits can be found in Table 2.4.

–	E_{Peak} Type A Formate vs log[HCOOH]	
$[HClO_4]$ / m	Slope / mV RHE	Intercept / mV RHE
0.01	-80.6	379.6
0.05	-81.6	378.3
0.1	-80.5	391.6
0.5	-115.3	388.9
1	-137.8	392.2
–	E_{Peak} Type B Formate vs log[HCOOH]:	
$[HClO_4]$ / m	Slope / mV RHE	Intercept / mV RHE
0.01	-56.9	782.2
0.05	-66.3	776.8
0.1	-72.3	786.4
0.5	-70.8	807.2
1	-72.0	826.9
–	$\sigma_{A,\max}$ vs log[HCOOH]:	
$[HClO_4]$ / m	Slope / μC cm^{-2}	Intercept / μC cm^{-2}
0.01	3.52	18.2
0.05	3.59	17.3
0.1	2.79	15.2

Table 2.4: Parameters from Linear Fits in Perchloric and Formic Acid Data

Formate Sips Isotherm Peak Fits

In the interest of brevity, only some formate peak fits were shown in the main body of this work. All peak fits (for all 30 solution compositions) are here, overlaid with their respective data sets in Figures 2.15 to 2.19. Also included are the χ^2 values for all fits, summarized in Table 2.5.

Oxidation Current: First Order Rate Law Fits

Not all fits of Sips isotherms to j_{ox} vs potential data were shown in the main paper. All fits and experimental data are shown here in Figures 2.20 to 2.24. Values of χ^2 are tabulated in Table 2.6.

As discussed in Sec. 2.6.1, the type A formate peak is composed of both perchlorate and formate adsorption charge ($\lesssim$ 35% perchlorate). Unfortunately, perchlorate

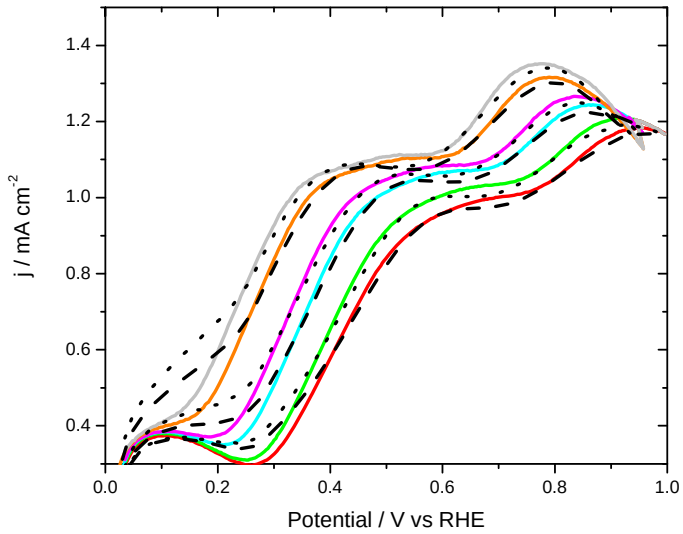

Figure 2.15: Measured capacitance + adsorption pseudocapacitance currents at 15 V/s in 0.01 m $HClO_4$. [HCOOH] = 0.005 (red), 0.01 (green), 0.05 (cyan), 0.1 (magenta), 0.5 (orange), and 1 m (grey). Dotted and dashed lines represent Sips isotherm fits of formate adsorption current density + capacitance current density.

[HCOOH] / m	$[HClO_4]$ = 0.01 m	$[HClO_4]$ = 0.05 m	$[HClO_4]$ = 0.1 m
0.005	$4.354{\cdot}10^{-3}$	$1.012{\cdot}10^{-3}$	$2.857{\cdot}10^{-4}$
0.01	$4.210{\cdot}10^{-3}$	$7.545{\cdot}10^{-4}$	$2.854{\cdot}10^{-4}$
0.05	$2.104{\cdot}10^{-3}$	$5.450{\cdot}10^{-4}$	$2.374{\cdot}10^{-4}$
0.1	$2.062{\cdot}10^{-3}$	$1.866{\cdot}10^{-4}$	$1.972{\cdot}10^{-4}$
0.5	$3.065{\cdot}10^{-3}$	$4.686{\cdot}10^{-5}$	$1.942{\cdot}10^{-4}$
1	$3.918{\cdot}10^{-3}$	$4.338{\cdot}10^{-5}$	$2.680{\cdot}10^{-4}$
[HCOOH] / m	$[HClO_4]$ = 0.5 m	$[HClO_4]$ = 1 m	–
0.005	$6.667{\cdot}10^{-4}$*	$7.295{\cdot}10^{-3}$*	–
0.01	$1.914{\cdot}10^{-4}$*	$7.255{\cdot}10^{-3}$*	–
0.05	$8.190{\cdot}10^{-5}$	$2.165{\cdot}10^{-3}$*	–
0.1	$8.736{\cdot}10^{-5}$	$2.315{\cdot}10^{-4}$	–
0.5	$9.755{\cdot}10^{-5}$	$3.984{\cdot}10^{-4}$	–
1	$1.740{\cdot}10^{-5}$	$5.440{\cdot}10^{-4}$	–
* indicates single peak Sips isotherm fit.			

Table 2.5: Chi Squared Values: Sips Isotherm Fits of Formate Adsorption Peaks

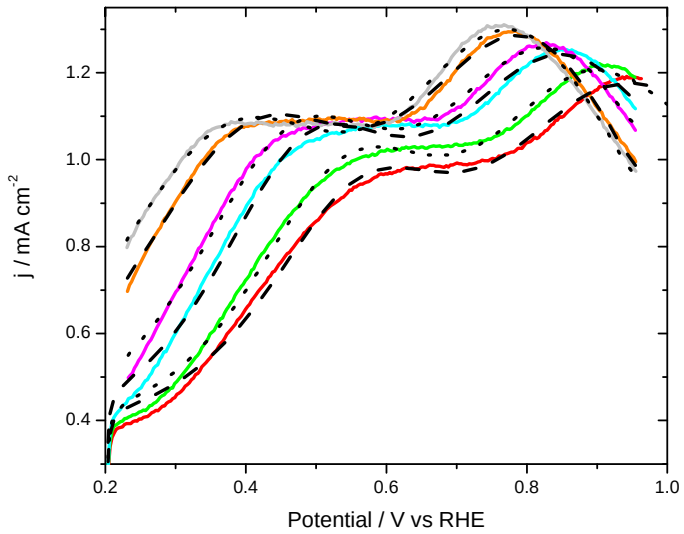

Figure 2.16: Measured capacitance + adsorption pseudocapacitance currents at 15 V/s in 0.05 m $HClO_4$. [HCOOH] = 0.005 (red), 0.01 (green), 0.05 (cyan), 0.1 (magenta), 0.5 (orange), and 1 m (grey). Dotted and dashed lines represent Sips isotherm fits of formate adsorption current density + capacitance current density.

[HCOOH] / m	$[HClO_4]$ = 0.01 m	$[HClO_4]$ = 0.05 m	$[HClO_4]$ = 0.1 m
0.005	$5.387{\cdot}10^{-4}$	$9.343{\cdot}10^{-4}$	$1.060{\cdot}10^{-4}$
0.01	$1.490{\cdot}10^{-3}$	$1.951{\cdot}10^{-4}$	$1.114{\cdot}10^{-4}$
0.05	$1.630{\cdot}10^{-4}$	$2.917{\cdot}10^{-4}$	$1.560{\cdot}10^{-4}$
0.1	$2.041{\cdot}10^{-4}$	$2.934{\cdot}10^{-4}$	$1.980{\cdot}10^{-4}$
0.5	$1.642{\cdot}10^{-4}$	$3.136{\cdot}10^{-4}$	$3.050{\cdot}10^{-4}$
1	$1.442{\cdot}10^{-4}$	$2.667{\cdot}10^{-4}$	$2.993{\cdot}10^{-4}$
[HCOOH] / m	$[HClO_4]$ = 0.5 m	$[HClO_4]$ = 1 m	–
0.005	$1.688{\cdot}10^{-4}$	$9.102{\cdot}10^{-5}$	–
0.01	$9.205{\cdot}10^{-5}$	$8.569{\cdot}10^{-5}$	–
0.05	$1.080{\cdot}10^{-4}$	$8.323{\cdot}10^{-5}$	–
0.1	$1.068{\cdot}10^{-4}$	$1.035{\cdot}10^{-4}$	–
0.5	$1.858{\cdot}10^{-4}$	$1.494{\cdot}10^{-4}$	–
1	$1.650{\cdot}10^{-4}$	$1.881{\cdot}10^{-4}$	–

Table 2.6: Chi Squared Values: First Order Fits of Current Density vs Potential to Sips Isotherm Coverages

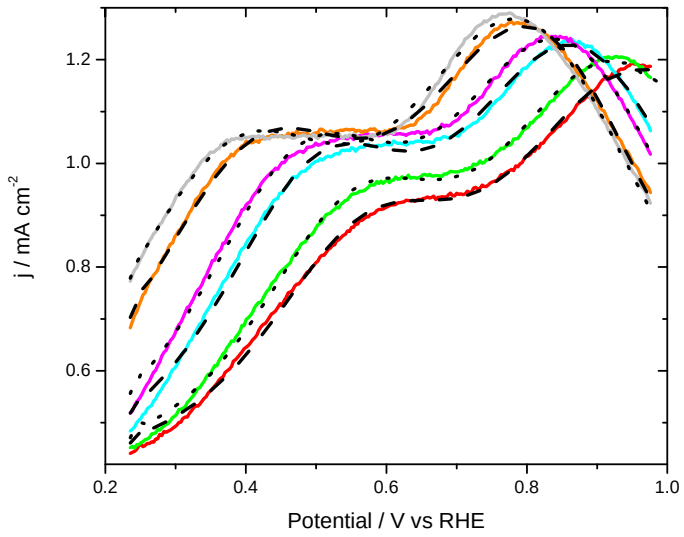

Figure 2.17: Measured capacitance + adsorption pseudocapacitance currents at 15 V/s in 0.1 m $HClO_4$. [HCOOH] = 0.005 (red), 0.01 (green), 0.05 (cyan), 0.1 (magenta), 0.5 (orange), and 1 m (grey). Dotted and dashed lines represent Sips isotherm fits of formate adsorption current density + capacitance current density.

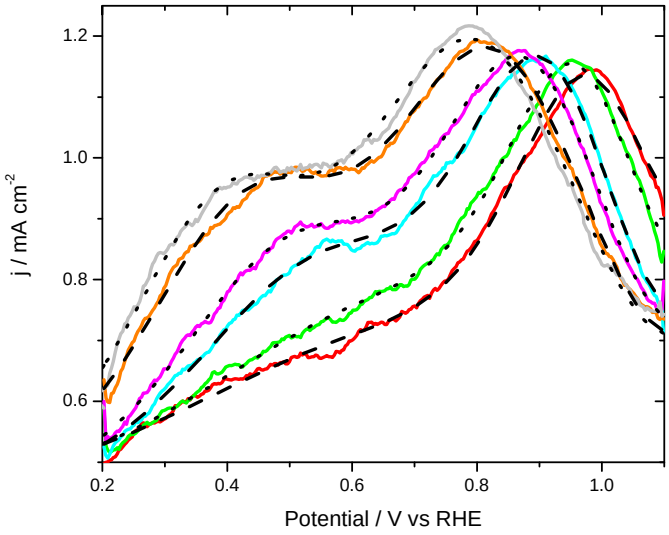

Figure 2.18: Measured capacitance + adsorption pseudocapacitance currents at 15 V/s in 0.5 m $HClO_4$. [HCOOH] = 0.005 (red), 0.01 (green), 0.05 (cyan), 0.1 (magenta), 0.5 (orange), and 1 m (grey). Dotted and dashed lines represent Sips isotherm fits of formate adsorption current density + capacitance current density.

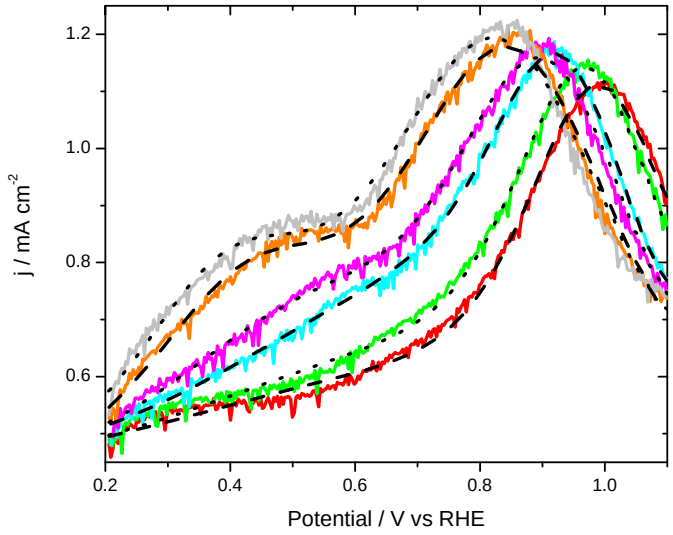

Figure 2.19: Measured capacitance + adsorption pseudocapacitance currents at 15 V/s in 1 m $HClO_4$. [HCOOH] = 0.005 (red), 0.01 (green), 0.05 (cyan), 0.1 (magenta), 0.5 (orange), and 1 m (grey). Dotted and dashed lines represent Sips isotherm fits of formate adsorption current density + capacitance current density.

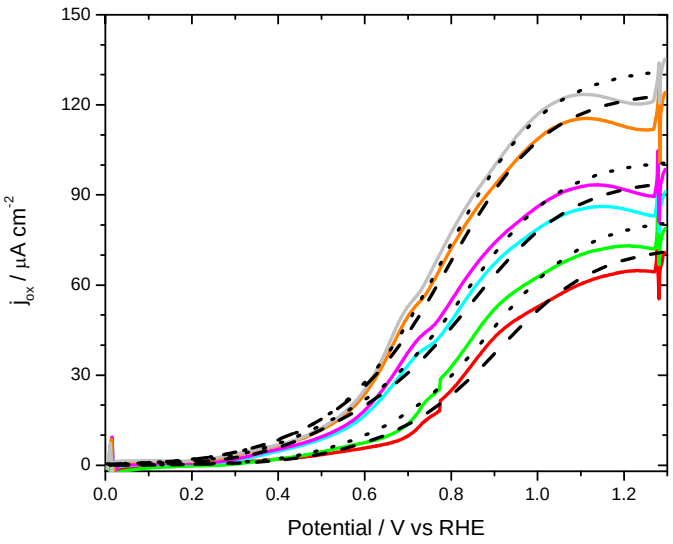

Figure 2.20: Potential dependence of j_{ox} in 0.01 m $HClO_4$ at [HCOOH] = 0.005 (red), 0.01 (green), 0.05 (cyan), 0.1 (magenta), 0.5 (orange) and 1 m (grey). Dashed and dotted black lines correspond to fits of $j_{\mathrm{ox}} = kA \cdot \theta_{\mathrm{A}} + kB \cdot \theta_{\mathrm{B}}$ with the coverages found by fitting Sips Isotherms.

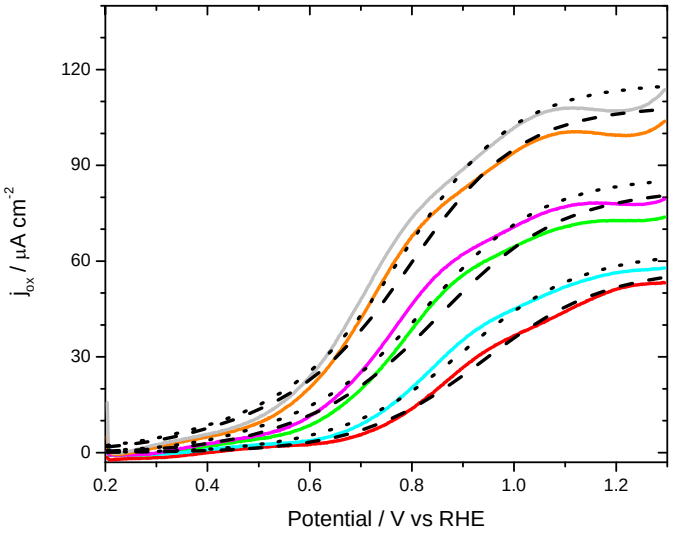

Figure 2.21: Potential dependence of j_{ox} in 0.05 m $HClO_4$ at [HCOOH] = 0.005 (red), 0.01 (green), 0.05 (cyan), 0.1 (magenta), 0.5 (orange) and 1 m (grey). Dashed and dotted black lines correspond to fits of $j_{\mathrm{ox}} = kA \cdot \theta_{\mathrm{A}} + kB \cdot \theta_{\mathrm{B}}$ with the coverages found by fitting Sips Isotherms.

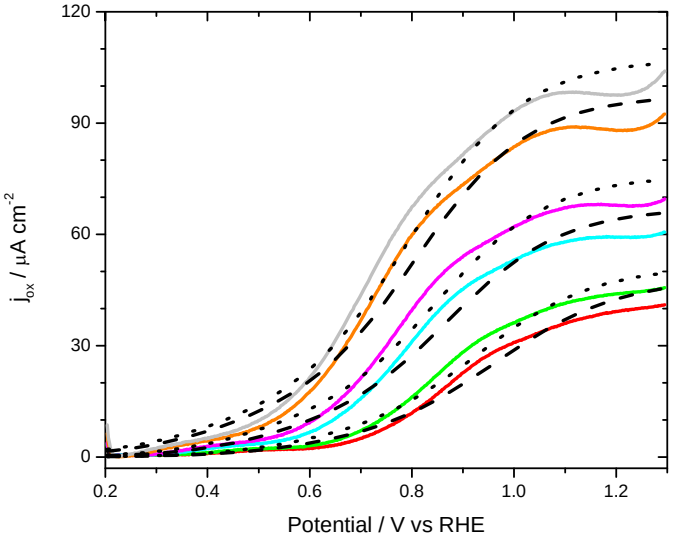

Figure 2.22: Potential dependence of j_{ox} in 0.1 m $HClO_4$ at [HCOOH] = 0.005 (red), 0.01 (green), 0.05 (cyan), 0.1 (magenta), 0.5 (orange) and 1 m (grey). Dashed and dotted black lines correspond to fits of $j_{\mathrm{ox}} = kA \cdot \theta_{\mathrm{A}} + kB \cdot \theta_{\mathrm{B}}$ with the coverages found by fitting Sips Isotherms.

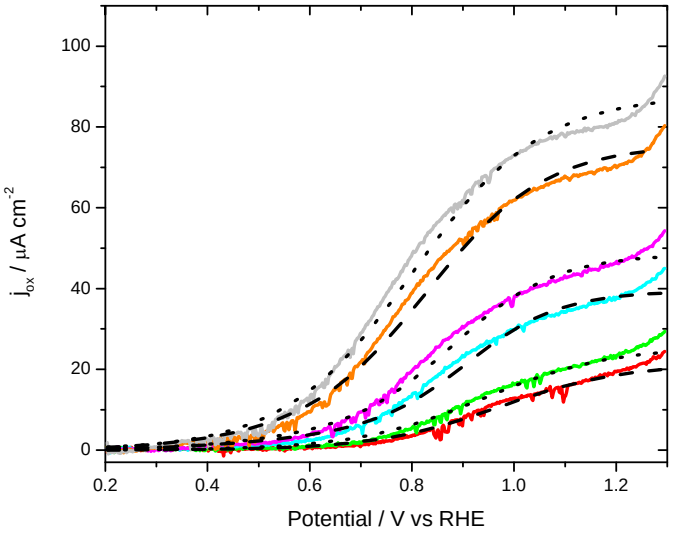

Figure 2.23: Potential dependence of j_{ox} in 0.5 m $HClO_4$ at [HCOOH] = 0.005 (red), 0.01 (green), 0.05 (cyan), 0.1 (magenta), 0.5 (orange) and 1 m (grey). Dashed and dotted black lines correspond to fits of $j_{\mathrm{ox}} = kA \cdot \theta_{\mathrm{A}} + kB \cdot \theta_{\mathrm{B}}$ with the coverages found by fitting Sips Isotherms.

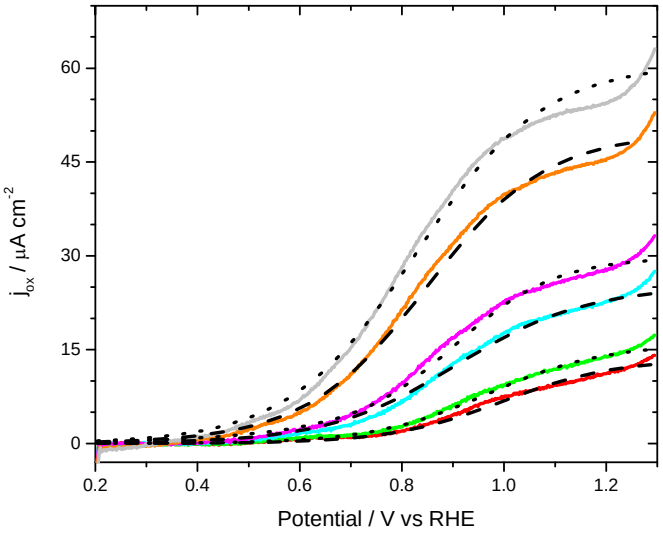

Figure 2.24: Potential dependence of j_{ox} in 1 m $HClO_4$ at [HCOOH] = 0.005 (red), 0.01 (green), 0.05 (cyan), 0.1 (magenta), 0.5 (orange) and 1 m (grey). Dashed and dotted black lines correspond to fits of $j_{\mathrm{ox}} = kA \cdot \theta_{\mathrm{A}} + kB \cdot \theta_{\mathrm{B}}$ with the coverages found by fitting Sips Isotherms.

[HCOOH] / m:	$[HClO_4]$ = 0.01 m:	$[HClO_4]$ = 0.05 m:	$[HClO_4]$ = 0.1 m:
0.005	0.603	$1.68{\cdot}10^{-9}$	0.309
0.01	0.658	0.228	0.406
0.05	1.19	0.342	0.590
0.1	1.10	0.528	0.672
0.5	0.606	0.635	0.718
1	0.392	0.555	0.662
[HCOOH] / m:	$[HClO_4]$ = 0.5 m:	$[HClO_4]$ = 1 m:	–
0.005	–	–	–
0.01	–	–	–
0.05	0.333	–	–
0.1	0.284	0.209	–
0.5	0.232	0.0524	–
1	$4.22{\cdot}10^{-3}$	$9.70{\cdot}10^{-11}$	–

Table 2.7: Values of Rate Constant, kA, for First Order Oxidation of Type A Formate

charge cannot be corrected for in the experimental system. This leads to inaccurate assessment of the charge for type A formate, as we can only extract the sum of perchlorate and formate charge on type A sites. Since the charge for type A peak was used in fitting rate laws to the oxidation current-potential traces, the oxidation rate constant for type A formate will be inaccurate at low [HCOOH]:[$HClO_4$]. Over all data sets, kA averages at $(5 \pm 3){\cdot}10^{-1}$ s^{-1}. When restricted to [HCOOH]:[$HClO_4$] $\geq$ 1, kA averages $(5 \pm 2){\cdot}10^{-1}$ s^{-1} (upon rejection of statistical outliers). There is no systematic shift in kA, although precision improves. It appears as if the small contribution that type A formate makes towards oxidation activity means that experimental scatter in kA is greater than the systematic error from coadsorbed perchlorate. All extracted values of kA have been included in Table 2.7.

Chapter 3

Formic Acid Oxidation on Au in H_2SO_4 Solutions

3.1 Introduction

Detailed results on formic acid oxidation on Au(poly) in $HClO_4$ solutions were recently presented [34][1], with focus on the adsorption of formate and its subsequent oxidation. Supporting electrolyte concentration heavily influenced catalytic activity, because of competitive perchlorate adsorption. An even greater dependence of activity on supporting electrolyte composition is seen in sulfuric acid solutions, given the greater affinity of sulfate for Au. This study focuses on measuring and rationalizing catalytic activity vs supporting electrolyte composition, mainly via tracking formate and sulfate adsorption onto Au.

The activity of Au for the oxidation of formic acid (HCOOH) has been studied in UHV conditions [2, 3], as well as in sulfuric [4–11] and perchloric acid [11–15, 34] solutions. This reaction mechanism has been characterized as sequential adsorption and oxidation of a formate intermediate, and has been observed with techniques

[1] Chapter 2 of this thesis.

such as voltammetry [5, 12–14, 34], SERAS [13, 14], SEIRAS [11, 15], EQCM [8] and potential step methods [10]. Au is a poor catalyst, having shown a maximum j_{ox} of 120 $\mu A/cm^2$ in a previous study [34], but possesses other advantages. The more active catalysts, e.g. Pt and Pd, suffer from accumulation of CO as a catalytic poison on their surfaces. While their maximum activity exceeds that of Au, CO poisoning complicates mechanistic studies. Treatment of formic acid oxidation becomes even more complicated when adsorption of supporting electrolyte anions is factored in, as these act as yet another catalytic poison. Conveniently, oxidation of HCOOH on Au is a CO-free process, leaving only supporting electrolyte anions to be accounted for. This was done in $HClO_4$ solutions [34], and a dual pathway mechanism was derived (Eq. (3.1)-(3.4)). The dominant pathway, Eq. (3.3), is similar to that proposed by Cuesta et al [11, 15], who extrapolated their mechanism to Pt. Both oxidation pathways have chemical rate limiting steps, which have potential independent rate constants.

$$\mathrm{HCOOH} \rightleftharpoons \mathrm{HCOO(ads)} + \mathrm{H^+} + \mathrm{e^-} \tag{3.1}$$

$$\mathrm{HCOOH} \rightleftharpoons \mathrm{HCOO^-(ads)} + \mathrm{H^+} \tag{3.2}$$

$$\mathrm{HCOO^-(ads)} + \mathrm{HCOO(ads)} \longrightarrow 2\mathrm{CO_2} + 2\mathrm{H^+} + 3\mathrm{e^-} \tag{3.3}$$

$$\mathrm{HCOO(ads)} \longrightarrow \mathrm{CO_2} + \mathrm{H^+} + \mathrm{e^-} \tag{3.4}$$

An increased tendency for sulfate adsorption has been offered as an explanation why current densities are decreased in H_2SO_4 solutions as compared to $HClO_4$ solutions [11]. Many researchers have focused their efforts on the study of sulfate adsorption onto Au electrodes, including Au(111) [20, 35–40], Au(100) [39, 41], Au(110) [39] and Au(poly) [20]. In general, a sulfate derivative (sulfate or bisulfate, assignment varies) is found to adsorb strongly onto Au(*hkl*) electrodes and often shows an order-disorder transition to a 2D solid-like adlayer at high coverages. This ordered structure

contains water acting as hydrogen-bond bridges between adsorbates [40], creating a more stable adlayer. Such an adlayer appears to be resilient enough to largely suppress formate adsorption.

An electrochemical and SEIRAS study comparing H_2SO_4 and $HClO_4$ solutions by Cuesta and coworkers [15] revealed lowered activity and formate vibrational intensity in the presence of H_2SO_4, which possesses the more strongly adsorbing anion. Also, EQCM studies [8] showed that mass of adsorbates on Au decreased from H_2SO_4 to H_2SO_4 + HCOOH solutions. Given the lighter mass of formate, displacement of SO_4^{2-} from Au is implied. Formate and SO_4^{2-} are clearly in competition for the same adsorption sites on Au surfaces. In order to understand HCOOH oxidation activity, SO_4^{2-} and formate adsorption must be studied in parallel. This has not been done in great detail in previous studies, to the best of our knowledge. Solutions from 0.05 - 1 molal (m) [H_2SO_4] and 0.005 - 1 m [HCOOH] were studied by collecting cyclic voltammograms (CVs) for sweep rates from 0.2 - 100 V/s. The results are discussed with heavy reference to the preceding study in $HClO_4$ solutions [34].

3.2 Experimental

All solutions used Milli-Q water with a resistivity of >18 MΩ cm. The Au(poly) working electrode was made from Au wire (Alfa Aesar, Premion, 99.999%) sealed to a third of its length in teflon tape. This was immersed in fresh, hot piranha solution overnight and was then rinsed and soaked thoroughly in Milli-Q water before use. All experiments made use of a reversible hydrogen reference electrode (RHE) separated from the working compartment by a Luer cap wetted with electrolyte. The Pt reference electrode was cleaned in fresh piranha solution overnight and rinsed thoroughly before use. A Pt wire counter electrode (Alfa Aesar, Premion, 99.997%) was used, and was flame annealed before experiments. Ultra-pure H_2SO_4 supplied by Seastar Chemicals ("Baseline" grade, 98%) and $Na_2SO_4{\cdot}10H_2O$ supplied by Sigma-Aldrich

(puriss, $\geq$ 99%) were used in the preparation of supporting electrolyte solutions. Solutions were purged using 99.999% Ar (Praxair), and purging of the reference electrode compartment was done with 99.995% H_2 (Praxair). HCOOH was supplied by Fluka Analytical (puriss for HPLC, 50% HCOOH). The electrochemical cell used was glass, and all components in contact with the experimental solutions were glass or teflon. Cell components were heated in concentrated H_2SO_4 overnight and then rinsed thoroughly with Milli-Q water before experiments. This was also done for volumetric glassware used in preparing solutions. The RHE and working electrode compartment were filled with identical solutions (common $[H_2SO_4]$) at the beginning of experiments. Constant ionic strength was not maintained accross different $[H_2SO_4]$, due to the lack of suitable, non-adsorbing anion candidates. Candidates such as PF_6^- and BF_4^- were considered, but available purities were too low. Experiments at different [HCOOH]'s at a common $[H_2SO_4]$ were undertaken by sucessive spiking of HCOOH aliquots. Aliquots were added into an electrolyte of known % mass H_2O, HCOOH, and supporting electrolyte between experiments (into working electrode compartment only). Electrolytes were mixed by vigorous Ar bubbling for 3 min following additions. Electrochemical annealing was applied to the working electrode before and between all separate experiments, formic acid additions, etc. This entailed running 25-100 CVs from 0.2 to 1.85 V RHE at 200 mV/s. This was found to stabilize currents reliably. The surface area of the Au working electrode was determined using the Burshtein method [30] in 0.5 M H_2SO_4. The area was 0.45 cm^2, with a roughness factor of 2.3. Potential control and current measurement were handled by Gamry Reference 600 potentiostat/galvanostat.

Whenever pH is used, this was calculated as $pH = -\log[H^+]$ (neglecting the single ion activity coefficient of H^+). Trends versus pH are generally assessed at constant concentration of supporting electrolyte, e.g. varied ratio of H_2SO_4 to Na_2SO_4 at total 0.5 M, which helps to minimize change in ionic activity coefficients as a function of pH. Concentrations used in calculating pH's were generated using average

ionic activity coefficients for H_2SO_4 / Na_2SO_4 solutions from Wirth's work [42]. All reported concentrations are in molal, abreviated "m" (or millimolal as "mm"), unless otherwise specified.

Fast sweep CVs ($\geq$15 V/s) were collected to emphasize capacitance and adsorption pseudocapacitance currents. This allows easier observation of formate adsorption peaks. Potential excursions were restricted from 0.2 to 1.35 V RHE. This excludes zones where appreciable hydrogen evolution or reconstruction due to Au oxidation takes place**.** Fast sweep CVs were corrected for IR drop post-collection, with the cell set up to minimize resistance. Cell resistances fell in the range of 0.5-10 Ω. For currents measured at 15 V/s, IR corrections fell in the range of 0 - 5 mV. Only data from the anodic sweeps of CVs were analyzed in detail.

3.3 Results

Current densities from electrochemically reversible adsorption are expected to be linear with sweep rate (ν), and to appear as peaks. Capacitance currents scale identically with sweep rate, and so are experimentally inseparable from adsorption current. In the reversible limit, the sum of capacitance and adsorption currents become much greater than the sweep rate independent oxidation currents (see Sec. 3.3.3) at larger ν. In $HClO_4$ solutions, formate adsorbs reversibly onto Au [34], so this is anticipated in H_2SO_4 solutions. Formate and sulfate adsorption onto Au in H_2SO_4 solution was observed by setting ν for CVs to 15 V/s or greater (often referred to as "fast sweep" CVs). This has been exploited on Pt to allow observation of formate adsorption onto these surfaces [31]. The measured capacitance + adsorption current can be scaled down to its value at a lower ν to show oxidation current density (j_{ox}) and adsorption / capacitance current separately (Fig. 3.1).

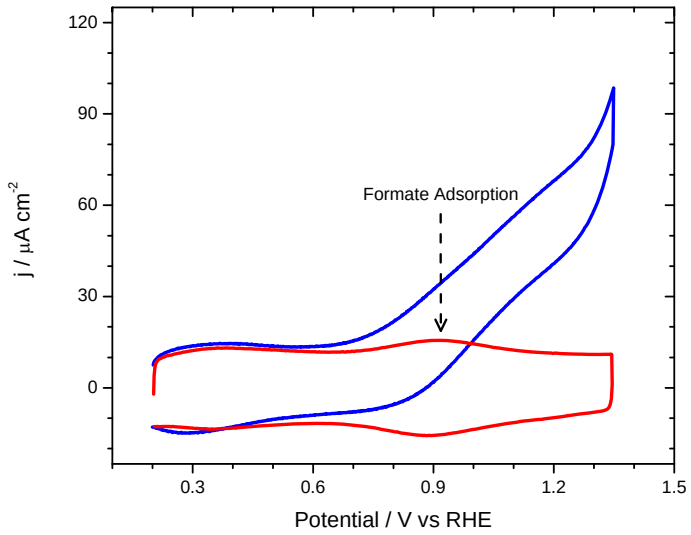

Figure 3.1: Current densities measured in 0.1 m H_2SO_4 / 0.1 m HCOOH. j_{tot} (blue) $j_{\text{Cap.+Pseudocap.}}$ (red) apply at 0.2 V/s. $j_{\text{Cap.+Pseudocap.}}$ measured at 15 V/s, divided by 75.

3.3.1 Sulfate Adsorption in H_2SO_4 Solution

CVs over a range of H_2SO_4 concentrations (0.01 - 1 m) and ν (0.2 - 100 V/s) reveal current density peaks associated with sulfate adsorption, which cover most of the double layer region $>$ 0.2 V RHE. A large, lower potential peak and a small, high potential shoulder are seen in all cases, e.g., Fig. 3.2 (A). The dual peak shape is reminiscent of results in a preceding study in $HClO_4$ solutions [34], where the same electrodes and electrode treatments were used. Several distinct types of formate and perchlorate adsorption were observed in the previous study, and now sulfate adsorption seems to behave similarly.

The position of these peaks displays both H_2SO_4 and pH dependence. Peak potential drops at -61.1 mV/log[H_2SO_4] vs RHE or ca. 0 mV/log[H_2SO_4] vs SHE. There is more exotic behaviour against pH at $[SO_4^{2-}] = 0.5$ M, displayed in Fig. 3.2 (B).

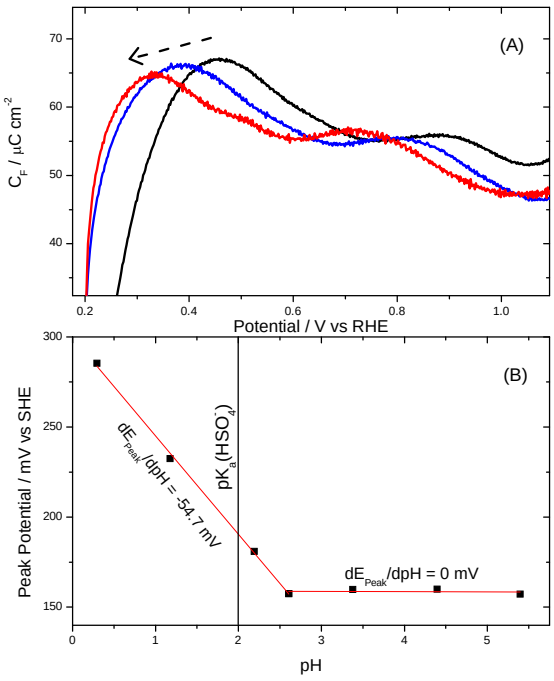

Figure 3.2: (A) Sulfate adsorption peaks for $[H_2SO_4] = 0.01$, 0.1 and 1 m. Arrow indicates increasing concentration. (B) Low-potential peak position as a function of pH. $[H_2SO_4] + [Na_2SO_4] = 0.5$ M. Parameters for linear trends are included in Supporting Information.

Here, peak potential is independent of pH when pH > pK_a(HSO_4^-) =1.99 and shifts at -55 mV/pH near or below pK_a(HSO_4^-). Peak potentials do not exhibit shifts vs sweep rate for ν = 0.2 - 100 V/s.

3.3.2 Formate Adsorption in H_2SO_4 Solution

Similar to sulfate adsorption, formate adsorption pseudocapacitance peaks were observed upon addition of HCOOH. For sweep rates $\leq$ 100 V/s, CVs are superimposable after IR correction and normalization by sweep rate. As expected, adsorption of formate is heavily suppressed with rising [H_2SO_4]:[HCOOH], which shrinks adsorption peaks and moves them to higher potentials. At low [HCOOH], it is typical to see no peak whatsoever, only a flat shoulder above the sulfate peaks. When [HCOOH] is raised further, an adsorption peak seems to grow on top of this shoulder. This is shown in Fig. 3.3. The maximum charge observed under the main formate peak was 16 μC/cm^2, calculated from the charge difference between 0.005 and 1 m HCOOH at 0.05 m H_2SO_4. Charge associated with the higher potential shoulder was 4.2 μC/cm^2, calculated as the charge difference between 0.005 m HCOOH and the blank at 0.05 H_2SO_4. The total charge is on the order of charges measured in $HClO_4$ solutions [34].

Formate peaks are wide, much more so than the 91 mV full width half maximum (FWHM) predicted by the Langmuir model. This is similar to results in $HClO_4$ solutions [34], where electrode heterogeneity accounted for peak widths. Accurate peak widths are difficult to assess without some form of peak deconvolution.

Trends of formate peak potential versus log[HCOOH] are presented in Fig. 3.4. The decrease in formate peak potential is linear in log[HCOOH], with slopes < -59.2 mV (-121 to -233 mV/log[HCOOH]).

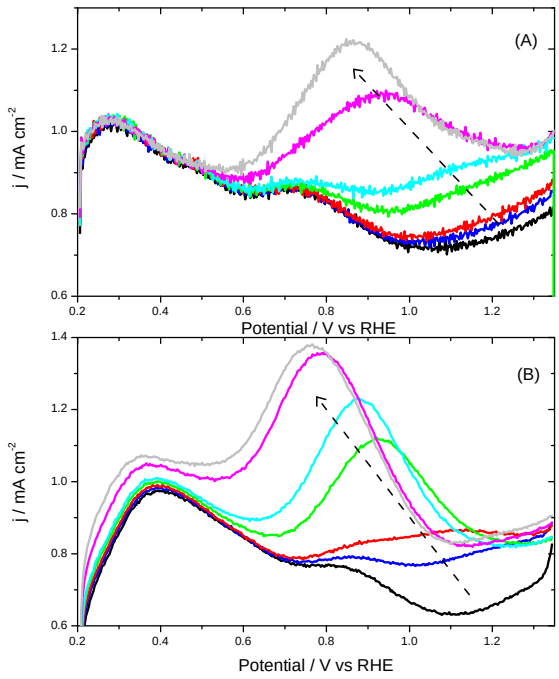

Figure 3.3: 15 V/s anodic sweeps in (A) 1 or (B) 0.05 m H_2SO_4. [HCOOH] = 0, 0.005, 0.01, 0.05, 0.1, 0.5 or 1 m. Arrow indicates increasing concentration.

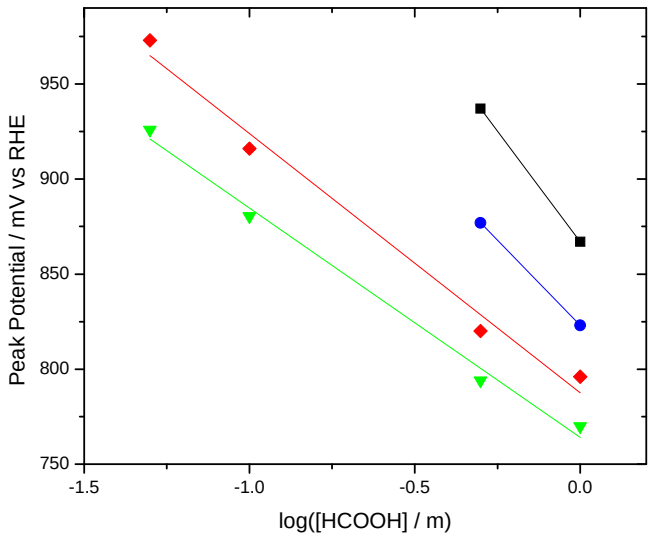

Figure 3.4: Formate adsorption peak potentials as a function of log[HCOOH]. [H_2SO_4] = 0.05 (▼, green), 0.1 (♦, red), 0.5 (●, blue) or 1 m (■, black). Parameters for linear trends are included in Supporting Information.

3.3.3 Formate Oxidation in H_2SO_4 Solutions

Oxidation Current Densities versus Potential

CVs collected at $\nu = 0.2$ V/s show a rise in current density in potential regions where formate adsorption is observed, as in Fig. 3.1. This is assigned to adsorbed formate oxidizing to CO_2, and referred to as j_{ox}. Oxidation onset and the maximum j_{ox} achieved improve with [HCOOH] and are adversely affected by [H_2SO_4]. Some j_{ox} vs potential curves are included in Fig. 3.5. The form of these curves is usually different from those measured in $HClO_4$ solutions, with j_{ox} curving from 0 up to a ca. linear current density vs potential trend. Usually, no maximum limiting j_{ox} is reached before the onset of Au oxidation (ca. 1.25 V). In $HClO_4$ solutions [34] and at the lowest [H_2SO_4]:[HCOOH], a plateau in current at $E \gtrsim 1.1$ V vs RHE is normal. Note that the maximum current observed is the same as the maximum seen in $HClO_4$ solution.

Other significant details include the independence of j_{ox} from ν and stirring of electrolyte. This is indicative of no mass transport limitations on HCOOH and reflects the speed of formate adsorption. Independence of j_{ox} from ν has been reported before [12, 14, 34].

Current Densities vs [HCOOH] and [H_2SO_4]

Trends of j_{ox} vs solution composition yield important information on the reaction order of formate. The most telling trend is j_{ox} vs [HCOOH] at 0.6 V, included in Fig. 3.6. Here, j_{ox} is linear with [HCOOH], with slope increasing at decreased [H_2SO_4]. This type of behaviour applies so long as $j_{ox} \lesssim 60$ μA/cm^2. Similar behaviour was seen in $HClO_4$ solutions [34], but was restricted to the low coverage limit for formate ($j_{ox} < 3$ μA/cm^2). This significant change implies major differences in the mode of

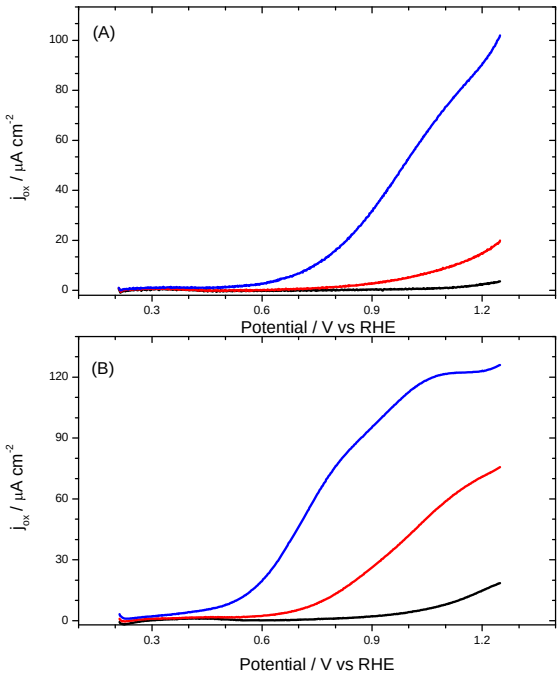

Figure 3.5: j_{ox} vs potential in (A) 1 or (B) 0.05 m H_2SO_4. [HCOOH] = 0.01 (black), 0.1 (red) or 1 m (blue).

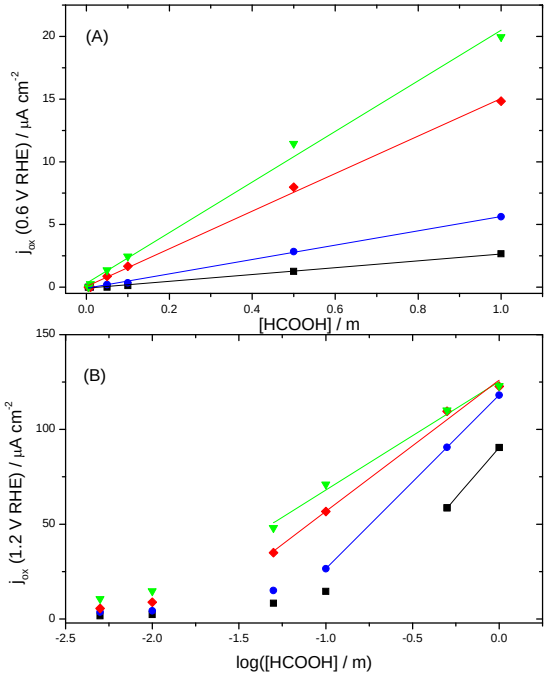

Figure 3.6: (A) j_{ox} at 0.6 V RHE as a function of [HCOOH]. (B) j_{ox} at 1.2 V RHE as a function of log[HCOOH]. [H_2SO_4] = 0.05 (▼, green), 0.1 (♦, red), 0.5 (●, blue), 1 m (■, black). Parameters for linear trends are included in Supporting Information.

formate oxidation.

Linearity of j_{ox} with log[HCOOH] was observed in $HClO_4$ solutions [34], at $j_{ox} > 20$ μA/cm^2. For H_2SO_4 solutions, j_{ox} shifts from linear vs [HCOOH] at $j_{ox} < 40$ μA/cm^2 to become linear vs log[HCOOH] at $j_{ox} > 75$ μA/cm^2. Slopes in this regime are proportional to [H_2SO_4].

In order to discern the reaction order of formate, j_{ox} must be correlated to the amount of adsorbed formate. The charge of adsorbed formate was assessed by integrating the difference in fast sweep current without HCOOH from that with HCOOH. The accuracy of these baseline corrections is doubted above low coverages, as there

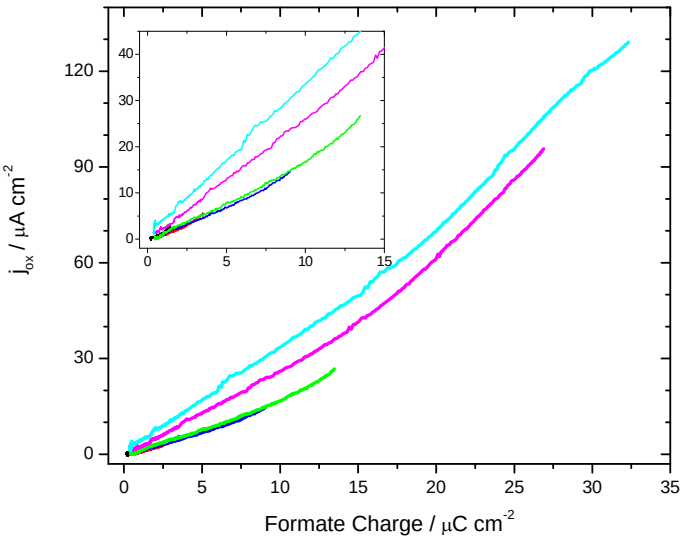

Figure 3.7: j_{ox} as a function of adsorbed formate charge for $[H_2SO_4]$ = 0.5 m and [HCOOH] = 0.005 (black), 0.01 (red), 0.05 (blue), 0.1 (green), 0.5 (magenta) and 1 m (cyan). Inset: low charge regime.

is a distinct rise in the capacitance baseline with increasing formate coverage. This is exemplified by the dropoff of formate adsorption currents to a plateau well above the capacitance baseline measured in the absence of HCOOH. This is seen in Fig. 3.3 A) and B). For higher [HCOOH]:$[H_2SO_4]$, capacitance is higher accross the whole potential range (Fig. 3.3 B)). These deviations lead to overestimation of the formate coverage, becoming worse with higher coverage. The expected maximum coverage of type B formate is 21.8 μC/cm^2 [34], but as much as 40 μC/cm^2 is calculated with the capacitance increase. Therefore, correlation of j_{ox} to formate coverage is only interpreted for formate coverage $\leq$ 12.5 μC/cm^2, and when fast sweep currents before formate adsorption are ca. equal those from HCOOH free CVs. The dependence of j_{ox} on formate charge can be seen in Fig. 3.7.

The most notable feature in Fig. 3.7 is the linearity of j_{ox} vs formate coverage below 12.5 μC/cm^2, and its superposition for [HCOOH] $<$ 0.1 m. The slope of lines

$\leq 12.5\ \mu C/cm^2$ is fixed for [HCOOH] ≤ 0.5 m, found as $1.6 \pm 0.3\ s^{-1}$ over all valid data sets. At higher [HCOOH]:[H_2SO_4], the slopes increase, suggesting a change in behaviour.

3.4 Discussion

3.4.1 Sulfate Adsorption in H_2SO_4 Solution

There is some disparity in the literature on the identity of the adsorbed form of sulfate. An early study [35] holds that moderate coverages of HSO_4^- adhere to Au(111) surfaces, with maximum coverages of 0.4 monolayers (ML). This conclusion was reached using STM images that show two different height maxima in sulfate adlayers (0.4 maxima per Au atom). The assignment of HSO_4^- as the adsorbed species was also made in some subsequent publications [20, 38] based on mass : charge ratios from EQCM work on both Au(111) and Au(poly). This conclusion ignored the possiblity of strong coadsorption of water, and that a positive surface excess of cations might exist. Later work [36, 37, 39, 40] suggests that it is in fact sulfate adsorbed onto the Au electrode surface at 0.2 ML. A new interpretation of STM data suggested a SO_4^{2-} coverage of 0.2 ML, which predicts the previously observed charges [37]. STM studies on Au(111) reproduced earlier results but interpreted the two height maxima as SO_4^{2-} and H_2O [40] / H_3O^+ [37] hydrogen bond bridges between anions. Coadsorption of water with sulfate might explain the high mass:charge ratios seen by Uchida et al [20, 38]. This structure is a $\sqrt{3} \times \sqrt{7}$ adlayer in the limit of high potential and coverage, with a similar structure found on Au(100) [41] (approximately $\sqrt{2} \times \sqrt{13}$). The $\sqrt{3} \times \sqrt{7}$ structure has been predicted using an elongated hard hexagon isotherm in Monte-Carlo simulations [47, 48]. An approach using radiotracers [36] gave good agreement with previous studies and showed that there are more sulfates adsorbed than charges on the metal side of the interface. This implies excess positive charges

are accumulated on the solution side of the interface to respect charge balance. This might lend support to the idea of H_3O^+ coadsorption as a hydrogen bond bridge [37] between adsorbed SO_4^{2-}. However, this theory is rejected by Osawa et. al. in favor of H_2O playing this role (based on their assignment of vibrational bands from in situ IR spectroscopy).

Results in this study corroborate the idea of sulfate being the dominant surface species. The most important results in this respect are the trends of peak potential vs $[H_2SO_4]$ or pH. If we write a pair of Nernst equations based on the stoichiometries of Eqs. (3.5) and (3.6), predicted peak potential vs $[H_2SO_4]$ and pH trends fit with experimental data. Note that these stoichiometries imply that singly charged sulfate is expected on the Au surface. This treatment assumes fardaic electron transfer, but the clear separation of faradaic and capacitive contributions is not possible in the general cases as shown by Delahay **[43–45]**. Lipkowsky et al. have emphasized that in electrocapillarity theory, the amount of charge flowing to the interface per adsorbate cannot be unambiguously interpreted as charge transferred from the adsorbate **[46].**

$$HSO_4^- \rightleftharpoons SO_4^-(\text{ads}) + H^+ + e^- \tag{3.5}$$

$$SO_4^{2-} \rightleftharpoons SO_4^-(\text{ads}) + e^- \tag{3.6}$$

Sulfate adsorption manifests itself as two current density peaks, seen in Fig. 3.2 (A) and 3.3. The adsorption is electrochemically reversible, as peak shape and position do not change at varied ν (0.2 - 100 V/s). For reversible adsorption, adsorption purely from sulfate is expected to display no pH dependence. However, a pH dependence of -59.2 mV/pH is expected for adsorption purely from bisulfate. The pH dependence of adsorption peaks is shown in Fig. 3.2 (B). When sulfate dominates in solution, i.e. pH $>> pK_a(HSO_4^-)$ (1.99), the peak potential vs SHE for adsorbing sulfate remains fixed vs pH. When bisulfate dominates in solution, i.e. pH $\lesssim pK_a(HSO_4^-)$, the peak potential vs SHE for adsorbing sulfate shifts at -54.7 mV/pH.

A -59.2 mV/log[H_2SO_4] shift on the RHE scale is expected, as increasing [SO_4^{2-}] + [HSO_4^-] promotes adsorption. A -61.1 mV/log[H_2SO_4] shift is measured. All these trends agree with predictions from Eqs. (3.5) and (3.6). It should be emphasized that the Au(poly) electrodes used have significant roughness (roughness factor = 2.3), and may have many defect sites on the surface where this adsorption / charge transfer reaction takes place. Sulfate adsorption accompanied by faradaic charge transfer might not be a universal phenomena.

The peak potential for the large, lower-potential sulfate peak is in good agreement with that seen on Au(111) in a study by Weaver et al. [37]. The high-potential shoulder on the adsorption peak seems to show similar separation from the main peak as the current spike associated with the SO_4^-(ads) gas-like to solid-like phase transition. It is tentatively proposed that this high-potential shoulder represents this very same phase transition, but is heavily broadened by the heterogeneity of the electrode. Regardless of its origin, sulfate adsorbing in this higher potential shoulder will be called "weakly bound sulfate", and the remainder "strongly bound sulfate".

3.4.2 Formate Adsorption in H_2SO_4 Solution

In $HClO_4$ solutions [34], reversible adsorption of formate onto Au was seen, by virtue of its accompanying electron transfer. This behaviour has also been observed in H_2SO_4 solutions, where fast sweep CVs show no dependence of formate charge vs potential on ν. This reversible adsorption was originally proposed by Crepy et al. [5].

Formate adsorption is much more suppressed than in $HClO_4$ solutions [34]. Whereas 21.8 - 40.3 $\mu C/cm^2$ of charge transfer was seen on Au in $HClO_4$ solutions, only 0.8 - 20.2 $\mu C/cm^2$ is observed in the presence of H_2SO_4. Distinct adsorption peaks are not observed unless [H_2SO_4]:[HCOOH] $\leq$ 2:1. Above this ratio, a small shoulder for formate adsorption is seen at potentials higher than sulfate adsorption. It is not obviously peak shaped, but seems to be formate adsorption because j_{ox} always rises in

the same potential region.

Two types of formate were observed to adsorb oxidatively on Au in $HClO_4$ solutions [34], and were named type A and type B formate. Type A formate appears to adsorb on sites typical for Au(111) or Au(110), with type B doing so on sites typical of Au(100). Type A formate has an E^0_{ads} of 0.374 V SHE, while type B formate has an E^0_{ads} of 0.785 V SHE. Given the potential at which the experimentally observed formate is adsorbing, it seems likely that the majority of adsorption here takes place as type B formate. In $HClO_4$ solutions, type B formate competes for sites with fully charged perchlorate, whose adsorption equilibrium constant is nearly potential *independent*. This leads to a peak of fixed size (21.8 μC/cm^2). Here peak size increases with [HCOOH]. Although type B formate adsorption is largely suppressed at high $[H_2SO_4]$:[HCOOH], it may approach to the same coverages as in $HClO_4$ solutions. Growing peak size with [HCOOH] was seen for type A formate in $HClO_4$ solutions, and was modelled as formate competing with potential *dependent* adsorption of supporting anions. It would seem that the potential dependence of sulfate adsorption onto the same sites as type B formate has modified its behaviour accordingly. It seems likely that weakly bound sulfate is displaced from Au with decreased $[H_2SO_4]$:[HCOOH], as this peak's potential is comparable to that of formate adsorption. This is not visible for the strongly bound sulfate peak, which does not change drastically in the parameter space investigated.

The decrease in formate peak potential is linear in log[HCOOH], with slopes $<$ -59.2 mV (-121 to -233 mV/log[HCOOH]). Evidently peak potential is more sensitive to log[HCOOH] as supporting electrolyte levels are increased. Slopes $<$ -59.2 mV were also seen for formate in $HClO_4$ solutions [34], athough under the right conditions formate peaks were found to shift at ca. -59.2 mV per decade of [HCOOH] and $[H^+]$. This confirmed the stoichiometry of Eq. (3.1). Rising peak potential indicates suppression of formate adsorption. Peak potential increases with $[H_2SO_4]$ can only be explained by sulfate adsorption, since adsorption according to Eq. (3.1) has the

same pH dependence as the RHE electrode.

Formate peaks are wide, much more so than the 91 mV full width half maximum (FWHM) predicted by the Langmuir model. This is similar to results in $HClO_4$ solutions [34], where electrode heterogeneity accounted for peak widths. The electrode used in this study is the same as for the previous study, and preparation procedures were identical. Accurate peak widths are difficult to assess without some form of peak deconvolution. However, the adsorption of formate over most of the double layer region has been observed in many previous studies [5, 8, 11, 14, 15].

3.4.3 Oxidation Currents in H_2SO_4 Solution

Magnitudes of j_{ox} were comparable to those measured on Au(111) by Avramov-Ivic et. al. [9]. Trends of j_{ox} vs E agree well in shape with all previous studies. Oxidation current is found only in potential regions and solution compositions where formate adsorption is observed, an indication that formic acid oxidation proceeds through adsorbed formate as an intermediate. This is in keeping with all mechanisms in the literature. As was demonstrated in $HClO_4$ solutions in several studies [11, 15, 34], j_{ox} depends on formate coverages alone at constant temperature. This is further supported by the high potential j_{ox} plateau at the highest [HCOOH]:[H_2SO_4], e.g., Fig. 3.5 (B), which coincides with the tapering off of the formate adsorption peak in Fig. 3.3 (B). In contrast, if adsorption does not taper off before the upper potential limit, j_{ox} is not seen to plateau. This implies a chemical rate limiting step as put forward by Cuesta and coworkers (potential independent rate constant).

Current magnitudes are often reduced when switching $HClO_4$ for H_2SO_4 at the same concentration, but not always. For the highest [HCOOH]:[H_2SO_4], currents are often equal to those seen in an equivalent $HClO_4$ solution. This is a consequence of type B formate competing for sites primarily with potential dependent sulfate adsorption (Equations (3.5), (3.6)) instead of potential independent perchlorate adsorption,

as was seen for type B formate in $HClO_4$ solutions. Suppression of formate adsorption is complete at lower [HCOOH]:[H_2SO_4], but can be overcome completely at higher ratios.

An interesting result is the linearity of j_{ox} with [HCOOH] for ca. half of the observed j_{ox} range, e.g., Fig. 3.6. This was seen in $HClO_4$ solutions [34], where it was restricted to the low coverage limit for formate ($j_{ox} < 3$ μA/cm^2). At this limit, the Langmuir or Sips isotherm [23] predicts linearity of coverage with concentration of adsorbing species. Therefore, a first-order dependence on formate made j_{ox} linear with [HCOOH]. The situation seems much different here, as j_{ox} vs [HCOOH] is linear at much higher j_{ox} and coverages. It is unlikely that this is a first-order dependence on dissolved [HCOOH]. Plotting j_{ox} from Fig. 3.6 vs log[H_2SO_4] yields another set of straight lines. This graph is included in the Supporting Information. A linear drop in formate coverage against log[H_2SO_4] is expected when formate and sulfate compete for the same sites, implying that j_{ox} has a first-order dependence on type B formate.

Trends from Fig. 3.7 are essential in assigning a mechanism to formate oxidation, and can support the proposal for a first-order dependence on type B formate. At type B formate coverage < 12.5 μC/cm^2, oxidation rate is dependent only on the amount of formate adsorbed, shown by the superposition of j_{ox} vs formate charge when [HCOOH] < 0.5 m. This is evidence of a rate limiting chemical step [11, 15], not electron transfer **??**. The simplest mechanism to explain low coverage and low [HCOOH] oxidation rates is first order oxidation of formate, as in Eq. (3.7). This was seen for oxidation of type A formate in $HClO_4$ solutions [34]. The formate observed here is type B formate, and first order kinetics cannot explain high [HCOOH] behaviour. In $HClO_4$ solution, type B formate reacts in a second order fashion with type C formate to yield CO_2 (Eq. (3.8)). It is possible that this also occurs here. Type C formate retains full charge on adsorption, contributing no adsorption current and leading to a ca. potential independent adsorption constant. Adsorbed sulfate would be expected to outcompete type C formate in occupying sites, since its adsorption

constant rises exponentially with potential. Increases in rate vs coverage consistently occur when sulfate adsorption is expected to be heavily perturbed by type B formate adsorption. It may be that only small amounts of type C formate may be present on the surface along with sulfate (explaining lower j_{ox} vs $\theta_{HCOO,B}$ in low [HCOOH] regime). When sulfate is displaced by type B formate adsorption, this may create room for type C formate, increasing the slope of j_{ox} vs $\theta_{HCOO,B}$ at higher $\theta_{HCOO,B}$. Type B and type C formate were found to coadsorb on Au in $HClO_4$ solutions [34].

$$j_{ox} = k_{ox} \cdot \theta_{HCOO,B} \tag{3.7}$$

$$j_{ox} = k_{ox} \cdot \theta_{HCOO,B} \cdot \theta_{HCOO^-,C} \tag{3.8}$$

3.5 Conclusion

Reversible sulfate adsorption obeying the stoichiometry of Equations (3.5) and (3.6) was observed. Formate was seen to adsorb reversibly on Au(poly) in H_2SO_4 solutions as the previously observed type B formate [34], according to the stoichiometry of Eq. (3.1). This type of formate is hypothesized to adsorb on sites typical of Au(100) surfaces. Both formate and sulfate adsorption occur on the same surface sites, so competition for sites leads to suppression of formate adsorption with increasing $[H_2SO_4]$:[HCOOH]. The amount of formate detected for [HCOOH] = 0.005 - 1 m and $[H_2SO_4]$ = 0.05 - 1 m ranged from 0.8 - 20.2 $\mu C/cm^2$, up to the minimum amount of formate seen in $HClO_4$ solutions [34]. Oxidation of formic acid is only seen in potential regions with adsorbed formate, and only increases with increasing formate coverage. This fits with rate limiting oxidation of formate through a chemical step [11, 15, 34]. j_{ox} is in general lower than in $HClO_4$ solutions, but for low $[H_2SO_4]$:[HCOOH] maximum catalytic activity matches that in $HClO_4$ solutions. Trends for j_{ox} vs solution composition are in general difficult to interpret, but linearity of j_{ox} vs [HCOOH] for $j_{ox} \lesssim 60\ \mu A/cm^2$ is typical, and linearity of j_{ox} vs formate charge is also seen. A first-

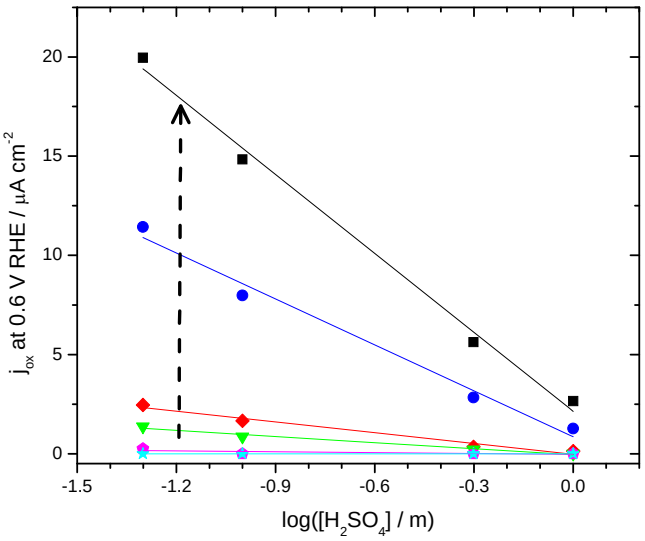

Figure 3.8: Oxidation current density, j_{ox}, vs $\log[H_2SO_4]$. [HCOOH] = 0.005, 0.01, 0.05, 0.1, 0.5, and 1 m. Arrow indicates increasing concentration.

order dependence of oxidation rate on type B formate coverage seems likely, as well as a rate dependence on another variety of formate, assumed to be type C formate [34].

3.6 Supporting Information

Fig. 3.8 shows the dependency of oxidation current densities on $\log[H_2SO_4]$, representative for current densities $\lesssim 50\ \mu A/cm^2$.

Contained within Table 3.1 are the parameters for all peak potential against solution composition linear fits shown in this work. Table 3.2 holds all parameters from linear fits of j_{ox} vs solution composition.

e

E_{Peak,SO_4^-} vs pH:	Slope / mV SHE:	Intercept / mV SHE:
pH $\leq$ 2.5	-54.7	300
pH $\geq$ 2.5	-0.144	159
$E_{\mathrm{Peak,HCOO}}$ vs log[HCOOH]	Slope / mV RHE:	Intercept / mV RHE
$[H_2SO_4]$ = 0.05 m	-121	764
$[H_2SO_4]$ = 0.1 m	-136	788
$[H_2SO_4]$ = 0.5 m	-179	823
$[H_2SO_4]$ = 1 m	-233	867

Table 3.1: Parameters from Linear Fits of Adsorption Peak Potential at Varying Solution Composition in the Sulfuric and Formic Acid System.

j_{ox} vs log$[H_2SO_4]$ at E = 0.6 V RHE:	Slope / μA cm^{-2}:	Intercept / μA cm^{-2}:
[HCOOH] = 1 m	-13.3	2.14
[HCOOH] = 0.5 m	-7.72	0.855
[HCOOH] = 0.1 m	-1.81	-0.0272
[HCOOH] = 0.05 m	-1.03	-0.0590
[HCOOH] = 0.01 m	-0.148	-0.0342
[HCOOH] = 0.005 m	0.00	0.00
j_{ox} vs log[HCOOH], E = 1.2 V RHE:	Slope / μA cm^{-2}:	Intercept / μA cm^{-2}:
$[H_2SO_4]$ = 1 m	90.4	105
$[H_2SO_4]$ = 0.5 m	91.6	118
$[H_2SO_4]$ = 0.1 m	69.3	126
$[H_2SO_4]$ = 0.05 m	57.2	125
j_{ox} vs [HCOOH], E = 0.6 V RHE:	Slope / μA cm^{-2} m^{-1}:	Intercept / μA cm^{-2}:
$[H_2SO_4]$ = 1 m	2.72	-0.0814
$[H_2SO_4]$ = 0.5 m	5.72	-0.0862
$[H_2SO_4]$ = 0.1 m	15.0	0.0651
$[H_2SO_4]$ = 0.05 m	20.2	0.313

Table 3.2: Parameters from Linear Fits of Oxidation Current Density vs Solution Composition in the Sulfuric and Formic Acid System.

Chapter 4

The Role of Available Sites in the Activity of Lattice Gases with Geometric Constraints[1]

4.1 Introduction

This paper concerns lattice-gas systems with only geometric constraints, i.e., systems where the configurations with given numbers of particles of various species all have the same energy. The geometric constraints may be non-trivial, for example, type A particles may be forbidden from occupying sites adjacent to type A particles, but may be allowed to be adjacent to type B particles; these types of interactions are the lattice equivalent of non-additive exclusion interactions in continuous hard-sphere models. Locality-specific constraints are also allowed, e.g., a line of lattice sites where occupancy is forbidden for one or more species. A simple statistical-mechanical derivation is first used to show that the activity is the ratio of the number of particles to the

[1]This chapter was published as a paper in the Journal of Chemical Physics [1], http://dx.doi.org/10.1063/1.4820400

number of available sites. The terminology of 2-D adsorption systems will be used here: counts of adsorbed species or available sites are normalized by the number of lattice sites and written as coverages θ or $\theta_{\rm av}$, and so we write the activity $a = \theta/\theta_{\rm av}$. However, the arguments may be applied also to 3-D systems and systems that do not have the adsorption sites strictly arrayed in a lattice.

The key role of $\theta_{\rm av}$, the sites available for occupation, is emphasized. (Throughout this paper, adsorption occurs at a specific site or location, which counts as one even though it may cover or exclude more than one lattice site.) Available sites may be different for different species and are not necessarily just unoccupied lattice sites. The key role of available sites is the lattice-gas equivalent of the key role of spare or available volume in the statistical geometry of continuous hard-sphere systems [49–52]. Our derivation of the activity is an extension to lattice gases of the derivation of Speedy for hard spheres [49] or of Corti and Bowles for hard-sphere mixtures [52]. Derivations directly linking addition of a particle to chemical potential, as here, originate with Widom's particle insertion method [53] Widom's method was applied to lattice gas systems before [54–57], but the key significance of the number of available sites did not seem to be recognized. The work by Soto-Campos et. al. [58] does not use the particle addition method, but does point out the key role of the available sites for hard rod systems. They conjectured that their equivalent of $a = \theta/\theta_{\rm av}$ had more universal validity, but proved it only for hard rods on a 1-D lattice.

A simple derivation of the Langmuir adsorption isotherm is a trivial result of the theory, but the theory applied to the hard hexagon model and mixed hard hexagon/Langmuir systems provides non-trivial applications. The hard hexagon model describes adsorption on a triangular lattice in which nearest neighbor adsorption is forbidden, so that the "exclusion zone" around an adsorbate is a hexagon. This is one of the few statistical-mechanical lattice models with an exact solution, found by Baxter [59, 60], and recast in an algebraic form by Joyce [61, 62]. There is a phase transition from 2-D gas to coexistence of 2-D solid and gas phases when

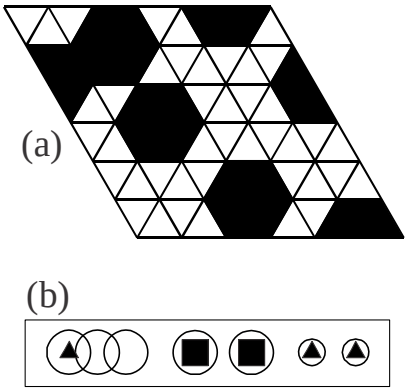

Figure 4.1: Surface configurations. (a) A configuration of hard hexagons on a triangular lattice of $M = 36$ sites with $N = 5$ adsorbed species (black hexagons), $N_{\mathrm{av}} = 6$ available sites (vertices not touching hexagons) and 25 forbidden lattice sites (at the vertices of the hexagons). Periodic boundary conditions mean the right and bottom edges are duplicates of the left and top edges. (b) A configuration of an artificial surface discussed in the text, with $M = 7$, $N_{\blacksquare} = 2$, $N_{\blacktriangle} = 3$, $N_{\mathrm{av},\blacksquare} = 1$ (site 3 only), $N_{\mathrm{av},\blacktriangle} = 2$ (sites 2 and 3).

the coverage exceeds a critical coverage $\theta_{\mathrm{c}} = 0.276$. The complexity of the model arises from the fact that different configurations with the same number of adsorbates nonetheless have different numbers of available sites for further adsorption, because the number of unoccupied lattice sites adjacent to adsorbates (forbidden lattice sites) depends on the configuration (Fig. 4.1(a)).

The hard hexagon model is of interest for two reasons. Firstly, it appears to explain some experimental results in surface science and electrochemistry [63–68]. Secondly, as a model system with a phase transition and an analytical solution, it can be used to verify methodologies independently of any experimental or theoretical approximations. For example, Nagai [69] used it as a test case to decide between two versions of transition-state theory in thermal desorption spectroscopy. In electrochemistry, the mean-field solution of the Ising lattice-gas model with nearest-neighbour interactions of energy ε_{nn} is known as the Frumkin isotherm and is frequently used to simulate voltammograms with phase transitions. However, the well-known deficien-

cies of the mean-field model mean that the mean-field phase transition at the non-dimensionalized interaction (Frumkin) parameter $g = c\varepsilon_{nn}/kT = -4$ is far from the true (square lattice, coordination number $c = 4$) value of $g = -7.05$ [70]. Therefore inadequacies of fits of the Frumkin model to experimental data may be due either in deficiencies in the mean-field approximation, or that the underlying nearest-neighbor interaction model does not apply in the experimental system. Nonetheless, the Frumkin model remains widely used simply because it has an analytical solution, and alternatives such as Monte-Carlo calculations are more complex and slower computationally. This is especially an issue in voltammetry or thermal desorption spectroscopy, as these methods require solutions over the whole coverage range.

Armed with an analytical expression for θ_{av} for the hard hexagon model, we show how to combine hard-hexagon adsorbates with Langmuir adsorbates in a competitive adsorption model. An interesting aspect of this is how the Langmuir adsorbates may disrupt the phase transition. There are only a few rigorous results for phase transitions of lattice gas mixtures, e.g., [71–73] We also formulate a kinetic version of the hard-hexagon model that requires only solution of an ordinary differential equation to determine coverage-time behavior, and use it to simulate voltammograms for electrochemical adsorption.

4.2 Theory

We consider a lattice gas model with the following assumptions:

1. The temperature and area of the surface (number of surface sites on the empty surface, M) are fixed. The Helmholtz energy A is therefore the appropriate free energy variable.

2. The internal motions of the adsorbates are independent of any interaction energies between them.

3. The chemical potential is defined as the work to add a particle (adsorbate) of a given type i to the system, $\mu_i = A_{N_i+1} - A_{N_i}$, even for a system with finite numbers of sites and adsorbates.

4. Geometric constraints forbidding adsorption at certain locations are allowed, but addition of a particle of type i to any of the locations available to it leads to the same change in energy.

Here we consider two canonical ensembles with fixed particle numbers for all s species, one with particle counts $N_1, N_2, \ldots, N_s$ and partition function $Q(N_1, N_2, \ldots, N_s)$ that we abbreviate Q_{N_i}, and another with one particle of species i added, $Q(N_1, \ldots, N_{i-1}, N_i+1, N_{i+1}, \ldots, N_s)$ that we abbreviate Q_{N_i+1}. Similar abbreviated notation is used for the number of configurations, Ω_{N_i} or Ω_{N_i+1} and Helmholtz energies, A_{N_i} or A_{N_i+1}.

Assumptions 1 and 2 are conventional for lattice gas theory. The philosophy here is slightly different from Widom's, in that we take the chemical potential expression $\mu_i = A_{N_i+1} - A_{N_i}$ (assumption 3) to be exact for a finite system, as is occasionally done, e.g., [74–77]. In the thermodynamic limit of large N_i this definition agrees with the usual one, because it is just the finite difference approximation to the derivative.

$$\mu_i = A_{N_i+1} - A_{N_i} = \frac{A_{N_i+1} - A_{N_i}}{(N_i+1) - N_i} \tag{4.1}$$

$$\underset{N_i, N_{j\neq i}, M=\infty}{\longrightarrow} \left(\frac{\partial A}{\partial N_i}\right)_{T,M,N_{j\neq i}} \tag{4.2}$$

The limit is taken for $N_i \to \infty$, $N_j \to \infty$, $M \to \infty$ with $\theta_i = N_i/M$ and the other particle coverages $\theta_j = N_j/M$ constant. Han et al [78], in a more typical approach, have discussed different finite difference approximations to the "real" (partial-derivative) chemical potential. Since we are developing analytical results only in the thermodynamic limit, the philosophical issue is immaterial for practical purposes. However, we suggest that deriving the chemical potential exactly for a finite system, and then approaching the thermodynamic limit, instead of finding the free energy in the ther-

modynamic limit and then differentiating to find the chemical potential, may offer insights in solving exactly some statistical models of interest. The geometric constraints referred to in assumption 4 are effectively infinite energy repulsions that do not introduce an energy parameter into the problem. These are similar to the hard-wall repulsions or volume exclusion interactions in continuous hard-particle systems. The possibilities and limitations of these constraints will be discussed in more detail in Sec. 4.3.1.

According to assumptions 2 and 4, the canonical partition function is given by Eq. (4.3), where Ω_{N_i} is the number of ways of arranging *all* adsorbates on the surface, i.e., $k \ln \Omega_{N_i}$ is the configurational entropy for the system. (The adsorption energies ε_i, ε_j could alternatively be included in the molecular partition functions q_i, q_j). Proceeding to calculate the chemical potential from the Helmholtz energy, Eq. (4.4), using $\mu_i = A_{N_i+1} - A_{N_i}$ and keeping T, M, N_j constant gives Eq. (4.5), and the activity takes the particularly simple form of Eq. (4.6)

$$Q_{N_i} = \Omega_{N_i} \left(q_i \exp(-\varepsilon_i/kT)\right)^{N_i} \prod_{j \neq i} \left(q_j \exp(-\varepsilon_j/kT)\right)^{N_j} \tag{4.3}$$

$$A_{N_i} = -kT \ln Q_{N_i} \tag{4.4}$$

$$\begin{aligned} \mu_i = A_{N_i+1} - A_{N_i} &= (-kT \ln q_i + \varepsilon_i) + kT \ln \left(\Omega_{N_i}/\Omega_{N_i+1}\right) \\ &= \mu_i^{\circ} + kT \ln \left(\Omega_{N_i}/\Omega_{N_i+1}\right) \end{aligned} \tag{4.5}$$

$$a_{i,N_i} = \Omega_{N_i}/\Omega_{N_i+1} \tag{4.6}$$

As an immediate application of this, consider the case of addition of one Langmuir adsorbate (no lateral interactions) to a system of N such adsorbates (the subscript i is redundant here since there is only one species). Then $\Omega_N = \binom{M}{N}$ and the activity is given by

$$a_N = \binom{M}{N} \Big/ \binom{M}{N+1} = \frac{N+1}{M-N} = \frac{(N+1)/M}{1 - N/M}. \tag{4.7}$$

The numerator is the coverage for the system with $N+1$ adsorbates, i.e., after addition, and we use a prime to distinguish this from the coverage before addition, θ. The activity for the finite system is therefore

$$a_N = \frac{\theta'}{1-\theta} \tag{4.8}$$

Given assumption 3, this is an exact result. In the thermodynamic limit, there is no distinction between θ' and θ, and we arrive at the well-known result $a = \theta/(1-\theta)$, derived rather simply and without recourse to Stirling's approximation. A similar calculation for two types of Langmuir adsorbates A and B competing for the same sites leads to $a_{\mathrm{A},N} = \theta'_{\mathrm{A}}/(1-\theta_{\mathrm{A}}-\theta_{\mathrm{B}})$ and $a_{\mathrm{B},N} = \theta'_{\mathrm{B}}/(1-\theta_{\mathrm{A}}-\theta_{\mathrm{B}})$.

We now show that rather generally the activity is given by $\theta'_i/\langle\theta_{\mathrm{av},i}\rangle$, where the angle brackets denote an ensemble average for the system with N_i adsorbates. Consider a configuration k of the system containing N_i adsorbates that has $N_{\mathrm{av},i}(k)$ possible locations to add the next adsorbate. Adsorbate here refers to the type for which we are to calculate the activity; there may be many other types of adsorbates, provided the number of each does not vary in the different configurations. Add up all the available sites from all the Ω_{N_i} configurations, to give an ensemble total $T_{\mathrm{av},i} = \sum_{k=1}^{\Omega_{N_i}} N_{\mathrm{av},i}(k)$. Now make new configurations by adding an adsorbate to each of these $T_{\mathrm{av},i}$ sites. Each of the resulting $T_{\mathrm{av},i}$ configurations will be identical to N_i others, because any of the indistinguishable N_i+1 adsorbates could have been the one just added. So the correct number of configurations with N_i+1 adsorbates is

$$\Omega_{N_i+1} = T_{\mathrm{av},i}/(N_i+1). \tag{4.9}$$

The ensemble average of the number of available sites before the addition is $\langle N_{\mathrm{av},i}\rangle = T_{\mathrm{av},i}/\Omega_{N_i}$ and this may be combined with the above equation to give

$$\frac{\Omega_{N_i+1}}{\Omega_{N_i}} = \frac{\langle N_{\mathrm{av},i}\rangle}{N_i+1}. \tag{4.10}$$

Combining with Eq. (4.6) leads to a simple expression for the activity of species i for the finite system that has N_i particles of species i

$$\begin{aligned} a_{i,N_i} &= \frac{\Omega_{N_i}}{\Omega_{N_i+1}} = \frac{N_i+1}{\langle N_{\mathrm{av},i}\rangle} = \frac{(N_i+1)/M}{\langle N_{\mathrm{av},i}\rangle/M} \\ &= \frac{\theta_i'}{\langle \theta_{\mathrm{av},i}\rangle}. \end{aligned} \tag{4.11}$$

Note that the use of the average here does not involve any approximation. In the thermodynamic limit, this reduces to

$$a_i = \frac{\theta_i}{\theta_{\mathrm{av},i}}, \tag{4.12}$$

where $\theta_{\mathrm{av},i}$ means coverage of sites available for adsorption of species i.

4.3 Results and discussion

4.3.1 The nature of available sites and geometric constraints

We begin with a discussion of the limitations and possibilities of assumption 4. The simplest type of geometric constraint is that a lattice site already occupied is not available for further adsorption, which of course is the basis for the Langmuir adsorption model. More interesting are cases where adsorption on a lattice site excludes further adsorption on any other specified sites, such as the nearest-neighbor exclusions in the hard hexagon model. Richer possibilities are also entertained, as best demonstrated in terms of a small artificial example with non-trivial possibilities. (Further details of this example, including a figure showing all configurations, are given in the supplementary material [79].) Fig. 4.1(b) shows one configuration for a surface with seven sites (circles), two types of adsorbates (squares or triangles), and the following rules: Squares have hard repulsions between each other and the triangles to the extent

that for the leftmost three sites (overlapping circles), they cannot occupy neighboring sites. (Two triangles may be adjacent on these sites, though.) For the next two sites, either squares or triangles may adsorb without any restrictions. For the last two sites, only triangles may adsorb, again without restrictions. The configuration shown is one of 32 configurations with two squares and three triangles obeying these rules. If we now consider addition of a square to this system, there are 12 available sites amongst the 32 configurations that are suitable, so according to Eq. (4.9), there will be $12/3 = 4$ configurations with 3 squares and 3 triangles, as is easily verified. Similarly, for addition of a triangle to this system, there are 40 available sites amongst the 32 configurations that are suitable, leading to $40/4 = 10$ configurations with 2 squares and 4 triangles.

This example emphasizes that the meaning of "available" in the above derivation means available for adsorption of the type of adsorbate for which we are calculating the activity. Available is not the same as "free" in the sense of an unoccupied lattice site, and the available sites may be different for different adsorbates. (Fig. 4.1(b) has two unoccupied sites; both are available for adsorption of a triangle, but only one is available for adsorption of a square.) Different configurations may have different numbers of available sites, and there may be more that one type of site for adsorption, e.g., the two types of circles for triangle adsorption. This flexibility in site type is constrained by the requirement that there be the same adsorption energy for the different sites on which a species may adsorb. A practical example where rules like this might apply is adsorption on sites near a step edge, where large molecules might be excluded but smaller molecules might not be. Just as constraints may be location specific, they may also be non-local, e.g., specifying that particles may not be five lattice sites apart. There is no requirement that sites have any particular spatial relationship to each other, and so the derivation does not actually require a lattice gas system. The sites must be distinguishable: two sites at the same location are not allowed, or equivalently, adsorption of two particles of the same type at the same site

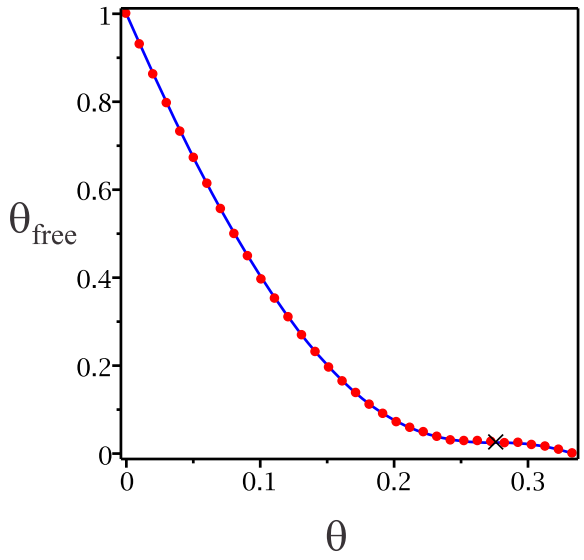

Figure 4.2: Available sites for the hard hexagon model. Solid line: analytical solution; the cross shows the phase transition point. Circles: result of Monte-Carlo simulations (every 11th point shown).

is not allowed.

4.3.2 Hard hexagons

The above derivation shows that the activity depends only on the average number of available sites, and not their distribution across members of the ensemble. The analytical solution of the hard-hexagon model expresses the activity, free energy per lattice site, or compressibility in terms of the coverage, and makes no reference to the available or forbidden sites. However, since the activity of the hexagons as a function of coverage, $a(\theta)$, is available, Eq. (4.12) immediately gives an exact analytical expression for the coverage of available sites for hard hexagons, $\theta_{\rm av} = \theta/a(\theta)$. The coverage $\theta_{\rm av}$ is given explicitly as a function of θ in the supplementary material [79], and is plotted in Fig. 4.2 . Taking the derivative at $\theta = 0$ yields the expected value of -7: the addition of an isolated adsorbate (hexagon) to an empty

lattice removes the central adsorption site and the six nearest neighbors. Similarly, the derivative at $\theta = 1/3$ is -1, consistent with filling the last, single-lattice-site holes in the solid-like adlayer.

To further verify that this expression for $\theta_{\rm av}$ represents the sites available for adsorption, Monte Carlo simulations were carried out on a 33×33 triangular lattice with periodic boundary conditions. Constant-coverage simulations were carried out for all numbers of adsorbates from two to maximum coverage. The final state of the surface after each simulation was used as the initial state for the sucessive one. The simulations consisted of first adsorbing the new adsorbate, followed by $1000\sqrt{N}$ migration steps in which a randomly selected adsorbate could move to a randomly-chosen available neighboring lattice site. The average coverage of available sites agrees with the analytical function to within ± 0.008, Fig. 4.2.

The Monte-Carlo simulations validate the meaning of $\theta_{\rm av}$ in the analytical expresssion, but involve some level of approximation. To verify that Eq. (4.9) is exact, it was tested by generating all configurations for a 6×6 surface with periodic boundary conditions. The 2^{36} configurations with all possibilities of lattice sites occupied or not were generated. This was done using a Gray code algorithm [80], which ensures that only neighbors of the adsorption or desorption lattice site need to be examined at each step. Invalid configurations with nearest-neighbor adsorption were eliminated. Counts of the numbers of occupied, forbidden and available sites were made for the remaining 162314 valid configurations of the grand canonical ensemble and $(N+1)\,\Omega_{N+1} - \sum_{k=1}^{\Omega_N} N_{\rm av}(k)$ was found to be exactly zero for all N up to 12, which corresponds to the maximum 1/3 coverage. Even for this small surface $\langle\theta_{\rm av}\rangle$ is surprisingly accurate, being within ± 0.02 of the analytical solution. Interestingly, the analytical expression is non-monotonic: it increases by 0.0002 between $\theta = 0.2734$ and 0.2792 (around the phase transition). The above tests do not have the resolution to verify this, and it does not influence the results presented below, but it does warrant further investigation.

4.3.3 Hard hexagons plus Langmuirs

Having an expression for the coverage of available sites for adsorption of hexagons enables consideration of mixed systems of some complexity, though some simplifying assumptions need to be made. We consider a mixed adsorbate system of hard hexagons and a second species ("Langmuirs"), which adsorb on the same lattice sites, but have no nearest-neighbor interactions and may adsorb on adjacent lattice sites. We may expect that in the thermodynamic limit the coverage of available sites for the Langmuir species is just the available coverage for hexagons in the hard hexagon model minus the Langmuir coverage θ_{L}. Therefore, the Langmuir activity is

$$a_{\mathrm{L}} = \frac{\theta_{\mathrm{L}}}{\theta_{\mathrm{av,H}} - \theta_{\mathrm{L}}}, \tag{4.13}$$

where the subcript H refers to the case of the pure hard-hexagon system *in the absence of Langmuirs*. The usual assumption is being made here: that the distribution of available sites in the hard hexagon model has negligible width in the thermodynamic limit. More formally, we note that in the mixed system, for every configuration k of hexagons with N_{H} hexagons and $N_{\mathrm{av,H}}(k)$ available sites, there are $\binom{N_{\mathrm{av,H}}(k)}{N_{\mathrm{L}}}$ arrangements of the N_{L} Langmuirs, so the number of configurations in the mixed model is

$$\Omega_{\mathrm{H+L}} = \sum_{k=1}^{\Omega_{\mathrm{H}}} \binom{N_{\mathrm{av,H}}(k)}{N_{\mathrm{L}}}, \tag{4.14}$$

where the binomial is to be interpreted as zero for $N_{\mathrm{L}} > N_{\mathrm{av,H}}(k)$. Under the assumption that $N_{\mathrm{av,H}}(k)$ may be approximated by its ensemble average, $\langle N_{\mathrm{av,H}} \rangle$,

$$\Omega_{\mathrm{H+L}} \approx \Omega_{\mathrm{H}} \cdot \binom{\langle N_{\mathrm{av,H}} \rangle}{N_{\mathrm{L}}} \tag{4.15}$$

and insertion into the free energy expression (Eqs. (4.3),(4.4)), differentiation with respect to N_{L}, and application of Stirling's approximation leads to Eq. (4.13). This derivation is relatively simple because Ω_{H} is independent of N_{L}. In the limit in which

the distribution of available sites becomes a delta function, Eq. (4.15) becomes exact.

The addition of hexagons to a mixed system is more complicated, because Langmuir adsorbates present configurations to the hexagons that are not envisaged in the pure hard-hexagon model, such as two (Langmuir) adsorbates on adjacent lattice sites. This considerably complicates the combinatorial problem. However, with the approximation described by Eq. (4.15), differentiation with respect to N_{H} leads to

$$a_{\mathrm{H}} = \frac{\theta_{\mathrm{H}}}{\theta_{\mathrm{av,H(mix)}}}, \tag{4.16}$$

where $\theta_{\mathrm{av,H(mix)}}$, the coverage of sites available to hexagons in the mixed system, is given by

$$\theta_{\mathrm{av,H(mix)}} = (\theta_{\mathrm{av,H}} - \theta_{\mathrm{L}}) \left(1 - \frac{\theta_{\mathrm{L}}}{\theta_{\mathrm{av,H}}}\right)^{-\left(d\theta_{\mathrm{av,H}}/d\theta_{\mathrm{H}}\right)-1}. \tag{4.17}$$

This expression for the available sites for hexagons may be checked under some limiting conditions. For $\theta_{\mathrm{L}} = 0$, $\theta_{\mathrm{av,H(mix)}} = \theta_{\mathrm{av,H}}$ as required. For a surface with coverage of hexagons close the the maximum of 1/3 and only a few Langmuirs, the Langmuirs fill some isolated holes and the remaining isolated holes are equally suitable for adsorption of hexagons or Langmuirs. In this limit, $d\theta_{\mathrm{av,H}}/d\theta_{\mathrm{H}} \approx -1$, and we find $\theta_{\mathrm{av,H(mix)}} \approx \theta_{\mathrm{av,H}} - \theta_{\mathrm{L}}$ as expected. When both Langmuirs and hexagons are dilute, a series expansion leads to $\theta_{\mathrm{av,H(mix)}} \approx 1 - 7\theta_{\mathrm{H}} - 7\theta_{\mathrm{L}}$, reflecting the fact that an added hexagon must avoid the 7 lattice sites occupied by and adjacent to Langmuirs and hexagons.

As an application of these equations, we consider the electrochemical adsorption of a mixture of hexagons and Langmuirs from a solution in which they each have unit

activity.

$$\mathrm{H^-(aq)} \rightleftharpoons \mathrm{H(ads)} + \mathrm{e^-} \tag{4.18}$$

$$\mathrm{L^-(aq)} \rightleftharpoons \mathrm{L(ads)} + \mathrm{e^-} \tag{4.19}$$

$$E = E^{\mathrm{o}}_{\mathrm{H}} + \frac{RT}{F} \ln a_{\mathrm{H}} \tag{4.20}$$

$$E = E^{\mathrm{o}}_{\mathrm{L}} + \frac{RT}{F} \ln a_{\mathrm{L}} \tag{4.21}$$

Solution of these Nernst equations with the activities above (Eqs. (4.13) and (4.16)), and the hard hexagon analytical expressions gives the coverages θ_{L} and θ_{H} as a function of potential, E. The experimental quantity measured in a slow sweep (reversible) voltammogram is the derivative of the charge passed, which is proportional to $d\left(\theta_{\mathrm{L}} + \theta_{\mathrm{H}}\right)/dE$, and is shown in Fig. 4.3. Numerical evaluation of the equations in the form given led to loss of significance, and so instead truncated series expansions of order 25 about $\theta_{\mathrm{H}} = 0$ of $\theta_{\mathrm{av,H}}$ and $d\theta_{\mathrm{av,H}}/d\theta_{\mathrm{H}}$ were used when $\theta_{\mathrm{H}} < 0.18$. The relative error in calculating $\theta_{\mathrm{av,H(mix)}}$ using this pair of series approximations was quantified at $< 0.25\%$. Numerical issues were more pronounced in the range $FE^{\mathrm{o}}_{\mathrm{L}}/RT = 2 - 2.5$, and there the analytical forms for $\theta_{\mathrm{av,H}}$ and $d\theta_{\mathrm{av,H}}/d\theta_{\mathrm{H}}$ were replaced with truncated series expansions (expanded about $\theta_{\mathrm{H}} = 0.15$ to order 25) from $\theta_{\mathrm{H}} = 0.18 - 0.276$, with relative error in $\theta_{\mathrm{av,H(mix)}}$ of less than 0.05%.

Increasing the potential promotes adsorption, and the standard potentials $E^{\mathrm{o}}_{\mathrm{H}}$ and $E^{\mathrm{o}}_{\mathrm{L}}$ represent the characteristic free energies for the adsorption of each type. For $E^{\mathrm{o}}_{\mathrm{H}} = 0$ and $E^{\mathrm{o}}_{\mathrm{L}}$ large, there is only adsorption of hexagons; the black curve at $E^{\mathrm{o}}_{\mathrm{L}} = 5RT/F$ shows the phase transition spike at approximately the pure hexagon value of $2.406 = \ln(11.09)$, where 11.09 is the critical activity. As expected, a trend of increasingly favorable Langmuir adsorption is seen with decreasing $E^{\mathrm{o}}_{\mathrm{L}}$. A small broadening of the hard hexagon phase transition is seen at $E^{\mathrm{o}}_{\mathrm{L}} = 2.5RT/F$ (red dashed curve). Here, there is a small coverage of Langmuirs on the surface across

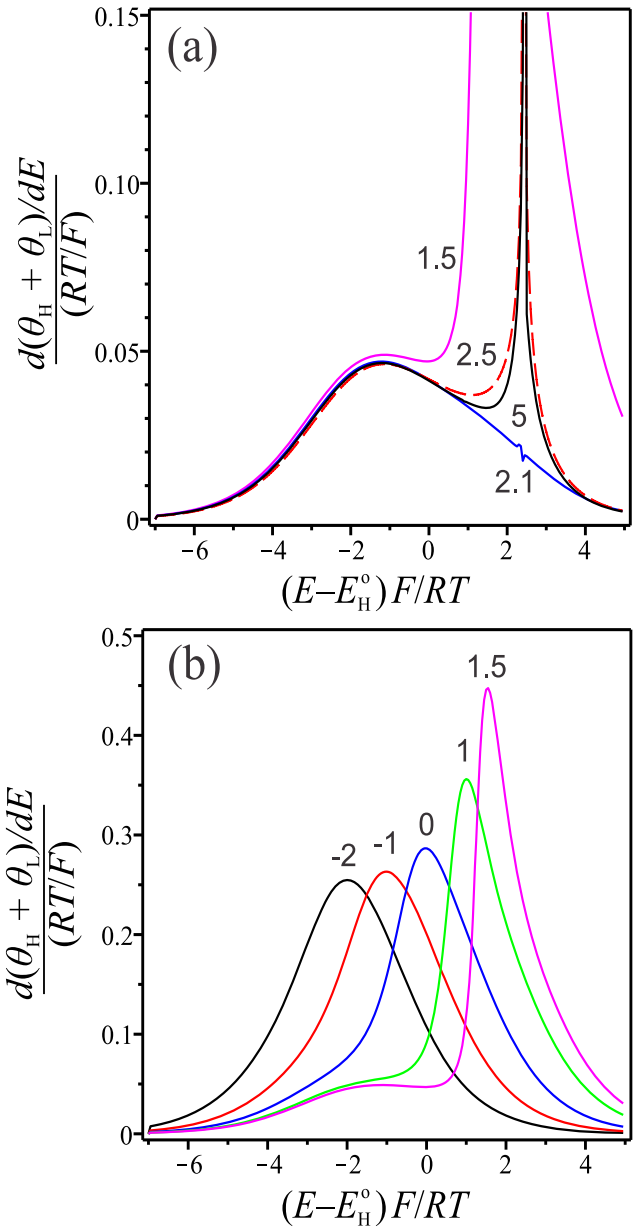

Figure 4.3: Mixed Hard-hexagon/Langmuir simulations. Reversible voltammograms for $E^o_H = 0$ and E^o_L varied. Curves labeled by FE^o_L/RT.

most of the displayed potential range. At $E_{\mathrm{L}}^{\mathrm{o}} = 2.1RT/F$, near perfect quenching of the phase transition is seen, and hard hexagons and Langmuirs are coadsorbed in appreciable amounts at higher potentials. For $E_{\mathrm{L}}^{\mathrm{o}} = 0 - 2.1\ RT/F$, no phase transition is in evidence and hard hexagons adsorb as a lower potential shoulder on a larger, primarily Langmuir based peak. Hard hexagon coverages are driven to zero in the potential range of Langmuir adsorption. Below $E_{\mathrm{L}}^{\mathrm{o}} = 0$, adsorption currents are derived almost purely from Langmuir adsorbates, and hard hexagons do not adsorb appreciably. These results follow the expected trend: as $E_{\mathrm{L}}^{\mathrm{o}}$ is decreased (which increases the tendency for the Langmuirs to adsorb), the shape of the voltammogram changes from one that resembles the adsorption of hard hexagons only to one that resembles the adsorption of purely Langmuir adsorbates. This happens over an $E_{\mathrm{L}}^{\mathrm{o}}$ range of about $7RT/F$.

4.3.4 Hard hexagons – kinetic extension

Having an expression for the coverage of available sites means that the adsorption and desorption rates may be decoupled and the system away from equilibrium may be considered. As an example, we consider the electrochemical adsorption of hexagons from a solution in which they are at unit activity, according to reaction (4.18). According to mass-action kinetics, the desorption rate of hexagons will be proportional to their concentration on the surface, θ_{H}, and the adsorption rate will be proportional the concentration of available adsorption sites, $\theta_{\mathrm{av,H}}$, leading to the rate law for net adsorption

$$r = v_{\mathrm{ads}} - v_{\mathrm{des}} = k_{\mathrm{ads}}\theta_{\mathrm{av,H}} - k_{\mathrm{des}}\theta_{\mathrm{H}}. \tag{4.22}$$

The equilibrium constant can be written as the activity of the species on the surface,

$$K = \frac{\theta_{\mathrm{H}}}{\theta_{\mathrm{av,H}}}. \tag{4.23}$$

The principle of detailed balance requires $v_{\rm ads} = v_{\rm des}$ at equilibrium, and this is satisfied by taking $K = k_{\rm ads}/k_{\rm des}$ (Other forms of the rate law consistent with detailed balance are possible, but the simple form of Eq. (4.22) is most consistent with an uncomplicated elementary reaction.). The governing differential equation is

$$\Gamma_{\rm m}\frac{d\theta_{\rm H}}{dt} = r = k_{\rm ads}\theta_{\rm av,H} - k_{\rm des}\theta_{\rm H}, \tag{4.24}$$

where $\Gamma_{\rm m}$ (mol m^{-2}) converts coverage to surface concentration. Since we have an analytical solution for $\theta_{\rm av,H}$ as a function of $\theta_{\rm H}$, we may solve the kinetic differential equation (4.24) and determine how the phase transition influences the kinetics. This is solved numerically in Fig. 4.4 for the electrochemical cyclic voltammetry case, where the rate constants depend exponentially on potential, $k_{\rm ads} = k^{\rm o}_{\rm ads}\exp\left((1-\beta)F(E-E^{\rm o})/RT\right)$, $k_{\rm des} = k^{\rm o}_{\rm des}\exp\left(-\beta F(E-E^{\rm o})/RT\right)$, and the potential is swept linearly with time at sweep rate v, $E = E(t=0) + vt$. The initial condition is that the equilibrium coverage applies at $t = 0$. Several sweep rates v are shown. In the limit of zero sweep rate, the ratio of rate to sweep rate becomes the derivative of the equilibrium isotherm, $d\theta/dE$ (dashed line). Higher sweep rates push the system further into irreversibility. In this sequence the sharpness of the phase transition peak is diminished and barely persists on the reverse sweep at the highest sweep rate shown.

4.4 Conclusions

The derivation of the activity based on the combinatorics of adding a particle to a lattice-gas system leads rather directly to a simple formula, which emphasizes the key role that the number of available sites plays. A rich variety of geometric constraints and types of sites are covered by this treatment, including systems not strictly on a lattice. An analytical expression for the number of available sites may be found in

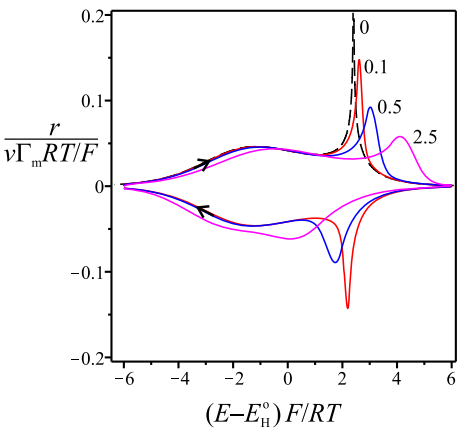

Figure 4.4: Voltammograms for adsorption of hard hexagons at different sweep rates. Rate normalized by sweep rate vs potential. From numerical solution of Eq. (4.24) with $k^\circ_{\rm ads}/\Gamma_{\rm m} = k^\circ_{\rm des}/\Gamma_{\rm m} = 1$, $\beta = 1/2$, sweeping from $F(E - E^\circ)/RT = -6$ to $+6$ and back to -6. Sweep rates vF/RT as shown. Dashed curve is the equilibrium analytical solution $(d\theta/dE) \cdot (RT/F)$ that applies in the limit of zero sweep rate.

cases where the problem is combinatorially simple, or when the activity as a function of coverage is known. The availability of an analytical expression for the coverage of available sites can make non-trivial and more realistic systems accessible to analytical treatment. Applications to hard-hexagon and mixed hard-hexagon/Langmuir systems have been used to demonstrate this, including an extension of hard-hexagon adsorption to the kinetic regime.

4.5 Acknowledgements

We thank the Natural Sciences and Engineering Research Council of Canada (NSERC) for financial support of this research. JRS thanks NSERC and the University of Victoria for a scholarship.

4.6 Supporting Information

4.6.1 Configurations example 1

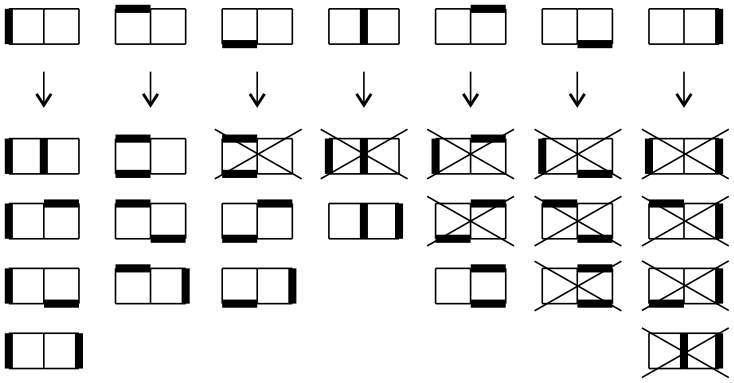

Figure 4.5: Configurations for dimers on a 2×3 square lattice. Top: configurations for $N = 1$, Bottom: configurations for $N = 2$.

As a simple example of the use of Eqs. (4.9) and (4.11), consider the case of

enumeration of dimers on a small 2×3 square lattice. The figure above has sites at the vertices. A dimer covers two lattice sites and is shown as a heavy line. For one dimer ($N = 1$), there are seven configurations, shown in the top row of the figure. This ensemble has 22 available locations/sites for the next dimer, each of which covers two adjacent lattice sites. Addition of a dimer to each of these locations is depicted in the bottom of the figure. This leads to 11 duplicates (crossed out in the figure) or redundancy by a factor of $2 = N + 1$, leading to $T_{av}/(N + 1) = 22/2 = 11$ configurations for two dimers on this surface (Eq. (4.9)). So $\langle N_{av} \rangle = 22/7$ and $\Omega_1/\Omega_2 = 7/11 = (N + 1)/\langle N_{av} \rangle = 2/(22/7)$, Eq. (4.11).

4.6.2 Configurations example 2

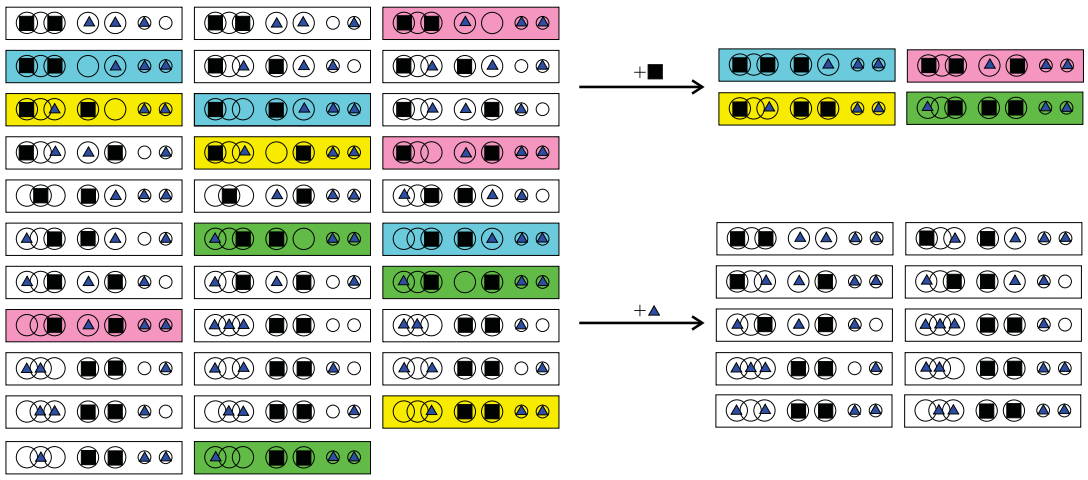

Figure 4.6: Configurations for a 7-site surface. Left: For 2 squares and 3 triangles. Top right: For 3 squares and 2 triangles. Bottom right: For 2 squares and 4 triangles.

Details of the configurations example introduced in the "Results and discussion" section. Refer to the figure above. A surface has seven sites (circles), 1 to 7 from left to right. There are two types of adsorbates (squares or triangles). The following rules apply.

1. There may be no more than one adsorbate per site.

2. For sites 1-3 (overlapping circles), a square may not be adjacent to a triangle or to another square.(Two triangles may be adjacent on these sites, though.)

3. For sites 4 and 5 (large non-overlapping circles), squares or triangles may adsorb without any restrictions about neighbors.

4. For sites 6 and 7 (small non-overlapping circles), only triangles may adsorb, again without restrictions.

All 32 configurations with two squares and three triangles obeying these rules are shown in the left of the figure. If we now consider addition of a square to this system, amongst the 32 configurations there are 12 available sites (one on each of the colored configurations) that are suitable. Addition of a square to the system gives 4 distinct configurations (top right), since addition to the 12 available sites results in triplicate configurations (identical colours give only one resulting configuration of that color). The duplicates arise because any of the 3 final squares could be the one just added. In other words, the 12 available sites is divided by the number of squares, 3, in the final states to give the number of resulting configurations. Similarly, for addition of a triangle to this system, there are 40 available sites amongst the 32 configurations that are suitable, leading to the $40/4 = 10$ configuations with 2 squares and 4 triangles shown in the bottom right.

4.6.3 Hard hexagon available sites

Starting from Joyce's expression for the activity [61] (Eqs. (20) and (47)), the coverage of available sites for the hard hexagon model may be calculated as:

$$\theta_{\rm av} = \begin{cases} 4\theta^7(1-\theta)\left(p^2\sqrt{Q_1}+Q_2-p\left(2Q_3+2Q_2\sqrt{Q_1}\right)^{1/2}\right)^{-1} & \theta<\theta_{\rm c} \\ \left(9\sqrt{5}-20\right)/5 = 0.02492\ldots & \theta=\theta_{\rm c} \\ -\frac{1}{2}\theta\left(2-3\theta\right)^{-1}\left(1-\theta\right)^{-3}\left(r+q^{1/2}(-p)^{3/2}\right) & \theta>\theta_{\rm c} \end{cases} \tag{4.25}$$

where

$$\theta_{\rm c} = \left(5-\sqrt{5}\right)/10 = 0.27639... \tag{4.26}$$

$$p = 1-5\theta+5\theta^2 \tag{4.27}$$

$$q = -1+9\theta-9\theta^2 \tag{4.28}$$

$$r = 1-12\theta+45\theta^2-66\theta^3+33\theta^4 \tag{4.29}$$

$$Q_1 = \left(1-\theta+\theta^2\right)p \tag{4.30}$$

$$Q_2 = (1-2\theta)\left(1-11\theta+44\theta^2-77\theta^3+66\theta^4-33\theta^5+11\theta^6\right) \tag{4.31}$$

$$Q_3 = 1-16\theta+106\theta^2-378\theta^3+803\theta^4 \tag{4.32}$$

$$-1080\theta^5+962\theta^6-576\theta^7+219\theta^8-50\theta^9+10\theta^{10} \tag{4.33}$$

Chapter 5

Conclusions and Future Work

The adsorption of formate onto Au was characterized as a reversible process in $HClO_4$ and H_2SO_4 solutions in Chapters 2 and 3. This style of adsorption was hypothesized decades ago [5], but was not characterized and was rejected by some [10, 11, 15]. By varying solution composition, the stoichiometry of the adsorption reaction was seen to follow Eqs. (2.1) and (2.12). This corroborates spectroscopic evidence [11,13–15] that formate is present on Au surfaces. The multiple types of adsorbed formate observed are thought to adsorb onto different types of surface sites.

Competition of formate for surface sites with perchlorate was observed unequivocally, in contrast with all previous studies in $HClO_4$ solutions where this was not studied. Three main coadsorption scenarios were observed. Formate adsorbs oxidatively according to Eq. (2.1) on the same sites as perchlorate displaying oxidative adsorption or no charge transfer, according to Eqs. (2.3) and (2.4), respectively. The third scenario was coadsorption of formate and perchlorate onto Au, with neither showing charge transfer (Eqs. (2.12) and (2.4), respectively). In order of mention, these three types of formate were named type A, B and C. It was found that their adsorption could be described adequately by the Sips isotherm. Oxidation rates for HCOOH were governed only by the coverage of these three types of formate, confirm-

ing the chemical rate limiting step proposed by Cuesta et al. [11, 15]. Two oxidation pathways were seen, a slower first order oxidation of type A formate, and a faster second order reaction of type B and C formate. The existence of these pathways is supported both by experimental data and fitting of this data to a simple model.

Analysis of oxidation rates in H_2SO_4 solutions reveals rates that are generally lower. This is justified by the strong adsorption of sulfate, which seems to obey Eqs. (3.6) and (3.5), adsorbing oxidatively in all cases seen. Sulfate adsorption almost completely prevents formate adsorption at low [HCOOH]:[H_2SO_4], as these equilibria have comparable potential dependence. Conversely at higher [HCOOH]:[H_2SO_4], type B formate is seen to adsorb almost as well as in $HClO_4$ solutions. This raises catalytic activity to levels seen in those solutions. Although HCOOH oxidation is still thought to have a chemical rate limiting step after formate adsorption, the mode of formate oxidation has not been fully characterized in H_2SO_4 solutions. A first-order dependence of rate on type B formate was observed, and a first-order dependence on type C formate was conjectured based on results in $HClO_4$ solutions [34].

Further study into the adsorption of formic acid as formate may be warranted on other surfaces. This work characterizes this reaction and subsequent formate oxidation fairly completely in $HClO_4$ and H_2SO_4 solutions on Au(poly) surfaces. These are however some of the worst catalytic systems for formic acid oxidation, so study of this adsorption reaction on other catalysts might be beneficial. Better catalysts such as Pt or Pt/Au alloys could make worthwhile future targets. Use of fast voltammetry to observe formate adsorption onto Pt has been demonstrated by Feliu at al. [31], albeit only in $HClO_4$ solutions and without accounting for supporting electrolyte effects. Accounting for these effects may very well change the assessment of the rate law, as was seen in this work on Au surfaces.

Some developments in the theory of coadsorbing species were made as well, in Chapter 4. Simple relationships describing the activity of lattice gases with geometric constraints on adsorption, for both finite systems and in the thermodynamic limit,

Eqs. (4.11) and (4.12) respectively, were derived. This is similar to work done for hard sphere systems [49]. A particle insertion method was used to reach these expressions free of Stirling's approximation. These expressions simplify treatments of coadsorption, and can be used to derive activities for systems mixing two separate adsorption isotherms. As an example, the derived expressions were used to simulate voltammograms for coadsorption of adsorbates obeying the hard hexagon and Langmuir adsorption isotherms. This is expected to be similar to coadsorption of sulfate and formate on certain single crystal faces of Au, as adsorbed sulfate exhibits an order-disorder phase transition like the hard hexagon isotherm. The applications of Eqs. (4.11) and (4.12) are more general than this single example. Any two adsorption isotherms for which analytical expressions for adsorbate activities are known can in theory be modelled at least approximately using the approach in Chapter 4. This is likely the most important application of the results, and a possible avenue for future research.

References

[1] Harrington, D. A.; Strobl, J. R. *Journal of Chemical Physics*, **2013**, *139*, 104104.

[2] Joyner, R. W.; Roberts, M. W. *Proceedings of the Royal Society of London, Series A: Mathematical, Physical and Engineering Sciences,* **1976,** *350,* 107.

[3] Columbia, M. R.; Thiel, P. A. *Journal of Electroanalytical Chemistry,* **1994**, *369,* 1.

[4] Kutschker, A.; Vielstich, W. *Electrochimica Acta*, **1963**, *8*, 985.

[5] Crepy, G.; Lamy, C.; Maximovitch, S. *Journal of Electroanalytical Chemistry,* **1974,** *54*, 161.

[6] Besenhard, J. O.; Parsons, R.; Reeves, R. M. *Journal of Electroanalytical Chemistry,* **1979,** *96,* 57.

[7] Burke, L. D.; Lee, B. H. *Journal of Electroanalytical Chemistry,* **1992***, 330,* 637.

[8] Chen, S.-L.; Wu, B.-L.; Cha, C.-S. *Journal of Electroanalyitcal Chemistry,* **1997,** *431*, 243.

[9] Avramov-Ivic, M.; Strbac, S.; Mitrovic, V. *Electrochimica Acta,* **2001,** *46,* 3175.

[10] Chen, S.-L.; Wu, B.-L.; Xiang, J. *Journal of Electroanalytical Chemistry,* **2001,** *517*, 95.

[11] Cuesta, A.; Cabello, G.; Hartl, F. W.; Escudero-Escribano, M.; Vaz-Dominguez,C.; Kibler, L. A.; Osawa, M.; Gutierrez, C. *Catalysis Today,* **2013,** *202*, 79.

[12] Hamelin, A. *Langmuir,* **1992,** *8,* 975.

[13] Zhang, Y.; Weaver, M. J. *Langmuir*, **1993***, 9,* 1397.

[14] Beltramo, G. L.; Shubina, T. A.; Koper, M. T. M. *ChemPhysChem,* **2005,** *6*, 2597.

[15] Cuesta, A.; Cabello, G.; Osawa, M.; Gutierrez, C. *ACS Catalysis*, **2012**, *2*, 728.

[16] Borkowska, Z.; Stimming, U. *Journal of Electroanalytical Chemistry,* **1991**, *312*, 237.

[17] Angerstein-Kozlowska, H.; Conway, B. E.; Hamelin, A.; Stoicoviciu, L. *Electrochimica Acta,* **1986,** *31,* 1051.

[18] Eberhardt, D.; Santos, E.; Schmickler, W. *Journal of Electroanalytical Chemistry,* **1996**, *419*, 23.

[19] Hamm, U. W.; Kramer, D.; Zhai, R. S.; Kolb, D. M. *Journal of Electroanal Chemistry*, **1996**, *414*, 85.

[20] Uchida, H.; Ikeda, N.; Watanabe, M. *Journal of Electroanalytical Chemistry,* **1997**, *424,* 5.

[21] Fawcett, W. R.; Kloss, A. A.; Calvente, J. J.; Marinkovic, N. *Electrochimica Acta*, **1998**, *44*, 881.

[22] Smalley, J. F.; Wu, Y.-C. *Journal of Physical Chemistry C,* **2011**, *115*, 2693.

[23] Sips, R. *Journal of Chemical Phys*ics, **1948**, *16*, 490.

[24] Baxter, S. C.; Chen, Y.; Shah, R. N.; Shimizu, K. D.; Umpleby, R. *Journal of Analytical Chemistry*, **2001**, *73*, 4584.

[25] Kumar, K. V.; Monteiro de Castro, M.; Martinez-Escandell, M.; Molina-Sabio, M.; Rodriguez-Reinoso, F. *Journal of Physical Chemistry C*, **2010**, *114*, 13759.

[26] Calefi, P. S.; Carnizello, A. P.; Ciuffi, K. J.; Gil, A.; Korili, S. A.; Marcal, L.; Nassar, E. J.; Trujillano, R.; Vicente, M. A. *Journal of Chemical & Engineering Data*, **2009**, *54*, 241.

[27] Auroux, A.; Carniti, P.; Gervasini, A. *Thermochimica Acta*, **2001**, *379*, 95.

[28] Otto, K.; Shelef, M. *Journal of Catalysis*, **1973**, *29*, 138.

[29] Bagotzky, V. S.; Khazova, O. A.; Sedova, S. S.; Vassiliev, Yu. B. *Electrochimica Acta*, **1971**, *16*, 913.

[30] Burshtein, R. Kh.; Michri, A. A.; Pshenichnikov, A. G. *Elektrokhimiya*, **1972**, *8,* 364.

[31] Grozovski, V.; Vidal-Iglesias, F. J.; Herrero, E.; Feliu, J. M. *ChemPhysChem*, **2011**, *12,* 1641.

[32] Ashton, M. R.; Jones, T. S.; Richardson, N. V. *Journal of Chemical Physics*, **1988,** *12,* 7564.

[33] Jones, T. S.; Richardson, N. V. *Surface Science Letters,* **1989**, *207,* L948.

[34] Harrington, D. A.; Strobl, J. R. In Preparation, as Chapter 2 herein..

[35] Magnussen, O. M.; Hagebock, J.; Hotlos, J.; Behm, R. J. *Faraday Discussions,* **1992***, 94,* 329.

[36] Gamboa, M.; Zelenay, P.; Wiekowski, A.; Shi, Z.; Lipkowski, J. *Journal of Electroanalytical Chemistry,* **1994***, 366*, 317.

[37] Edens, G. J.; Gao, X.; Weaver, M. J. *Journal of Electroanalytical Chemistry,* **1994**, *375,* 357.

[38] Uchida, H.; Ikeda, N.; Watanabe, M. *Journal of Electroanalytical Chemistry,* **1995**, *380, 25*5.

[39] de Moraes, I. R.; Nart, F. C. *Journal of Electroanalytical Chemistry,* **1999,** *461*, 110.

[40] Ataka, K.; Osawa, M. *Langmuir,* **1998,** *14*, 951.

[41] Kleinert, M.; Cuesta, A.; Kibler, L. A.; Kolb, D. M. *Surface Science*, **1999,** *430,* L521.

[42] Wirth, H. E. *Electrochimica Acta,* **1971***, 16*, 1345.

[43] Delahay, P. *Journal of Physical Chemistry*, **1966**, *70*, 2373.

[44] Delahay, P.; Holub, K. *Journal of Electroanalytical Chemistry*, **1967**, *16*, 131.

[45] Delahay, P.; Susbielles, G. G. *Journal of Electroanalytical Chemistry*, **1968**, *17*, 289.

[46] Lipkowski, J.; Mirwald, S.; Pettinger, B.; Shi, Z. *Journal of Electroanalytical Chemistry,* **1995**, *396*, 115.

[47] Saravanan, C.; Koper, M. T. M.; Markovic, M. N.; Head-Gordon, M.; Ross, P. N. *Physical Chemistry Chemical Physics,* **2002,** *4,* 2660.

[48] Hermse, C. G. M.; van Bavel, A. P.; Koper, M. T. M.; Lukien, J. J.; van Santen, R. A.; Jansen, A. P. J. *Surface Science,* **2004***, 572,* 247.

[49] Speedy, R. J., *Journal of the Chemical Society, Faraday Transactions 2,* **1977**, *73*, 714.

[50] Speedy, R. J., *Journal of the Chemical Society, Faraday Transactions 2,* **1981**, *77*, 329.

[51] Speedy, R. J., *Journal of Physical Chemistry,* **1988,** *92*, 2016.

[52] Corti, D. S.; Bowles, R. K., *Molecular Physics,* **1999**, *96*, 1623.

[53] Widom, B., *Journal of Chemical Physics,* **1963**, *39*, 2808.

[54] Van Leeuwen, J. M. J., *Journal of Chemical Physics,* **1964**, *41*, 2959.

[55] de Oliviera, M. J., *Physical Review E,* **1982**, *91*, 234.

[56] Henderson, J. R., *Molecular Physics,* **1998**, *95*, 187.

[57] Xing, J., *Journal of Chemical Physics,* **2001**, *115*, 8038.

[58] Soto-Campos, G.; Bowles, R.; Itkin, A.; Reiss, H., *Journal of Statistical Physics,* **1999**, *96*, 1111.

[59] Baxter, R. J., *Journal of Physics A: Mathematical and General,* **1980**, *13*, L61.

[60] Baxter, R. J., *Journal of Statistical Physics,* **1981**, *26*, 427.

[61] Joyce, G. S., *Journal of Physics A: Mathematical and General,* **1988**, *21*, L983.

[62] Joyce, G. S., *Philosophical Transactions of the Royal Society A,* **1988**, *325*, 643.

[63] Nagai, K., *Surface Science,* **1992**, *260*, 286.

[64] Blum, L.; Huckaby, D. A., *Journal of Electroanalytical Chemistry,* **1994**, *375,* 69.

[65] Legault, M.; Blum, L.; Huckaby, D. A., *Journal of Electroanalytical Chemistry,* **1996**, *409*, 79.

[66] Koper, M. T. M.; Lukien, J. J., *Journal of Electroanalytical Chemistry,* **2000**, *485*, 161.

[67] Koper, M. T. M.; Lukien, J. J., *Surface Science,* **2002**, *498*, 105.

[68] Labayen, M.; Furman, S. A.; Harrington, D. A., *Surface Science,* **2003,** *525,* 149.

[69] Nagai, K., *Surface Science Letters,* **1991***, 244*, L147.

[70] Hill, T. L., *An Introduction to Statistical Thermodynamics*, (Dover, NY, 1986) p. 249.

[71] Widom, B., *Journal of Chemical Phys*ics, **1967**, 46, 3324.

[72] Frenkel, D.; Louis, A. A., *Physical Review Letters,* **1992***, 68*, 3363.

[73] Gujrati, P. D., *Physical Review E,* **2001**, *63*, 021504.

[74] F.C. Andrews, *Equilibrium Statistical Mechanics*, 2nd ed., (Wiley-Interscience, NY, 1975) p 75.

[75] N.W. Ashcroft and N.D. Mermin, *Solid State Physics*, (Saunders College, Philadelphia, 1976) p. 41.

[76] J. Hölzl and F.K. Schulte, in G. Höhler, ed., *Springer Tracts in Modern Physics*, (Springer-Verlag, Berlin, 1979) v. 85, *Solid Surface Physics*, p.1.

[77] Lang, N. D.; Kohn, W., *Physical Review B,* **1970**, *1*, 4555.

[78] Han, K. K.; Cushman, J. H.; Diestler, D. J., *Journal of Chemical Physics,* **1990**, *93*, 5167.

[79] See supplementary material at http://dx.doi.org/10.1063/1.4820400 for a PDF file containing all configurations of the example surface, a second example of dimers on a square lattice, and the analytical expression for coverage of available sites for the hard-hexagon model. Also Sec. 4.6 in this work.

[80] Bitner, J. R.; Ehrlich, G.; Reingold, E. M., *Communications of the ACM.,* **1976**, *19*, 517.